

MINISTÉRIO DA EDUCAÇÃO
UNIVERSIDADE FEDERAL DO RIO GRANDE DO SUL
PROGRAMA DE PÓS-GRADUAÇÃO EM ENGENHARIA MECÂNICA

ANALYSIS OF THE POWER GENERATED BY THE BISTABLE FLOW AROUND
CIRCULAR CYLINDERS

por

Patrick Batista Habowski

Dissertação para obtenção do Título de
Mestre em Engenharia

Porto Alegre, Abril de 2020

ANALYSIS OF THE POWER GENERATED BY THE BISTABLE FLOW AROUND
CIRCULAR CYLINDERS

por

Patrick Batista Habowski
Engenheiro Mecânico

Dissertação submetida ao Corpo Docente do Programa de Pós-Graduação em Engenharia Mecânica, PROMEC, da Escola de Engenharia da Universidade Federal do Rio Grande do Sul, como parte dos requisitos necessários para a obtenção do Título de

Mestre em Engenharia

Área de Concentração: Fenômenos de Transporte

Orientador: Prof. Dr.–Ing. Sérgio Viçosa Möller

Co-Orientador: Prof. Dr. Alexandre Vagtinski de Paula

Aprovada por:

Prof. Dr. Gherhardt Ribatski EESC/USP

Prof. Dr. Luiz Augusto Magalhães Endres IPH/UFRGS

Prof. Dr. Guilherme Henrique Fiorot DEMEC/UFRGS

Prof. Dr. Fernando Marcelo Pereira
Coordenador do PROMEC

Porto Alegre, 30 de Abril de 2020

*“Each dream you
leave behind is a part of
your future that will no
longer exist.” (Steve Jobs)*

AGRADECIMENTOS

Agradeço primeiramente à minha família, que disponibilizou todos os recursos necessários para que eu concluísse essa etapa em minha vida. Aos meus amigos, por facilitarem os momentos de alto estresse e dificuldades passados na elaboração desse trabalho.

Agradeço aos sábios conselhos e a orientação do Prof. Sergio Möller, que guiou os passos desse trabalho, juntamente com a co-orientação do Prof. Alexandre de Paula. Agradeço, também, aos professores Gustavo da Cunha Dias (FURG) e Guilherme Henrique Fiorot (PROMEC). Aos colegas do Laboratório de Mecânica dos Fluidos da UFRGS, pelos anos de convivência, conhecimentos passados e auxílio nas diversas etapas de elaboração desse trabalho.

Agradeço à Universidade Federal do Rio Grande do Sul por dispor de excelentes e qualificados professores.

O presente trabalho foi realizado com apoio da Coordenação de Aperfeiçoamento de Pessoal de Nível Superior - Brasil (CAPES) - Código de Financiamento 001.

RESUMO

Este trabalho apresenta um estudo experimental acerca do fenômeno da biestabilidade em pares de tubos circulares dispostos lado-a-lado com um escoamento cruzado turbulento e a capacidade de gerar potência a partir desse fenômeno. Experimentos em um canal aerodinâmico e em um canal hidrodinâmico com mesma geometria foram realizados utilizando pares de cilindros com diâmetro de 25,1 mm e razão de espaçamento $p/d = 1,26$. No canal aerodinâmico foi empregada a técnica de anemometria de fio quente. A análise de Fourier e a transformada de ondaletas foram utilizadas através do software MATLAB para análise dos sinais gerados. Para os experimentos em canal hidráulico, a técnica de visualização com tinta colorida injetada no escoamento através de orifícios nos tubos foi utilizada. Vídeos gerados com uma câmera com resolução de 1080 x 720 pixels e 30 quadros por segundo foram analisados por meio do software Tracker. Os principais resultados mostraram a presença da biestabilidade para cilindros fixos dispostos lado a lado e para cilindros posicionados $2,5^\circ$ em relação ao escoamento, sendo que para esse último a presença da biestabilidade ocorreu apenas para os experimentos hidrodinâmicos. Na configuração onde os cilindros foram montados de modo que a rotação do sistema fosse possível, foram avaliadas as capacidades de gerar potência através de um sistema elétrico montado com um motor de passo funcionando como gerador. Os resultados mostraram a capacidade de geração de potência em pequenas escalas, conhecido como *colheita de energia*. Esses resultados foram comparados com um experimento de geração de potência através de uma turbina Savonius, mostrando que o sistema utilizando cilindros produz 43,5% menos energia. Por fim, um cilindro foi montado coaxialmente com o eixo do dispositivo, deixando o segundo cilindro livre para oscilar. Os resultados mostraram que o sistema oscila com baixa amplitude para qualquer velocidade de escoamento. Entretanto, ao se introduzir uma simples perturbação no escoamento, a amplitude aumenta, mantendo-se assim ao longo de todo o experimento, apresentando dois níveis de equilíbrio no sistema.

Palavras-chave: Anemometria de fio quente; Biestabilidade; Colheita de energia; Escoamento turbulento; Visualização de escoamento.

ABSTRACT

This work presents an experimental study about the phenomenon of bistability in pairs of circular tubes arranged side-by-side with a turbulent crossflow and the ability to generate power from this phenomenon. Experiments on an aerodynamic channel and a hydrodynamic channel with the same geometry were performed using pairs of cylinders with a diameter of 25.1 mm and spacing ratio $p/d = 1.26$. In the aerodynamic channel, the hot wire anemometry technique was used. Fourier analysis and wavelet transform were used using MATLAB software to analyze the generated signals. For the hydraulic channel experiments, the visualization technique with colored ink injected into the flow through holes in the tubes was used. Videos generated with a camera with a resolution of 1080 x 720 pixels and 30 frames per second were analyzed using the Tracker software. The main results showed the presence of bistability for fixed cylinders placed side-by-side and for cylinders positioned 2.5° to the flow, and for the latter, the presence of bistability occurred only for hydrodynamic experiments. In the configuration where the cylinders were mounted so that the rotation of the system was possible, the ability to generate power through an electrical system mounted with a stepper motor acting as a generator was evaluated. The results showed the capacity to generate power on small scales, known as energy harvesting. These results were compared with a power generation experiment using a Savonius turbine, showing that the system using cylinders produces 43.5% less energy. Finally, one cylinder was mounted coaxially with the axis of the device, setting up the second cylinder free to oscillate. The results showed that the system oscillates with low amplitude for any flow velocity. However, when is introduced a simple flow disturbance, the amplitude increases, maintaining itself throughout the whole experiment, presenting two levels of equilibrium in the system.

Keywords: Bistability; *Energy harvesting*; Flow visualization; Hot wire anemometry; Turbulent flow.

INDEX

| | | |
|----------|---|-----------|
| 1 | INTRODUCTION | 1 |
| 1.1 | Motivation..... | 1 |
| 1.2 | Main objectives..... | 2 |
| 1.3 | Organization of the work | 3 |
| 2 | FUNDAMENTALS..... | 5 |
| 2.1 | Turbulent flows..... | 5 |
| 2.1.1 | Characteristics of turbulence | 7 |
| 2.2 | Mathematical tools..... | 12 |
| 2.2.1 | Time domain analysis | 12 |
| 2.2.2 | Frequency domain analysis..... | 13 |
| 2.2.3 | Time and frequency domain analysis: Wavelet analysis | 15 |
| 2.3 | Literature Review | 17 |
| 3 | EXPERIMENTAL TECHNIQUES | 27 |
| 3.1 | Aerodynamic flow channel..... | 27 |
| 3.2 | Performed experiments in the aerodynamic flow channel | 28 |
| 3.2.1 | Fixed cylinders..... | 28 |
| 3.2.2 | Free to rotate cylinders | 30 |
| 3.2.3 | Free to oscillate cylinders | 35 |
| 3.2.4 | Savonius wind turbine | 37 |
| 3.2.5 | Electrical generation | 38 |
| 3.3 | Hydrodynamic flow channel..... | 40 |
| 3.3.1 | Experiments performed in the hydrodynamic flow channel..... | 42 |
| 3.4 | Experiments summary | 43 |
| 4 | RESULTS | 45 |
| 4.1 | Fixed cylinders – Aerodynamic channel results | 45 |
| 4.1.1 | Results for side-by-side cylinders (0° position) | 45 |
| 4.1.2 | Results from 2.5° to 35° positions | 50 |
| 4.1.3 | Results for 45° to 75° positions | 55 |

| | | |
|-------------------|---|------------|
| 4.1.4 | Results for tandem configuration (90° position) | 56 |
| 4.2 | Fixed cylinders – Hydrodynamic flow channel results | 57 |
| 4.2.1 | Results for side-by-side cylinders (0° position) | 57 |
| 4.2.2 | Results for 2.5° up to 90° | 59 |
| 4.3 | Results for free to rotate cylinders | 65 |
| 4.3.1 | Results for power generation for free to rotate cylinders | 76 |
| 4.4 | Results for the free to oscillate cylinders | 79 |
| 4.4.1 | Natural | 80 |
| 4.4.2 | One obstacle | 84 |
| 4.4.3 | Two obstacles | 89 |
| 4.4.4 | Perturbated | 94 |
| 4.5 | Results for the Savonius wind turbine | 100 |
| 4.5.1 | Results for power generation for the wind turbine | 107 |
| 5 | CONCLUSIONS | 111 |
| 5.1 | Suggestions for future works | 114 |
| | BIBLIOGRAPHY | 116 |
| APPENDIX A | Error Analysis of Tracker Software | 123 |
| APPENDIX B | Measurement Uncertainty | 124 |
| APPENDIX C | Details About the Angular Base | 125 |
| APPENDIX D | Details About the Angular Positioner | 126 |
| APPENDIX E | Studies Involving Balance of Classical Dynamic Systems | 127 |

LIST OF FIGURES

| | | |
|-------------|---|----|
| Figure 2.1 | Effects of Reynolds number in the vortex shedding for a smooth and circular cylinder [Blevins, 1990]. | 10 |
| Figure 2.2 | Relationship between Strouhal and Reynolds numbers [Blevins, 1990]. | 11 |
| Figure 2.3 | Bistability modes (a) and (b) (top view), velocity vs. time chart of this phenomenon (c) [De Paula, 2013]. | 17 |
| Figure 2.4 | Flow characteristic over two cylinders [Afgan et al., 2011]. | 18 |
| Figure 2.5 | Drag coefficient of each cylinder in the flow over two cylinders side by side. | 19 |
| Figure 2.6 | Interference regions and wake effects by Zdravkovich, 1987 [Zhou and Alam, 2016]. | 19 |
| Figure 2.7 | Flow mode changes for two cylinders placed side-by-side horizontally (a and b) and vertically (c and d) [Destefani, 2016]. | 22 |
| Figure 2.8 | Oscillation of the setup with two cylinders in the initial time of the acquisition [Varela, 2017]. | 23 |
| Figure 2.9 | Results of numerical simulation showing the non-simultaneous wake formation for a pair of cylinders at two different times [Neumeister et al., 2018]. | 26 |
| Figure 3.1 | Dimensions and details of the aerodynamic flow channel. | 27 |
| Figure 3.2 | Details about the fixation of the fixed cylinders (a) and the alignment of the probe (b, adapted from De Paula, 2008). | 29 |
| Figure 3.3 | Setup details (a), scheme to define the “shadow angle” (b), and experiment built with “shadow angle” (c). | 30 |
| Figure 3.4 | Details about the assembly of the free to rotate cylinders (a) and probes alignment (b, adapted from De Paula, 2008). | 32 |
| Figure 3.5 | Scheme with the aerodynamic flow channel and the high-speed camera. | 33 |
| Figure 3.6 | Details about the mirror view (schematic) analyzed in the Tracker software. | 33 |
| Figure 3.7 | Interface of Tracker software. | 34 |
| Figure 3.8 | Details about the assembly of the free to oscillate cylinders (a) and the alignment of the probe (b, adapted from De Paula, 2008). | 36 |
| Figure 3.9 | Details about the assembly of the wind turbine (a) and the alignment of the probe (b, adapted from De Paula, 2008). | 38 |
| Figure 3.10 | Stepper motor employed in the electrical experiments. | 39 |
| Figure 3.11 | Schematic of hydrodynamic flow channel for the visualization of the flow. | 41 |

| | | |
|-------------|---|----|
| Figure 3.12 | Details about the definitions to analyze the wake angles..... | 42 |
| Figure 3.13 | Fixation scheme in the hydrodynamic flow channel (a) and the details about the fixation for use angles $\pm 2.5^\circ$ than the predefined angles (b)..... | 44 |
| Figure 4.1 | Velocity signals from the hot wire anemometers for Probe 1 (a) and Probe 2 (b), side-by-side position..... | 46 |
| Figure 4.2 | Reconstruction of the signals using DWT for Probe 1 (a) and Probe 2 (b), | 47 |
| Figure 4.3 | CWT of the velocity signals for Probe 1 (a) and Probe 2 (b), | 48 |
| Figure 4.4 | Power spectrum from velocity signals for Probe 1 (a) and Probe 2 (b), 0° position. | 49 |
| Figure 4.5 | Reconstruction of the signals using DWT for Probe 1 (a) and Probe 2 (b), CWT for the velocity signals for Probe 1 (c) and Probe 2 (d), for the flow incidence angle of 2.5° . .. | 51 |
| Figure 4.6 | Results of velocity signals (a) and their reconstruction using DWT (b), flow incidence angle of 5° | 52 |
| Figure 4.7 | CWT for the velocity signals for Probe 1 (a) and Probe 2 (b), flow incidence angle of 5° | 53 |
| Figure 4.8 | Reconstructed signals of velocities using DWT for 15° (a), 25° (b), and 35° (c). | 54 |
| Figure 4.9 | Reconstructed signals of velocities using DWT for 45° (a), 60° (b), and 75° (c). | 55 |
| Figure 4.10 | Reconstructed signals of velocities using DWT for 90° and both probes. | 57 |
| Figure 4.11 | Photos from the visualization of the bistable flow phenomenon (side-by-side position)..... | 58 |
| Figure 4.12 | Results of flow visualization for side-by-side cylinders (a), 2.5° (b), 5° (c), 15° (d), 25° (e), 35° (f), 45° (g), 60° (h), 75° (i) and 90° (j)..... | 60 |
| Figure 4.13 | Wake behavior behind cylinders for flow incidence angle of 2.5° ; flow biased to the left side (a), flow with equal wakes (b), returning to the left-biased flow (c), formation of two equal wakes with an attempt to change the flow mode (d) and, finally, the flow mode change, with the flow deviated to the right side (e)..... | 62 |
| Figure 4.14 | Wake behavior behind cylinders for flow incidence angle of 5° (a), 15° (b), 25° (c), 35° (d), 45° (e), 60° (f), 75° (g) and 90° (h). Side and mirror views are shown for all the angles. | 63 |

| | | |
|-------------|--|----|
| Figure 4.15 | Statistical data for analyzed angles in the hydrodynamic channel. The positive signal means that the deflection angle is in the same direction as the rotation angle. | 64 |
| Figure 4.16 | Configuration with two different wakes: a narrow and a wide one (a, mirror view), and the side view of the cylinders (b) for the flow incidence angle equal to 15° | 64 |
| Figure 4.17 | Velocity signals for rotational cylinders for Probe 1 (a) and Probe 2 (b), free to rotate cylinders for $Re = 9.00 \times 10^3$ | 66 |
| Figure 4.18 | Angular positions for Reynolds number of 9.00×10^3 | 67 |
| Figure 4.19 | Photographs of the oscillation process of the free to rotate cylinders, $Re = 9.00 \times 10^3$; rest position (a), change in the rotational direction (b and c), and starting the rotational regime (d). | 68 |
| Figure 4.20 | Reconstructed signals of velocities using DWT for Probe 1 (a) and Probe 2 (b), free to rotate cylinders for $Re = 9.00 \times 10^3$ | 69 |
| Figure 4.21 | CWT for the velocity signals for Probe 1 (a) and Probe 2 (b), free to rotate cylinders for $Re = 9.00 \times 10^3$ | 69 |
| Figure 4.22 | Power spectrum from velocity signals (Figure 4.17) for Probe 1 (a) and Probe 2 (b), free to rotate cylinders for $Re = 9.00 \times 10^3$ | 70 |
| Figure 4.23 | Velocity signals for rotational cylinders for Probe 1 (a) and Probe 2 (b), free to rotate cylinders for $Re = 1.66 \times 10^4$ | 71 |
| Figure 4.24 | Angular positions for Reynolds number of 1.66×10^4 | 72 |
| Figure 4.25 | Photographs of the oscillation/rotational process of the free to rotate cylinders, $Re = 1.66 \times 10^4$; instant in which the configuration is changing the rotational direction, with details about the side and mirror view (a) and instant in which the configuration is already rotating (b). | 73 |
| Figure 4.26 | Reconstructed signals of velocities using DWT for Probe 1 (a) and Probe 2 (b), free to rotate cylinders for $Re = 1.66 \times 10^4$ | 74 |
| Figure 4.27 | Power spectrum from velocity signals (Figure 4.23) for Probe 1 (a) and Probe 2 (b), free to rotate cylinders for $Re = 1.66 \times 10^4$ | 75 |
| Figure 4.28 | CWT for the velocity signals for Probe 1 (a) and Probe 2 (b), free to rotate cylinders for $Re = 1.66 \times 10^4$ | 76 |
| Figure 4.29 | Power generation for reference flow velocity of 12.6 m/s and assist of the | 77 |
| Figure 4.30 | Power generation for reference flow velocity of 12.6 m/s with the extra cylinder. | 79 |

| | | |
|-------------|--|----|
| Figure 4.31 | Velocity signals reference velocity 5 m/s (a), 7.5 m/s (b) and 10 m/s (c), respectively; free to oscillate cylinders, natural setup..... | 80 |
| Figure 4.32 | Reconstruction of the signals using DWT for reference velocity 5 m/s (a), 7.5 m/s (b) and 10 m/s (c), respectively; free to oscillate cylinders, natural setup. | 81 |
| Figure 4.33 | CWT from the velocity signals for reference velocity 5 m/s (a), 7.5 m/s (b) and 10 m/s (c), respectively; free to oscillate cylinders, natural setup..... | 82 |
| Figure 4.34 | Angular behavior for the natural free to oscillate cylinders for 5 m/s (a), 7.5 m/s (b) and 10 m/s (c). | 83 |
| Figure 4.35 | Photographs from the high-speed camera for the natural oscillation cylinders, for the reference flow velocity of 10 m/s; the moment in which the acquisition is turned on (a) and the angular peak of this configuration (b)..... | 84 |
| Figure 4.36 | Velocity signals for reference velocity 5 m/s (a), 7.5 m/s (b), and 10 m/s (c), respectively; free to oscillate cylinders, one obstacle setup. | 85 |
| Figure 4.37 | Reconstruction of the signals using DWT for reference velocity 5 m/s (a), 7.5 m/s (b), and 10 m/s (c), respectively; free to oscillate cylinders, one obstacle setup..... | 86 |
| Figure 4.38 | CWT from the velocity signals for reference velocity 5 m/s (a), 7.5 m/s (b), and 10 m/s (c), respectively; free to oscillate cylinders, one obstacle setup..... | 87 |
| Figure 4.39 | Angular behavior for the free to oscillate cylinders with one obstacle for 5 m/s (a), 7.5 m/s (b) and 10 m/s (c). | 88 |
| Figure 4.40 | Photographs from the high-speed camera for the oscillation cylinders with one obstacle, for the reference flow velocity of 10 m/s; the moment in which the acquisition is turned on (a) and the angular peak of this configuration (b). | 89 |
| Figure 4.41 | Velocity signals for reference velocity 5m/s (a), 7.5 m/s (b), and 10 m/s (c), respectively; free to oscillate cylinders, two obstacle setup..... | 90 |
| Figure 4.42 | Reconstruction of the signals using DWT for reference velocity 5m/s (a), 7.5 m/s (b), and 10 m/s (c), respectively; free to oscillate cylinders, two obstacle setup. | 91 |
| Figure 4.43 | CWT from the velocity signals for reference velocity 5m/s (a), 7.5 m/s (b), and 10 m/s (c), respectively; free to oscillate cylinders, two obstacle setup..... | 92 |
| Figure 4.44 | Angular behavior for the free to oscillate cylinders with two obstacles for 5 m/s (a), 7.5 m/s (b), and 10 m/s (c). | 93 |

| | | |
|-------------|--|-----|
| Figure 4.45 | Photographs from the high-speed camera for the oscillation cylinders with 2 obstacles, for the reference flow velocity of 10 m/s; the moment in which the acquisition is turned on (a) and the angular peak of this configuration (b). | 94 |
| Figure 4.46 | Velocity signals for reference velocity 5m/s (a), 7.5 m/s (b), and 10 m/s (c), respectively; free to oscillate cylinders, perturbed setup. | 95 |
| Figure 4.47 | Reconstruction of the signals using DWT for reference velocity 5m/s (a), 7.5 m/s (b), and 10 m/s (c), respectively; free to oscillate cylinders, two obstacle setup. | 96 |
| Figure 4.48 | CWT from the velocity signals for reference velocity 5m/s (a), 7.5 m/s (b), and 10 m/s (c), respectively; free to oscillate cylinders, two obstacle setup. | 97 |
| Figure 4.49 | Angular behavior for the perturbed free to oscillate cylinders for 5 m/s (a), 7.5 m/s (b) and 10 m/s (c). | 98 |
| Figure 4.50 | Photographs from the high-speed camera for the perturbed oscillation cylinders; the moment in which the acquisition is turned on (a), perturbation being removed (b), angular peak (c), and details about the insertion of the perturbation in the flow (d-f). | 99 |
| Figure 4.51 | Velocity signals for the wind turbine for Probe 1 (a) and Probe 2 (b), for the reference flow velocity of 5.4 m/s. | 100 |
| Figure 4.52 | Reconstruction of the signals using DWT for Probe 1 (a) and Probe 2 (b), for the reference flow velocity of 5.4 m/s. | 101 |
| Figure 4.53 | CWT for the velocity signals for Probe 1 (a) and Probe 2 (b), for the reference flow velocity of 5.4 m/s. | 102 |
| Figure 4.54 | Photographs from the high-speed camera for the wind turbine; rest position (a), stable state ($\sim 90^\circ$) achieved by Savonius turbine (b), and rotational regime (c). | 102 |
| Figure 4.55 | Power spectrum from velocity signals of wind turbine for Probe 1 (a) and Probe 2 (b), for the reference flow velocity of 5.4 m/s. | 104 |
| Figure 4.56 | Velocity signals for the wind turbine for Probe 1 (a) and Probe 2 (b), for the reference flow velocity of 10 m/s. | 105 |
| Figure 4.57 | Reconstruction of the signals using DWT for Probe 1 (a) and Probe 2 (b), for the reference flow velocity of 10 m/s. | 105 |
| Figure 4.58 | Power spectrum from velocity signals of wind turbine for Probe 1 (a) and Probe 2 (b), reference flow velocity of 10 m/s. | 106 |
| Figure 4.59 | CWT for the velocity signals for Probe 1 (a) and Probe 2 (b), reference flow velocity of 10 m/s. | 107 |

| | | |
|-------------|---|-----|
| Figure 4.60 | Power generation obtained for reference flow velocity of 10 m/s..... | 108 |
| Figure 4.61 | Power generation for reference flow velocity of 12.6 m/s..... | 109 |
| Figure A.1 | Details of the error associated with the acquisition of cylinder position data... | 123 |
| Figure C.1 | Angular base used to position the cylinders..... | 125 |
| Figure D.1 | Angular positioner used to position the cylinders..... | 126 |
| Figure E.1 | Results for the generalized van der Pol oscillator and angular behavior for free to oscillate cylinders, reference flow velocity of 10 m/s..... | 127 |

LIST OF TABLES

| | | |
|------------|--|-----|
| Table 3.1 | Electrical specifications of the generator. | 39 |
| Table 3.2 | Summary of the experiments performed in this work. | 43 |
| Table 4.1 | Statistical data of velocity series for side-by-side cylinders for both probes. | 46 |
| Table 4.2 | Statistical data for velocity results for 2.5° to 35° and both probes. | 54 |
| Table 4.3 | Statistical data for velocity results for 45° to 75° and both probes. | 56 |
| Table 4.4 | Statistical data for velocity results for tandem position and both probes. | 56 |
| Table 4.5 | Statistical data for analyzed angles in the hydrodynamic channel. The positive signal means that the angle is in the same direction as the rotated angle. | 61 |
| Table 4.6 | Described oscillation process of the assembly for Reynolds number of 9.00×10^3 | 67 |
| Table 4.7 | Described oscillation process of the assembly for Reynolds number of 1.66×10^4 | 72 |
| Table 4.8 | Power generation results for free to rotate cylinders with the “throat device”, the reference flow velocity of 12.6 m/s. | 77 |
| Table 4.9 | Power generation results for free to rotate cylinders with the extra cylinder, the reference flow velocity of 12.6 m/s. | 78 |
| Table 4.10 | Power generation results for reference flow velocity of 10 m/s. | 108 |
| Table 4.11 | Power generation results for reference flow velocity of 12.6 m/s. | 109 |
| Table A.1 | Details of the error associated with the acquisition of cylinder position data. ... | 123 |
| Table B.1 | Main scale resolutions of used instruments. | 124 |

LIST OF ABBREVIATIONS

| | |
|----------|--|
| CFD | Computational Fluid Dynamics |
| CWT | Continuous Wavelet Transform |
| DNS | Direct Numerical Simulation |
| DWT | Discrete Wavelet Transform |
| HDD | Hard Drive Disk |
| LES | Large Eddy Simulation |
| LIFEELAB | <i>Innovation and digital manufacturing laboratory of the Engineering School</i> |
| PDF | Probability Density Function |
| PIV | Particle Image Velocimetry |
| PSD | Power Spectrum Density |
| PVC | PolyVinyl Chloride |
| RANS | Reynolds Averaged Navier–Stokes |

LIST OF SYMBOLS

| Latin Symbols | | Unit |
|----------------------|--|--------------------|
| $2D$ | Two-dimension | – |
| a | Wavelet parameter | – |
| b | Wavelet parameter | – |
| B_e | Bandwidth | Hz |
| $B(u')$ | Probability density function | - |
| D, d | Diameter | mm |
| E | Mean statistical error | % |
| f | Frequency | Hz |
| $f(x, t)$ | Instantaneous variable, scalar, or vector (coherent struct.) | - |
| f_c | Nyquist frequency | Hz |
| $f_c(x, t)$ | Coherent decomposition term | - |
| $f_r(x, t)$ | Non-coherent decomposition term | - |
| f_s | Acquisition frequency | Hz |
| F_s | Sampling frequency | Hz |
| f_{vs} | Vortex shedding frequency | Hz |
| g | Acceleration of gravity | m/s ² |
| I | Electrical current | mA |
| j | Dilatation coefficient | – |
| J | Reasonable number for DWT | – |
| K | Kurtosis | – |
| k | Translation coefficient | – |
| l | Size of block (for data series), dyadic value | – |
| n | Number of observations points | – |
| P | Electrical power | mW |
| p | pitch (distance between cylinder's center) | mm |
| P_{pres} | Pressure field | Pa |
| p/d | spacing ratio between cylinders | – |
| $P_{xx}(a, b)$ | Wavelet Spectrogram | (m/s) ² |

| | | |
|-------------------|--|-----|
| \Re | Real numbers | – |
| Re | Reynolds number | – |
| St | Strouhal Number | – |
| S_k | Skewness | – |
| t | Time | s |
| T | Period | s |
| U, u | Flow velocity | m/s |
| u' | Velocity fluctuations | m/s |
| \bar{u} | Mean velocity for a time series signal | m/s |
| u_{c_i} | Coherent velocity | m/s |
| U_e | Electrical tension | V |
| u_i | Velocity in x–direction | m/s |
| u_k | Velocity in z–direction | m/s |
| x | Position | mm |
| $x(f, t, B_e)$ | Generic function | mm |
| $x(t)$ | Generic function | – |
| $\tilde{X}(a, b)$ | Continuous Wavelet Transform (CWT) | – |
| $\tilde{X}(J, k)$ | Wavelet series | – |
| $\tilde{X}(j, k)$ | Discrete Wavelet Transform (DWT) | – |
| z | Height | m |

Greek Symbols

| | | |
|---------------------|---|--------------------|
| α | The angle of the pointer | rad |
| $\phi_{J,k}(t)$ | Scaling function associated with the wavelet function | - |
| Ω_{c_k} | Coherent vorticity | s ⁻¹ |
| Ω_i | Vorticity in x-direction | s ⁻¹ |
| ε_{ijk} | Permutation or Levi-Civita symbol, Levi-Civita tensor | - |
| σ^2 | Variance | [m/s] ² |
| σ^3 | Asymmetry factor (related to skewness) | [m/s] ³ |
| σ^4 | Flatness factor (related to kurtosis) | [m/s] ⁴ |
| $\psi_{a,b}(t)$ | Generic wavelet function | - |

| | | |
|-----------------|--|------------------------|
| $\psi_{j,k}(t)$ | Generic wavelet function | - |
| $\phi_{xx}(f)$ | Power Spectrum Density (PSD) | (m/s) ² /Hz |
| Δt | The time interval between two consecutive data | s |
| ν | Kinematic viscosity | m ² /s |
| ρ | Specific mass | kg/m ³ |

1 INTRODUCTION

1.1 Motivation

Circular cylinders are a common configuration that appears in many applications in industry and engineering, being a geometry used in pipelines, heat exchangers, transmission lines, and nuclear reactors, for example. In the literature is a subject very studied and discussed, mainly involving one or two cylinders and tube banks, due to the usage for heat exchangers. The arrangement of the tubes and the spacing ratios can vary depending on the specific application desired, as well as the flow or temperature distribution in heat exchangers. Around the tubes, the flow is complex and irregular, having no complete analytical modeling [Endres and Möller, 2001].

In flows over cylinders, vibrations can occur caused by dynamic loads from the flow and which are generally amplified with increasing fluid velocity. This vibration may cause catastrophic and permanent damages in the structures [Chen, 1985, 1987; Païdoussis, 1979, 1982], for example in the flow around heat exchangers in nuclear reactors. Therefore, the study of the bistability, a phenomenon which may aggravate these damages, is very important, even more by the fact that is a phenomenon not fully understood.

According to Priya and Inman, 2009, energy generation is a peculiar concern for remote places, such as deserts and isolated islands, once the energy distribution to these places is very expensive. To solve this problem, wireless systems are very interesting, since the costs of energy distribution no longer exist. However, supplying big demand of energy is still a challenge. Wireless systems are devices linked to the idea of energy harvesting.

The concept of energy harvesting is to use unused or wasted power to generate energy [Priya, 2007], using it immediately or storing it in batteries. Examples of unused power are human activity, motion, vibration, wind, solar power, electromagnetic and pressure gradients [Scarselli et al., 2016], which may be converted into electrical energy by simple electronic systems. Some examples of these electronic systems are photovoltaic sensors, piezoelectric sensors, smart roads, small generators, and others.

Energy harvesting has been investigated in the last decades since self-powered microsystems to bigger and more complex systems [Beeby et al., 2006; Anton and Sodano, 2007; Yang et al., 2014; Scarselli et al., 2016]. The concept of power harvesting works

towards developing self-powered devices that do not require replaceable power supplies, as the already mentioned wireless systems. Considering that, this work aims to generate small quantities of electrical power exploring the wind energy for two cylinders in specific arrangements.

To evaluate the ability to generate power, the bistability phenomenon was used as the main point for power generation. Since the ideal understanding of this phenomenon was not achieved yet, an exploration of wake behavior and bistability effect was presented for two cylinders placed side-by-side. The articles involving bistability review [Zhou and Alam, 2016; Sumner, 2010] present a lot of results of the past years' experiments, involving numerical and experimental processes to describe the bistability. Considering this scenario, this work also aims to contribute with results to improve the understanding of the bistability phenomenon of the flow on circular cylinders.

Bistable is the concept used to describe a phenomenon that presents distinct behaviors in a stable state for the same imposed conditions. The behavior of flows on specific configurations with two circular cylinders placed side-by-side are called bistable flow, once for these configurations, the flow presents two levels of average velocities under the same imposed conditions. For side-by-side cylinders, the bistable flow is reported for p/d ratio 1.1 – 2.5 [Alam et al., 2003; Alam and Sakamoto, 2005; Sumner, 2010], and do not depend on the Reynolds number or misalignments [De Paula and Möller, 2018]. A discussion about this phenomenon is presented in sec. 2.3.

1.2 Main objectives

The main objective of this work is to analyze the possibility to extract power from the bistability phenomenon through configurations using two cylinders placed side-by-side. Once the phenomenon is not completely understood, the specific objectives are:

- Analyzing the static behavior of the setup with two parallel circular cylinders, setting several angles to the flow until 90° ;
- Studying the oscillatory and rotatory phenomenon of a configuration with two cylinders placed side-by-side, generating video recordings and time series of velocity with the position of the setup along the time;

- Performing an experiment with a wind turbine, Savonius type, in order to compare the results with the rotatory setup;
- Perform an experiment with a setup using a central cylinder and another at the border, to explore only the oscillatory behavior;
- Measuring the electrical power generated through the setups using two cylinders to rotate, two cylinders to oscillate, and the wind turbine, comparing the power to generate electricity in small scales (energy harvesting).

1.3 Organization of the work

This work is organized into five chapters, as follows: chapter one is an introduction of the discussion that will be explored during the whole work. The motivation, justification, and main objectives are explained to summarize the work.

In the second chapter, a literature review is presented, from the basic concepts of turbulent flows to the recent works involving the bistability phenomenon. A mathematical approach is presented, pointing out the statistical definitions and equations used to analyze the experimental procedures which were performed in this work. Recent articles and works are presented as well, in order to explain how is the knowledge regarding the bistability phenomenon, and numerical and experimental analysis performed aiming to contribute to the understanding of the bistability phenomenon.

Chapter three presents the experimental procedures. Aerodynamic and hydrodynamic flow channels are described, as well the equipment used in each channel. The experiments are explained, detailing the positioning of the probes, the assembly of the cylinders, the camera setups, the defined angles to acquire the results, the configurations in the equipment, and the duration of the experiments. The methodology employed was detailed as well.

Chapter four is the core of the work, where the main results of the experiments are presented and discussed. The first experiment regards the static study of the wakes, with the cylinders set in several angles, where were presented the results for the aerodynamic and hydrodynamic flow channels. The second topic discussed is about the rotational cylinders, in which were made the video recordings with a high-speed camera to analyze the dynamic behavior of the cylinders and explore the ability to generate power. After this, was used an assembly with a central cylinder, where it was explored the oscillatory phenomenon. In the

last experiment, the Savonius turbine is studied, comparing the results obtained with previous experiments. All the experiments performed, were presented results regarding the velocity fluctuations, power spectrum, the angular positions of the wake, and video recordings.

The fifth and last chapter presents the conclusions about the results and observations made in chapter four. The methodology applied is discussed, the literature review is compared with the objectives and results obtained, and, to finish, suggestions for future works were proposed.

2 FUNDAMENTALS

In this section, a literature review about the main topics discussed along the work is presented. This review discusses some basic concepts in fluid dynamics up to recent works involving the fields explored in this work. A mathematical approach is also performed, involving the equations that rule the phenomenon analyzed and the statistical tools which supported the data collected.

2.1 Turbulent flows

The incompressible flow, laminar or turbulent, is strictly defined by the Navier–Stokes equations, despite the exact solution for these equations are only possible to laminar flows or low values of Reynolds number. Equation 2.1 is the mass conservation equation and the Equation 2.2 is the momentum equation.

$$\frac{\partial u_i}{\partial x_i} = 0 \quad (2.1)$$

$$\frac{\partial u_i}{\partial t} + u_j \frac{\partial u_i}{\partial x_j} = -\frac{1}{\rho} \frac{\partial P_{pres}}{\partial x_i} + \nu \frac{\partial^2 u_i}{\partial x_j \partial x_j} \quad (2.2)$$

In Equation 2.1 and Equation 2.2, u_i is the velocity field, P_{pres} is the pressure field and ρ is the specific mass of the fluid. The main difficulties to solve these equations are the nonlinearities of the governing equations and the complexity of the sought solution. The nonlinearity can be interpreted as a scale generation mechanism and energy transfer between different scales. This means that the solutions for the cases with high Reynolds numbers need to be performed through numerical methods, where exist some possibilities to solve them, like Direct Numerical Simulation (DNS), Large Eddy Simulation (LES), Reynolds Averaged Navier–Stokes (RANS), and others [Freire et al., 2002]. These equations are the mathematical basis of majority applications nowadays in engineering, being part of computational programs (Computational Fluid Dynamics, known as CFD) used to solve problems related to turbulent flows. However, experiments are still needed for the development and corroboration of the

numerical methods employed in numerical analysis. As the objective of this work is to present an experimental analysis, these numerical methods will not be discussed, once they will not be used throughout the work. A statistical review will be presented in topic 2.2.

In engineering and even in nature, the flow patterns are majority turbulent. The water currents below the surface of the oceans, clouds motion, interstellar gas clouds, boundary layer on aircraft wings, the mix of chemicals need turbulence and combustion process not even involve but may depend on the turbulence [Tennekes and Lumley, 1972]. When we talk about fluid dynamics, we can consider the laminar flow as an exception, occurring in small dimensions and high viscosities: the flow of lubrication oil in a bearing is an example.

The turbulent flows are unstable and own fluctuations depending on the space position and time. Among all characteristics that rule the turbulent flow, the scales involving this phenomenon must be pointed out: the bigger structures, related to the low frequencies, are controlled mainly by the geometry that generates them; the smaller structures, related to the high frequencies, are controlled mainly by the flow viscosity [Freire et al., 2002].

Starting from a laminar flow, this flow may become turbulent if exist inertial forces and/or potential energy gradient strong enough to overcome the viscous resistance of the flow which maintains it as laminar. Once overcome this resistance, a series of phenomena will make the laminar flow turbulent. This process of transition to turbulence is highly influenced by several factors, such as the perturbation level, surface roughness, pressure gradient, compressibility effects, heat transfer, and others [Möller and Silvestrini, 2004].

One of the most famous experiments involving instability and turbulence is dated to the 19th century: the investigation of flow inside pipes performed by Osborne Reynolds. In his investigation, Reynolds (1883) discovered the existence of two flow regimes: the laminar and the “turbulent” (defined as “winding” by the discoverer). He also defined a parameter to control this transition, based on the scales of velocity U , length d , and kinematic viscosity ν , defined by Equation 2.3.

$$Re = \frac{U d}{\nu} \quad (2.3)$$

For Equation 2.3, Reynolds observed that the turbulent flow is sustained just for values higher than 2300. Nowadays, is known that this value depends on the form that the

flow is perturbed [Freire et al., 2002]. Another discovery made by Reynolds was the existence of turbulent regions, posteriorly established as common close to the walls.

2.1.1 Characteristics of turbulence

Even nowadays, with long years of research and new discoveries, there is not a complete and succinct definition of turbulence. Tennekes and Lumley, 1972, proposed a list with seven characteristics of the turbulence, as follows:

- I. Irregularity: This characteristic makes the deterministic approach impossible, instead, only relies on statistical methods;
- II. Diffusivity: causes rapid mixing and increase rates of momentum, heat, and mass transfer. Considered by Tennekes and Lumley, 1972 as the most important of all the characteristics, once prevent the boundary layer separation on airfoils, increase heat transfers rates in all kinds of applications, increases momentum transfers between winds and oceans currents, and others;
- III. High Reynolds numbers;
- IV. Three-dimensional vorticity: turbulence is rotational and three-dimensional and is characterized by high levels of fluctuating vorticity. The random vorticity fluctuations could not maintain themselves if the velocity fluctuations were two-dimensional. For example, cyclones are not turbulent (2D rotation) and also the random waves on the surface of the oceans are not turbulent (irrotational);
- V. Dissipation: turbulence is a dissipative phenomenon that needs a continuous supply of energy to compensate the viscous losses. If energy is not supplied, the turbulence decays rapidly. This energy supply comes from the viscous shear stress, once the deformation work increases the internal energy of the fluid;
- VI. Continuum: the smallest scales occurring in a turbulent flow are larger than the molecular scale;
- VII. Turbulent flows are flows: the turbulence is not a characteristic of the fluid, but a characteristic of the fluid flow. Most of the dynamics of turbulence are the same in all fluids if the Reynolds number is large enough.

The vorticity is essential to identify turbulent flows and understanding your dynamic is important to comprehend the turbulence. The vorticity in the flow of a fluid is defined when the rotational of velocity exist and do not cancel itself in all the points of the flow. Mathematically, is defined by Equation 2.4, where ε_{ijk} is the Levi-Civita tensor.

$$\Omega_i = \varepsilon_{ijk} \frac{\partial u_k}{\partial x_j} \quad (2.4)$$

A new perspective involving the definition of turbulence was developed in the last decades, with the introduction of the idea of coherent structures. The main idea was a vortical movement, mainly on the smaller scales, in a chaotic state. The first revolution of this principle was the existence of the coherent structures quasi-deterministic, spread randomly in space and time, which are responsible for turbulent transport and noise generation (Brown and Roshko, 1974). Hussain, 1986, explained that diffusion and transport are more guided by induction than the gradients. This author also defines the coherent structure as a turbulent fluid mass, with vorticity correlated in phase, in the fluid region, and the scale of one coherent structure will be proportional to the smaller channel dimension.

According to Hussain, 1983, coherent structures are natural or induced and are related to the time of energy production. The initial conditions and the boundary conditions are related to the shear layer. For an instantaneous variable scalar or vector, a decomposition in a coherent ($f_c(x, t)$) and non-coherent ($f_r(x, t)$) function can be performed as given by the Equation 2.5:

$$f(x, t) = f_c(x, t) + f_r(x, t) \quad (2.5)$$

Part of the energy produced is due to the coherent structures, and the other part is produced by the non-coherent structures. The vortices in the turbulent flow are generated by shear or gravity, but they cannot maintain by themselves, as explained in topic V. The coherent vorticity is the property of the coherent structure, defined by Equation 2.6:

$$\Omega_{c_k} = \varepsilon_{ijk} \frac{\partial}{\partial x_j} u_{c_i} \quad (2.6)$$

Turbulent flows are characterized by very high Reynolds numbers, therefore is expected that any description of the turbulence will work properly as the Reynolds number tends to infinity. This criterion is called asymptotic invariance and allows criteria such as similarity via Reynolds number to be established. A discussion that arises when establishing this criterion is the quantification of high Reynolds numbers, because this problem does not depend on the value of the Reynolds number of the flow, but on the type of flow and the moment from which the flow characteristics will be independent of the Reynolds number, which means that the flow structure will no longer depend on the viscosity [Möller and Silvestrini, 2004].

In a simple turbulent flow, the characteristics of the flow at a given point over time are controlled only by the region immediately around it. The scales of time and length will vary along with the flow, as will the flow characteristics, so that once dimensioned by these scales, these dimensionless characteristics will remain unchanged. This fact is called local invariance or self-preservation [Möller and Silvestrini, 2004].

According to Blevins, 1990, a regular pattern of vortices is called “vortex street” and is localized behind the wake. They interact with the cylinder and they are the source of the effects called as vortex-induced vibrations. Vortex shedding for a smooth, circular cylinder in a steady subsonic flow is a function of the Reynolds number. Figure 2.1 and the list below shows the influence of the Reynolds number in the vortex shedding:

- a) $Re < 5$: fluid flow follows the cylinder contours, and is known as “creeping flow”;
- b) $5 \leq Re < 40$: the flow separates from the back of the cylinder forming a symmetric pair of vortices (Föppl) near wake, growing up as the Reynolds number grows up, reaching a distance up to three times than the diameter of the cylinders;
- c) $40 \leq Re < 150$: the wake becomes unstable, one of the vortices separates, while a laminar periodic wake of staggered vortices of opposite sign is formed;
- d) $150 \leq Re < 300$: the vortices breaking away from the cylinder become turbulent, although the boundary layer remains laminar;
- e) $300 \leq Re < 1.5 \times 10^5$: this range is called “subcritical” and the laminar boundary layer separates at about 80° behind of the front of the cylinder. The vortex shedding is strong and periodic. The boundary layer not separated is still laminar and the transition for the turbulence happens before vortex formation;

- f) $1.5 \times 10^5 \leq Re < 3.5 \times 10^6$: this range is called “transitional” and the cylinder boundary layer becomes turbulent, with the separation point moving to 140° behind the cylinder. Also, the cylinder drag coefficient drops to 0.3. The shedding layer tends to attach the body again, forming “separation–reattachment bubbles” for the angles $80\text{--}100^\circ$ and $120\text{--}140^\circ$, respectively;
- g) $Re \geq 3.5 \times 10^6$: this range is called “supercritical” and regular vortex shedding is reestablished with a turbulent cylinder boundary layer.

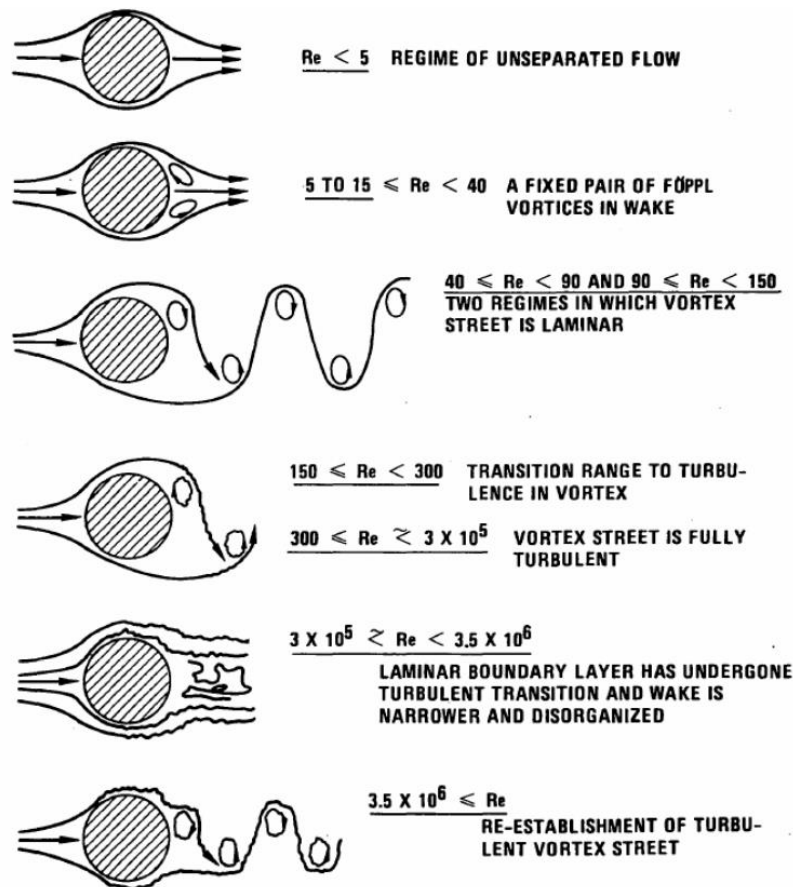


Figure 2.1 – Effects of Reynolds number in the vortex shedding for a smooth and circular cylinder [Blevins, 1990].

The dimensionless proportionality between the predominant frequency vortex shedding and the free velocity divided by the cylinder width is defined in Equation 2.7 and is known as the Strouhal number.

$$St = \frac{f_{vs} D}{U} \quad (2.7)$$

In Equation 2.7, f_{vs} is the vortex shedding frequency, U is the free stream flow velocity close to the cylinder and D is the cylinder diameter. Some authors consider the gap flow velocity, obtained by Bernoulli's principle, presented in Equation 2.8, to compute the Strouhal number, and others compute for the reference flow velocity. In this work, Strouhal numbers were computed considering these two velocities U , and were distinguished in the discussion of the results. This methodology allows the comparison with all the references presented in this work. A relationship for Strouhal and Reynolds numbers is shown in Figure 2.2. Until the beginning of the subcritical regime (about Reynolds number 300) the frequency occurs for low values of Strouhal numbers, less than 0.2. According to Blevins, 1990, for the entire subcritical regime, the Strouhal number remains at approximately 0.21. In the transitional regime, due to the breaking of stability in the vortex generation, the Strouhal number can grow to values in the range of 0.25 ~ 0.47, in the case of smooth cylinders, or grow slowly to values in the range of 0.3 for rough cylinders. In the supercritical regime, the Strouhal number is again independent of the roughness and tends to a value of 0.29.

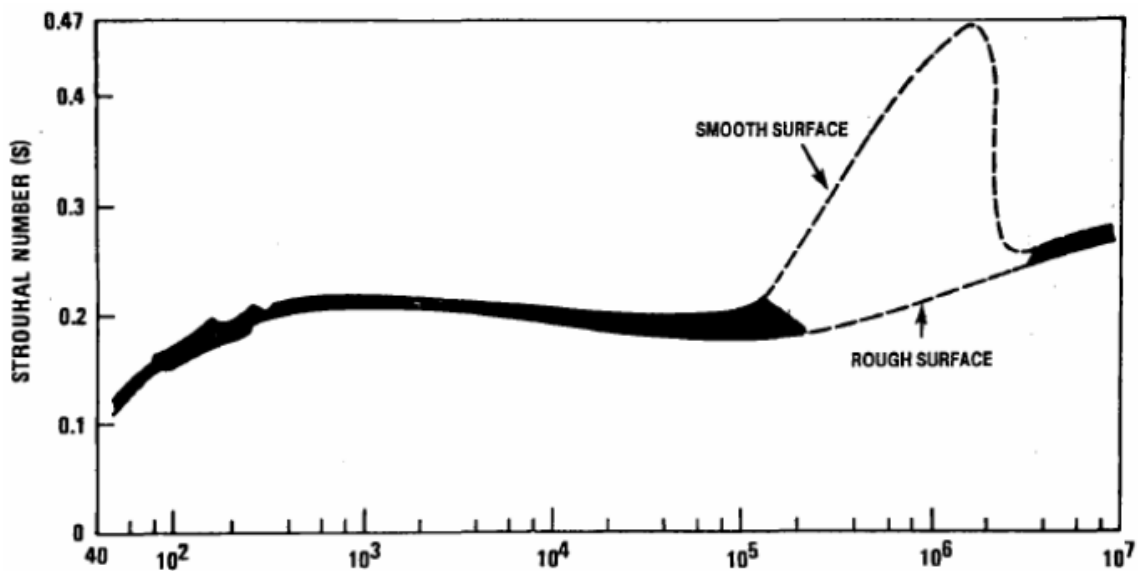


Figure 2.2 – Relationship between Strouhal and Reynolds numbers [Blevins, 1990].

$$\frac{U^2}{2} + gz + \frac{P_{pres}}{\rho} = constant \quad (2.8)$$

2.2 Mathematical tools

The Fourier analysis is the largest approach for studying random phenomena and processes and is broadly applied in turbulent flows. Random data, representing a particular phenomenon, are presented in the form of time series, obtained from the digitization of a continuous (analogic) signal, acquired with a frequency f_s , in the form of a sequence of numbers at constant Δt intervals. The analysis in time/frequency will be presented in the next topics.

2.2.1 Time-domain analysis

The analysis in the time-domain consists in calculating the four moments of Probability Density Function (PDF). These four moments are mean value (first moment), variance (second moment), asymmetry (third moment), and flatness (fourth moment).

The first moment consists in calculating the temporal mean value for the velocity fluctuations. To compute this quantity, the mean value of the velocity (\bar{u}) must be evaluated for all the instantaneous velocity values (u) in all the observation points (n), defined in Equation 2.9. The velocity fluctuations (u') are defined as the instantaneous velocity minus the mean value of velocity, given by Equation 2.10.

$$\bar{u} = \frac{\sum u}{n} \quad (2.9)$$

$$u' = u - \bar{u} \quad (2.10)$$

By means of definition, the first moment of u' is equal to zero [Tennekes and Lumley, 1972]. The squared mean of velocity fluctuations corresponds to the second moment and is computed as shown in Equation 2.11, where the $B(u')$ is the probability density function. The standard deviation is defined extracting the square root of the result of the Equation 2.11.

$$\sigma^2 = \overline{u'^2} = \int_{-\infty}^{\infty} u'^2 B(u') du' \quad (2.11)$$

The third moment is defined by Equation 2.12, and this value depends on the asymmetric part of the function. This value can be normalized by dividing the third moment by the σ^3 , generating the dimensionless parameter called skewness (Equation 2.13).

$$\overline{u'^3} = \int_{-\infty}^{\infty} u'^3 B(u') du' \quad (2.12)$$

$$S_k = \frac{\overline{u'^3}}{\sigma^3} \quad (2.13)$$

The fourth moment represents the flatness of the function and is defined in Equation 2.14. The dimensionless parameter kurtosis can be defined by dividing the fourth moment by σ^4 , as shown in Equation 2.15.

$$\overline{u'^4} = \int_{-\infty}^{\infty} u'^4 B(u') du' \quad (2.14)$$

$$K = \frac{\overline{u'^4}}{\sigma^4} \quad (2.15)$$

2.2.2 Frequency domain analysis

The Fourier analysis is used in the power spectrum analysis of turbulence, through the function called Power Spectrum Density (PSD). To evaluate a series of collected data, the power spectrum of Fourier is obtained, which represents the variation of mean squared value of a function $x(t)$ with frequency f , considering a T period and bandwidth B_e in a time t is given by Equation 2.16 [Bendat and Piersol, 1990].

$$\phi_{xx}(f) = \frac{1}{B_e T} \int_0^t x^2(f, t, B_e) dt \quad (2.16)$$

In the study of the turbulent flow, the function $x(t)$ is the velocity or pressure fluctuations. The vortex passage in several sizes (scales) are responsible for the fluctuations, and each scale is related to one frequency in the spectrum [Möller and Silvestrini, 2004]. Indrusiak, 2004, shows that the transform presented in Equation 2.16 is especially suitable for studies of stationary and ergodic signals, where frequency and amplitude do not vary with time and the result is independent of the sample. But it does not deal well with non-stationary processes at different scales, as they are evaluated over the entire time interval, i.e., this function has limited application in the study of transient flow regimes.

To ensure good quality in the power spectral density is necessary that the time t of the series be appropriate. Two parameters must be considered: the bandwidth (B_e) and the statistical mean error (E). The bandwidth is evaluated through Equation 2.17, where l is the size of the block in which will be divided the data series, being l a dyadic value. In Equation 2.17, which is used to define the bandwidth (B_e), the f_s is the acquisition frequency (see Equation 2.18) chosen for the study that represents the time interval between two consecutive data (Δt). This frequency must be suitable for the phenomenon studied.

$$B_e = \frac{f_s}{l} \quad (2.17)$$

$$f_s = \frac{1}{\Delta t} \quad (2.18)$$

Another consideration is the “cutoff” frequency f_c , which consists of low pass frequency filtering, to avoid doubling the frequencies without a spectrum and mistaken evaluation of the results. The theoretical “cutoff” frequency, called Nyquist frequency, is half the data capture frequency, but since the filter action is not the total cutoff, is a practical value 1/3 of the f_s ratio, shown in Equation 2.19. The mean statistical error (E) of the spectrum is given by Equation 2.20.

$$f_c = \frac{1}{3} f_s \quad (2.19)$$

$$E = (B_e t)^{-1/2} \quad (2.20)$$

2.2.3 Time and frequency domain analysis: Wavelet analysis

The wavelet analysis allows the study of a non-stationary signal in a time and frequencies domain and the detection of non-permanent flow structures. While the Fourier transform uses trigonometric functions as the basis, like the sinus function, the basis of wavelets transforms, according to Percival and Walden, 2000, are functions called wavelets $\psi(t)$, with finite energy and zero average. The main idea of the wavelet is the stretching and compressing of the window of the Fourier transform, allowing the definition of the scales of interest in time and frequency domains [Indrusiak et al., 2016]. The continuous wavelet transform (CWT) of a function $x(t)$ is given by Equation 2.21.

$$\tilde{X}(a, b) = \int_{-\infty}^{+\infty} x(t) \psi_{a,b}(t) dt \quad a, b \in \mathfrak{R} \quad (2.21)$$

In Equation 2.21, $\tilde{X}(a, b)$ is the generic function in the wavelet domain, a and b are the wavelet parameters, $x(t)$ is a generic function in the time domain and the $\psi_{a,b}(t)$ is a generic wavelet function. The wavelet spectrum is defined by the matrix of squared wavelets coefficients, given by Equation 2.22(2.22). In the wavelet spectrum, the energy is related to each time and scale or frequency. So, this characteristic allows the representation of the energy of this transient signal over time and frequency domains and is defined as spectrogram.

$$P_{xx}(a, b) = |\tilde{X}_{a,b}|^2 \quad (2.22)$$

In Equation 2.22, $P_{xx}(a, b)$ is the wavelet spectrogram given by means of energy units. The discrete wavelet transform (DWT) is a sub-sampling of continuous wavelets transform, but with dyadic scales, given by Equation 2.23. According to Indrusiak, 2004, the

DWT decomposes the energy of the time series in the respective scales and the sum shown in Equation 2.23 could be seen as a portion of energy due to the fluctuations in 2^{j-1} scale. Also, a time series and the discrete wavelet transform are both mathematical representations of an equal physical phenomenon.

$$\tilde{X}(j, k) = \sum_t x(t) \psi_{j,k}(t) \quad j, k \in \mathfrak{R} \quad (2.23)$$

In Equation 2.23, $\tilde{X}(j, k)$ is the wavelet series for the given j and k coefficients, j is the dilatation coefficient, k is the translation coefficient and the $\psi_{j,k}(t)$ is a generic wavelet function. According to Indrusiak and Möller, 2011, the length of the series restricts the number of coefficients, but the remaining ones are related to the lower frequencies, including the mean value of the signal, and cannot be disregarded. The DWT of a series with more than 2^j elements is calculated for $1 \leq j \leq J$, where J is a reasonable arbitrary choice and is defined in Equation 2.24.

$$\tilde{X}(J, k) = \sum_t x(t) \phi_{J,k}(t) \quad (2.24)$$

In Equation 2.24, $\phi_{J,k}(t)$ is the scaling function associated with the wavelet function. Therefore, any discrete time series with a sampling frequency (F_s) can be represented by Equation 2.25.

$$x(t) = \sum_k \tilde{X}(J, k) \phi_{J,k}(t) + \sum_{j \leq 1} \sum_k \tilde{X}(j, k) \phi_{j,k}(t) \quad (2.25)$$

In Equation 2.25, the first term is the approximation of the signal at the scale J , corresponding to the frequency interval $[0, F_s/2^{J+1}]$, and the second term is the details of the signal at the scales j , corresponding to the frequency intervals $[F_s/2^{j+1}, F_s/2^j]$. In the present work, was used Db20 wavelet and a level 8 ($J=8$) to reconstruct the signals from 0 Hz to 3.9063 Hz.

2.3 Literature Review

When a configuration with two parallel circular cylinders of equal diameter, placed side-by-side, is submitted to a transversal flow, a random phenomenon is presented in the wake, since the relation between the diameter D and the pitch p , where p is the distance between the centers of the cylinders, are around in the range $1.1 - 2.5$, according to Alam et al., 2003. This phenomenon is called bistability and presents a change in the flow mode, as shown in Figure 2.3 (a), (b), and (c).

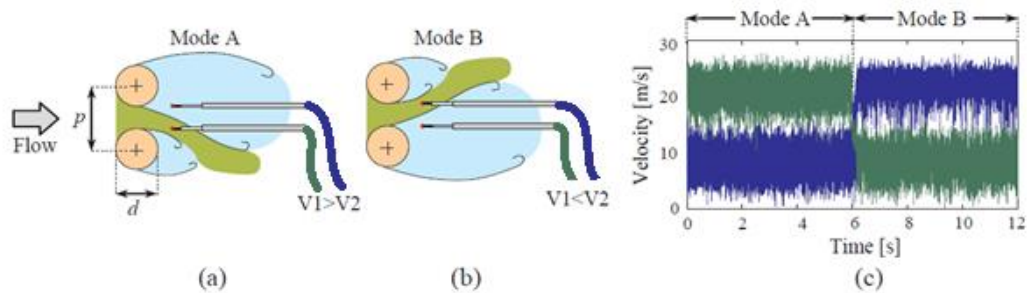


Figure 2.3 – Bistability modes (a) and (b) (top view), velocity vs. time chart of this phenomenon (c) [De Paula, 2013].

Figure 2.3 (a) and (b) shows the bistability phenomenon in the flow through the cylinders and Figure 2.3 (c) shows the result of this characteristic in a velocity vs. time chart. Besides that, according to De Paula et al., 2013, this phenomenon generates two dominant vortex-shedding frequencies, each one associated with a wake, where the wide wake is associated with the lower frequency, and the narrow wake is associated with the higher frequency.

The bistability is not restricted for two cylinders side-by-side; studies in others arrangements as tube banks, for example, showed effects of the bistability phenomenon [De Paula, 2008]. The case with two cylinders side-by-side is highly influenced by the p/d ratio. The literature, e.g., [Afgan et al., 2011; Alam et al., 2003; De Paula and Möller, 2013; Sumner, 2010], presents experimental and numerical studies, that show the changes in the wake configurations and drag and lift forces as the relation p/d is varied. These studies show that cylinders with $p/d > 1.8 - 2$ present characteristics of two independent single cylinders, as presented in Figure 2.4. For $1.1 < p/d < 1.8 - 2$, the main characteristic is the presence of

asymmetric wakes, one narrow and one wide, as shown in Figure 2.4, with a biased flow from the gap. This flow configuration changes with time as the narrow and wide wakes change their position. The flow is called bistable since each flow configuration assumes an apparent stable condition until the next change. For $p/d < 1.1$, the two cylinders setup behaves as a single bluff body. These characteristics are observed independent of the Reynolds Number, as described by Sumner, 2010.

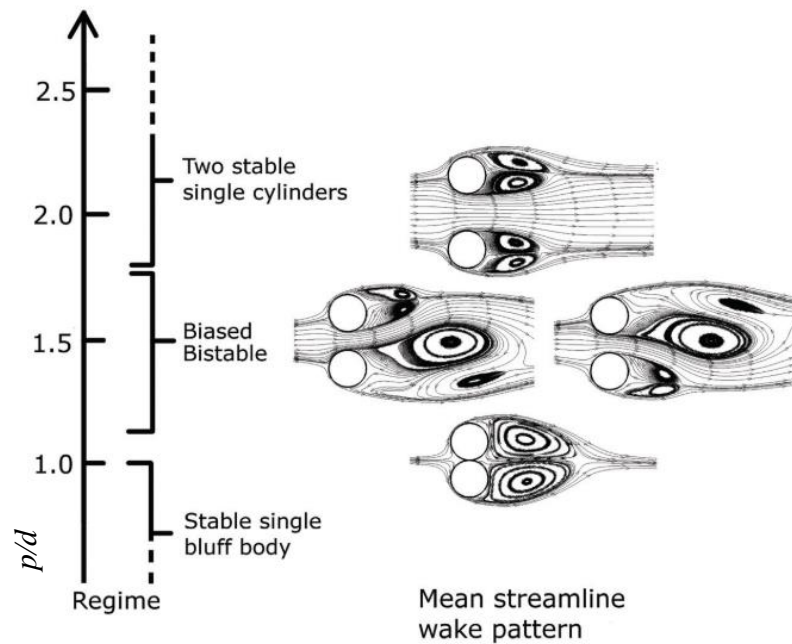


Figure 2.4 – Flow characteristic over two cylinders [Afgan et al., 2011].

The change in the wake configuration, presented in Figure 2.4, also affects the drag and lift forces, as presented in the work of Alam et al., 2003, for a Reynolds number of 5.5×10^4 . The drag behavior can be observed in Figure 2.5, where the wide wake (WW) presents a lower drag coefficient than the results of the narrow wake. For the cases with $p/d > 2.5$, only one value is observed for both cylinders.

Zdravkovich, 1987 describes the effects of interference produced by the proximity of the cylinders in the flow dynamics, classifying the flow according to the T/D and L/D ratio, where T and L are the transversal and longitudinal distance from the center of the cylinders, respectively. This classification presents four flow regions: proximity interference, proximity and wake interference, wake interference, and no interference (Figure 2.6).

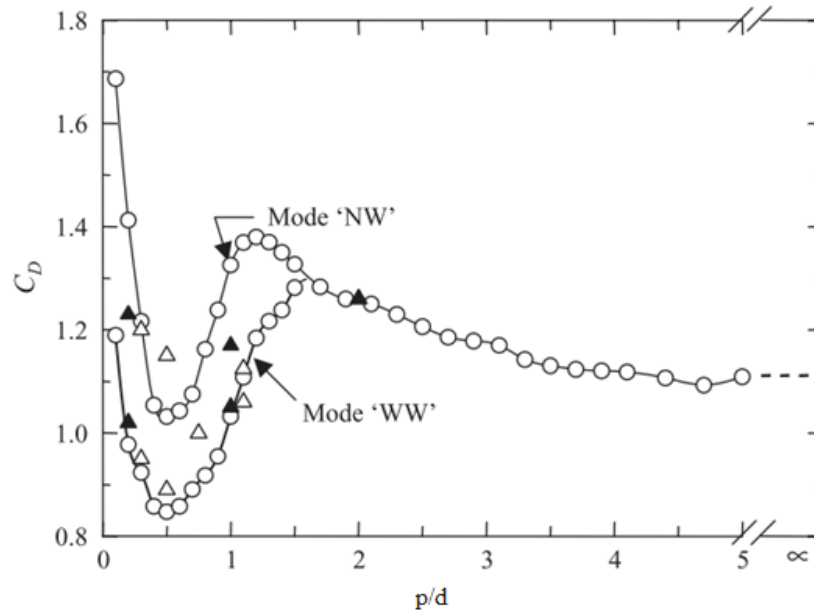


Figure 2.5 – Drag coefficient of each cylinder in the flow over two cylinders side by side. NW – Narrow Wake, WW – Wide Wake. [Alam et al., 2003].

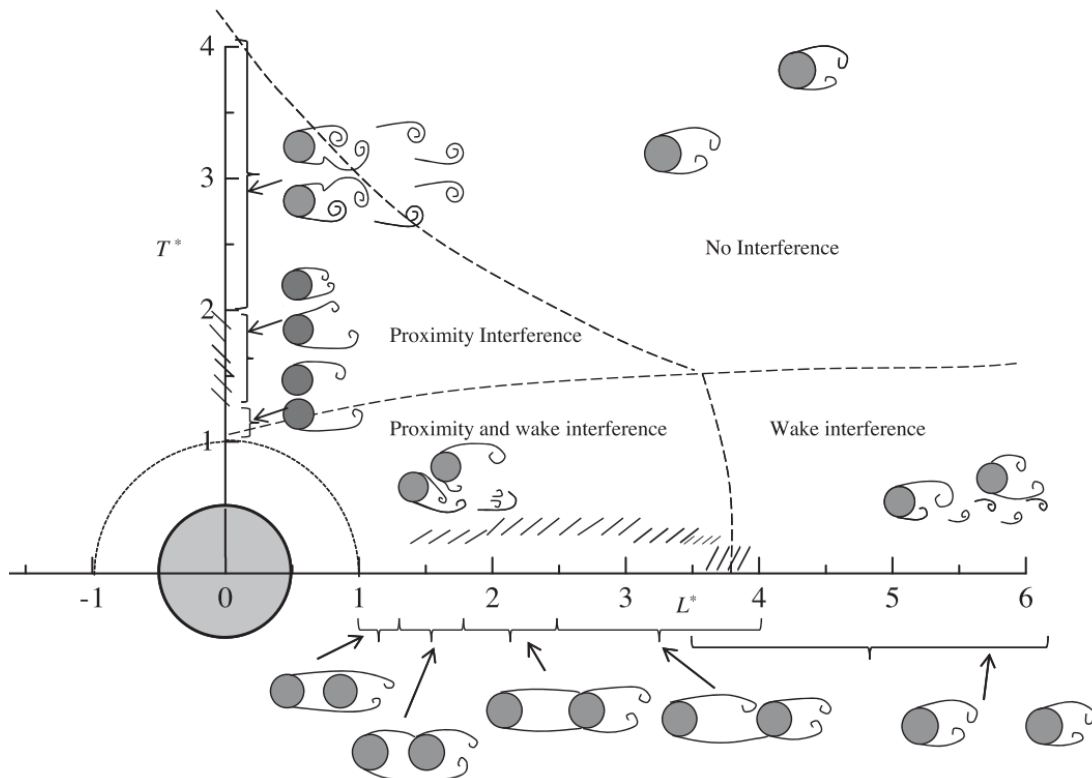


Figure 2.6 – Interference regions and wake effects by Zdravkovich, 1987 [Zhou and Alam, 2016].

Alam et al., 2003 described the main characteristics of a bistable flow englobing the drag and lift coefficients that also change with the bistability for several p/d -ratios, confirming that the asymmetric behavior occurs below $p/d = 2$. In a visualization experiment with hydrogen bubbles in water, a symmetric characteristic was observed, associated to a possible third mode, between the already known wide and narrow configuration, suggesting that this was an intermediate mode between the asymmetric wakes.

A study of the flow on staggered circular cylinders and a square cylinder (prism) is presented by Alam and Sakamoto, 2005. Results showed for the arrangement with about 5° with the flow that the gap flow is biased to one of the cylinders, and with 0° the gap flow is biased but switches intermittently to each cylinder. However, according to Zhou and Alam, 2016, the wake of two cylinders is highly complicated, and the bistable flow is highly sensitive to the angular position and the p/d ratio, occurring bistability phenomenon for 30° of angular position and p/d ratio equal 2.2. The authors also related the bistable flow phenomenon to four switching processes: shear layer reattachment and rollup switch, the bubble formation and burst switch, shear layer switch, and gap flow switch.

Results of flow visualization in a hydrodynamic flow channel performed by De Paula, 2008, for two circular cylinders, placed side-by-side and tube banks with 1.26 and 1.6 of p/d ratio showed the bistable phenomenon. The author performed the experiments for Reynolds number 7.5×10^3 and 1.5×10^4 , blockage ratio equal to 25.3%, and was perceived 2 – 4 flow mode changes in an observation time equal to 5 minutes.

Sumner, 2010 presents a thorough review of the flow around two circular “infinite” cylinders of equal diameter submitted to a steady crossflow, arranged in tandem, side-by-side, or staggered configurations focusing on the near-wake flow patterns, Reynolds number effects aerodynamic forces, and Strouhal number.

Afgan et al., 2011 present experimental and numerical studies that show the changes in the wake configurations and drag and lift forces as the relation p/d is varied.

De Paula and Möller, 2013 presented an experimental study with probability density functions and a double-well energy model to evaluate the wake changes on a flow over two side-by-side cylinders, showing the presence of two major states of energy, corresponding to the two flow modes, with pieces of evidence of a third flow mode. No evident correlation between the changes with time was found. Reconstructions performed with DWT were performed for axial and transversal velocity components together, and show the path or

temporal trajectory of the flow in the measurement plan where the flow has two stable states, but the authors found a path that the flow tries to switch from an initial stable mode to another one, but cannot achieve this second state, and then goes back to the first.

By means of hot wire anemometry technique and flow visualizations, De Paula et al., 2013, studied the presence of bistability around three cylinders in two triangular arrangements: one cylinder upstream and two downstream, and vice versa. The bistable flow was found in the configuration with one cylinder upstream and two downstream, but no bistable effect was detected in the second configuration, where the flow shows a single prominent shedding frequency.

Wong et al., 2014, investigated the dependence of the Reynolds number in a pattern of two rigid cylinders for several p/d ratios and angles between cylinders centers and flow. The range of subcritical Reynolds was explored and results pointed out to appreciable effects involving the Reynolds number, considering flow separation, boundary layer thickness, gap flow deflection, and vortex formation length.

Tandem positioning studies performed by means of time-resolved PIV, at subcritical Reynolds number and p/d ratio = 3.7, were performed by Elhimer et al., 2016. The authors found the bistable phenomenon for this specific configuration. Two flow regimes were investigated by the authors, where the first one presents a strong vortex shedding past the upstream and downstream cylinder, and the second one presents a weak alternating vortex shedding with reattachment past the upstream cylinder. Results highlight fundamental differences in the flow structures and dynamics around each cylinder. The shear layer vortices were tracked downstream the separation point, allowing the quantification of their shedding frequency. This is a very important issue regarding fluid instabilities in nuclear reactors and acoustic noise generated from the tandem cylinders of landing gear in aeronautics.

Destefani, 2016, presented a study in a hydrodynamic channel with two parallel circular cylinders and a diameter equal to 25.1 mm, in the side-by-side position with 1.26 p/d ratio, and the results showed the bistability phenomenon occurs in horizontal and vertical positions as well (Figure 2.7). Also, the author made experiments for about 25 minutes in both cases, and the bistable phenomenon occurred only one or two times in this period, i.e., the number of occurrences is much less than in the aerodynamic flow channel, in accordance with De Paula, 2008.

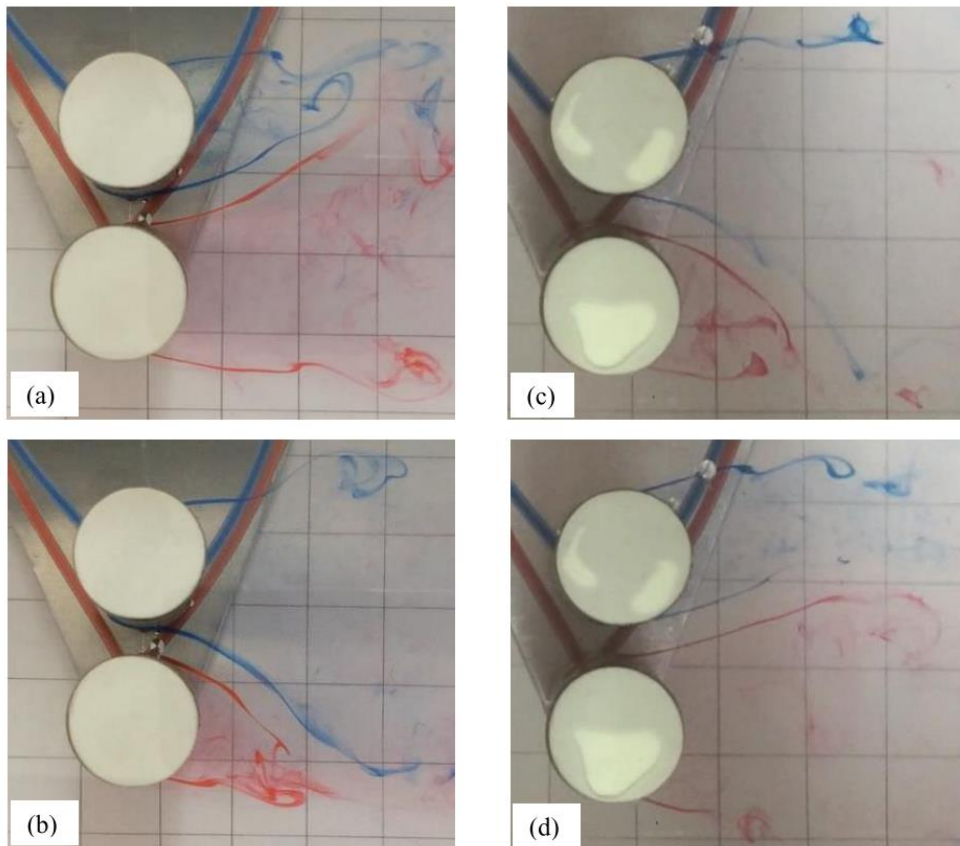


Figure 2.7 – Flow mode changes for two cylinders placed side-by-side horizontally (a and b) and vertically (c and d) [Destefani, 2016].

Varela et al., 2018 and Varela, 2017, presented a study of bistability for a configuration of two rigid cylinders, placed on a rotational structure, performing discrete wavelets transform to the data acquired, and showed some results for this configuration for several Reynolds numbers. For the results showed, there are more flow mode changings for the Reynolds number equal to 8.98×10^3 , which is the lowest presented by the author. With the highest Reynolds numbers explored, the phenomenon occurs as well, but less often. Authors measured by means of load cells the instantaneous drag forces of two cylinders side-by-side assembled on a pivoted table on an axis equidistant from the cylinder axes. When released from the load cells, the table was free to rotate. The two cylinders set oscillate around the rotation axis for both directions until it starts rotation (Figure 2.8).

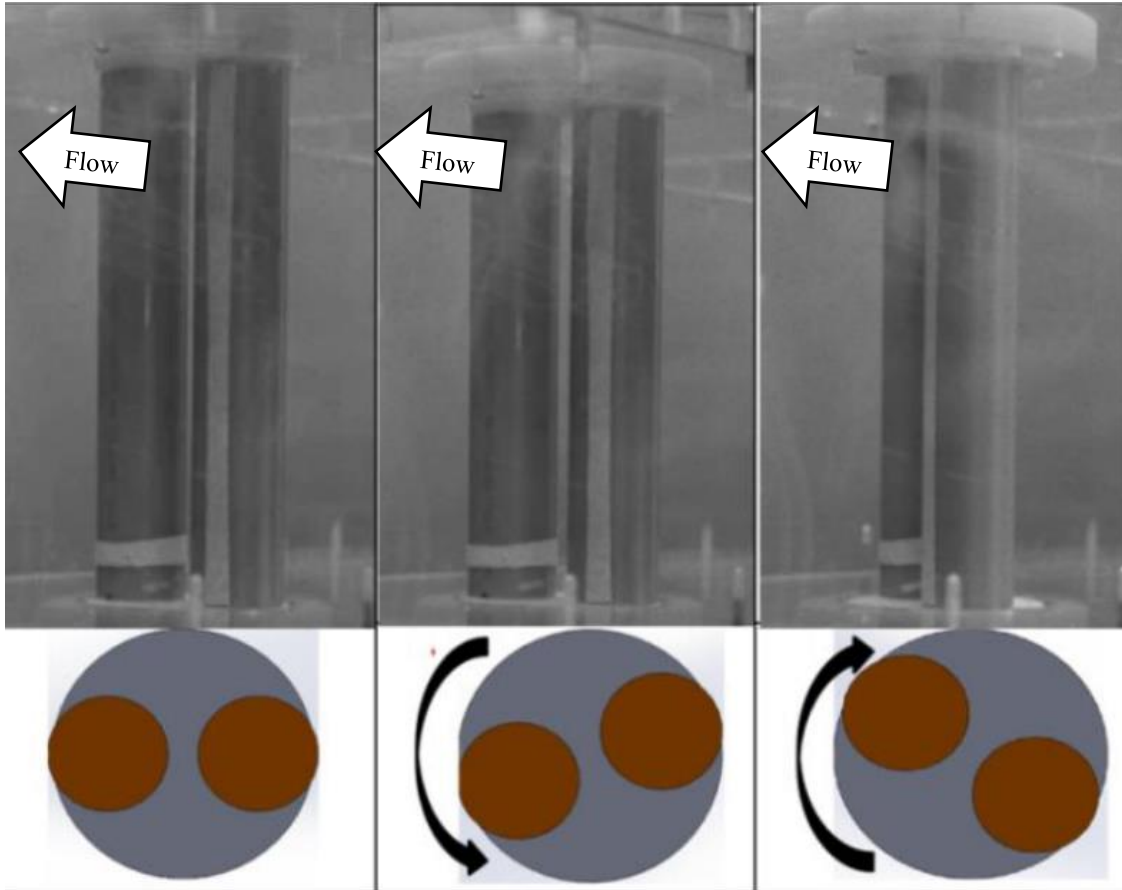


Figure 2.8 – Oscillation of the setup with two cylinders in the initial time of the acquisition [Varela, 2017].

Studies exploring the high subcritical and supercritical Reynolds number range ($Re > 2 \times 10^5$) are presented by Sun et al., 1992, Gu et al., 1993 and Gu and Sun, 1999 for side-by-side, staggered, and tandem positions. Results showed that the interference effect on fluctuating pressure is weaker at supercritical Reynolds than that at subcritical ones. Gu and Sun, 1999 classified the main flow patterns considering pressure measurements and flow visualization. The author identified three main flow patterns, emphasizing the discontinuity of large lift forces on cylinders on two different pressure patterns at critical angles.

The effects of positioning the cylinders in staggered configurations can be summarized by the studies of Sumner et al., 1997, Sumner et al., 1999 and Sumner et al., 2000. Considering the results, the cylinders present some patterns according to the combination of angle and p/d ratio imposed. For small incidence flow angles ($\alpha < 30^\circ$), three distinct flow modes were found by the author. Considering $\alpha < 20^\circ$ and $p/d = 1.125 - 4$, the results show

that the inner shear layer separated from the upstream cylinder reattaches on the downstream cylinder. However, for $\alpha = 20^\circ - 30^\circ$, this inner shear layer does not reattach on the downstream cylinder but rather goes through the gap between the cylinders. For larger p/d ratios > 4.0 and $\alpha < 30^\circ$, vortices generated by the upstream cylinder impinge upon the downstream cylinder. Considering configurations with $\alpha > 30^\circ$, one narrow and one wide wake form immediately behind the upstream and downstream cylinders, and three distinct behaviors were observed for the generated vortices.

Hu and Zhou, 2008a, 2008b presented studies regarding flow structures, Strouhal numbers, heat, momentum, and their evolutions in the wake of two staggered cylinders, using hot-wire anemometry and particle-image velocimetry techniques, for staggered configurations with p/d ratio 1.2 – 4.0. The authors identified four distinct flow structures: two single street modes and two thin street modes, based on flow topology, vortex-shedding frequencies, and their downstream evolutions. The single street modes are classified as modes S-I and S-II, where the mode S-I presents a single vortex street reasonably antisymmetric and mode S-II presents a single street asymmetric about the wake centerline. The two thin street modes are classified as mode T-I and mode T-II, where the mode T-I is characterized by two distinct streets of different vortex frequencies and mode T-II consists of two coupled streets of the same vortex strength and frequency. Each flow structure presented distinct heat and momentum transport characteristics from the others. In general, results pointed out that vortices transport heat more efficiently than momentum in a two-staggered cylinder wake.

Alam and Meyer, 2011 presented a study on two circular cylinders positioned at several flow incidence angles ($\alpha = 0 - 180^\circ$), in a wind tunnel with Reynolds number 5.52×10^4 . The authors evaluated the drag and lift coefficients and their fluctuations, and Strouhal numbers. Results showed that these coefficients are a strong function of α and the p/d ratio. The authors found 19 distinct flow patterns and emphasized the presence of quadristable and tristable flows. The quadristable flow is the result of simultaneous instabilities of the gap flow and separation bubble, occurring in side-by-side configurations at small p/d ratios. Three tristable flow patterns were found by the authors in different regimes, having different characteristics. The quadristable, tristable, and bistable flow created strong jumps in the coefficients and Strouhal numbers measured. Six different interacting mechanisms between the cylinders were observed by the authors, as follows: boundary layer and cylinder interaction, shear layer or wake and cylinder interaction, shear layer and shear

layer interaction, vortex and cylinder interaction, vortex and shear layer interaction, and vortex and vortex interaction. Each of them had different influences on the induced forces and Strouhal numbers.

Recent numerical works for staggered cylinders and low Reynolds numbers [Hsu et al., 2017 and Chauhan et al., 2019] presented similar flow patterns to those found by Sumner et al., 1997, 1999, 2000 and Hu and Zhou, 2008a, 2008b. Hsu et al., 2017 and Chauhan et al., 2019 found in their studies the shear layer reattachment for $\alpha = 0^\circ$, vortex pairing and enveloping for $\alpha = 45^\circ$, synchronized vortex shedding, vortex pairing and splitting for $\alpha = 90^\circ$.

Ye et al., 2019, explored the flow interference on the flow-induced vibrations of two staggered cylinders using fluid-structure interaction simulations, with low Reynolds numbers and high p/d ratios, ranging 5 – 7. With the increase of the inclined angle, the author divided the results into three regimes. In the first regime, at small inclined angles (close to tandem position) the vortices shedding from the upstream cylinder interacted directly with the downstream cylinder, increasing the pressure difference between the upper and lower surfaces of the downstream cylinder. In the second regime, at a medium inclined angle, the vortices shedding from the upstream cylinder do not interact with the downstream cylinder but instead with the vortices shedding from it. In the third regime at high inclined angles, the wakes from the upstream and downstream cylinders do not interact with each other at all and the two cylinders behave like an isolated cylinder.

Wu et al., 2020 presented a numerical study of the flow around two static staggered cylinders at high subcritical Reynolds number, varying the p/d ratio 1.5 to 4. Negative drag forces appeared close to tandem position, ascribed to a recirculation pair with opposite directions and a high-speed gap flow between the cylinders.

De Paula and Möller, 2018, presented a study showing that this phenomenon is chaotic for two circular cylinders placed side-by-side and for two rows of tube banks in triangular arrangement, i.e., it is independent of Reynolds number and cylinders misalignment lesser than 1° .

Neumeister et al., 2018, examined the bistable phenomenon in two cylinders placed side-by-side with p/d ratio equal 1.26 and Reynolds number 2.2×10^4 . The process of wake formation was described, where was found that the wake does not occur simultaneously along the z-direction of the cylinder (Figure 2.9), i.e., there is a delay in the switching process. This

characteristic is also presented in the cylinders wall pressure distribution, lift and drag coefficients.

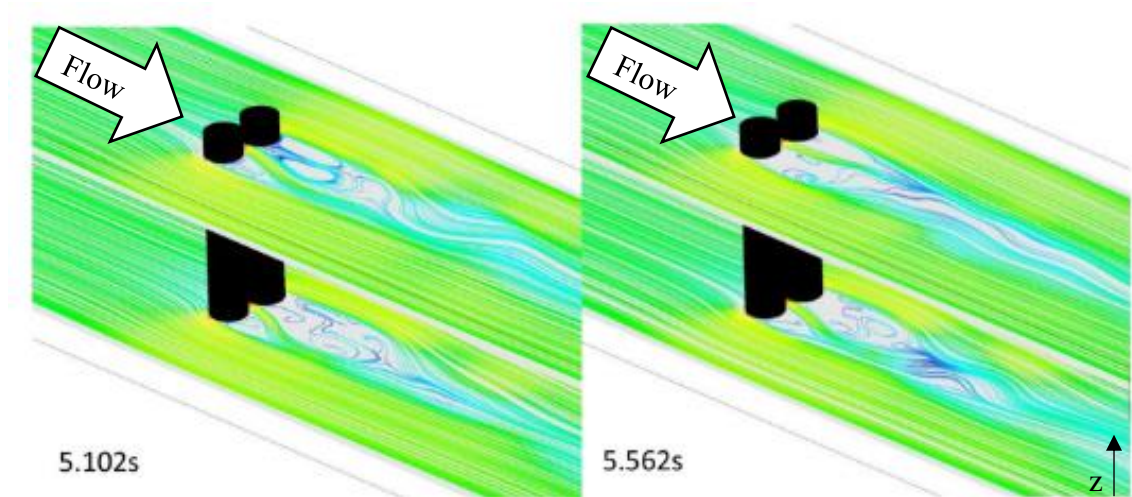


Figure 2.9 – Results of numerical simulation showing the non-simultaneous wake formation for a pair of cylinders at two different times [Neumeister et al., 2018].

Considering Zdravkovich's, 1987 classification, the study presented in this work belongs to two regions along with the experiment: the proximity interference, when it was in a side-by-side configuration, and in the proximity and wake interference, for the staggered one.

3 EXPERIMENTAL TECHNIQUES

3.1 Aerodynamic flow channel

The aerodynamic flow channel employed is a 2.29 m long acrylic glass channel, with a rectangular section of 0.193 m width and 0.146 m height, and is shown in Figure 3.1. The air flow is provided by a centrifugal blower of 0.75 kW and passes through a diffuser, two honeycombs, and two screens, to reduce the flow turbulence intensity to about 1% of the free stream velocity in the middle of the test section. The two circular cylinders are made of commercial PVC (PolyVinyl Chloride) with a diameter of 25.1 mm. The blockage ratio, computed considering the relation between the transversal area of the cylinders and the channel, varies between 10.9 to 26%, depending on the experiment performed. The reference velocity is obtained with a Pitot tube upstream of the test section. The velocity of the flow was measured with a DANTEC *StreamLine* constant hot wire anemometry system with two hot-wire probes type DANTEC 55P11, which is designed with a single wire perpendicular to the flow. The data acquisition was taken by a 16-bit A/D board, with a USB interface, with a sampling frequency of 1000 Hz and a low pass filter at 300 Hz.

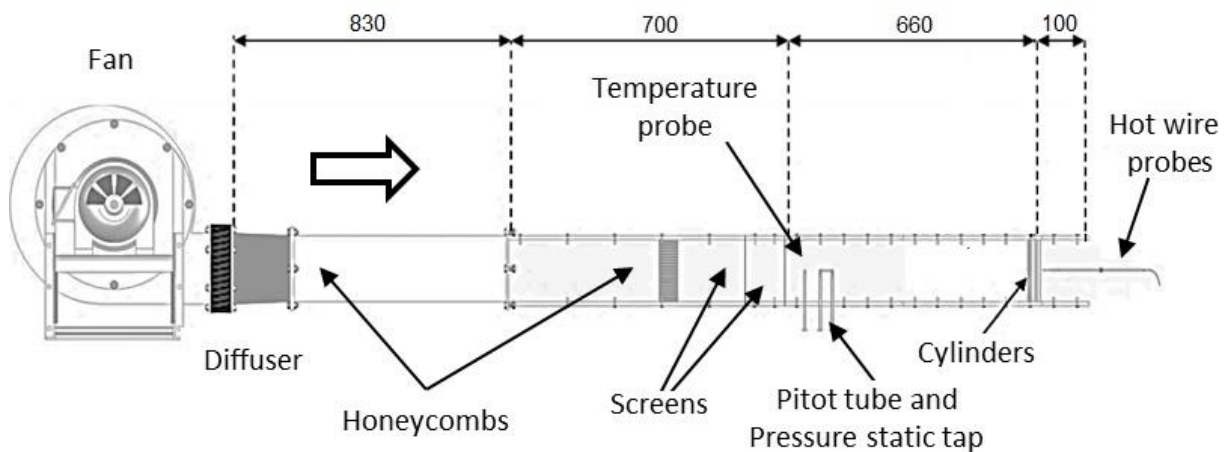


Figure 3.1 – Dimensions and details of the aerodynamic flow channel
[De Paula, 2008].

3.2 Performed experiments in the aerodynamic flow channel

Five experiments were performed in the aerodynamic flow channel in order to analyze the potential power generation through the bistable phenomenon, performed as follow:

- 1) An experiment with fixed cylinders at several angular positions to the flow (see sec. 3.2.1) was performed to study the wake for every analyzed angle;
- 2) The cylinders were assembled in a table free to rotate (see sec. 3.2.2), where the objective was to analyze the behavior of the assembly with the flow starting from the rest up to the target velocity;
- 3) A new concept of pattern, considering the influence of the wake in the oscillatory process (see sec. 3.2.3), was tested in order to complement the results for the experiment with fixed cylinders in tandem position (90°);
- 4) A Savonius wind turbine was also analyzed (see sec. 3.2.4) in order to compare the rotational velocities with the cylinders free to rotate;
- 5) Study of the ability to generate power from the bistability phenomenon (discussed inside sections 3.2.2, 3.2.4, and 3.2.3).

3.2.1 Fixed cylinders

In the first experiments, the cylinders were fixed as shown in Figure 3.2 (a). The angles to the flow were set by rotating a circular table, where the cylinders were fixed together with a protractor. A set of drilled holes on the upper wall assists the positioning the cylinders at chosen angles. The p/d ratio employed in this experiment was 1.26, in accordance with the standards employed in the shell-and-tube heat exchangers [TEMA Standards, 1988]. The time acquisition for the fixed cylinders was defined as 131.072 s. The Reynolds number of the experiment was 1.66×10^4 , based on the cylinder diameter and the reference velocity equal to 10 m/s.

For the measurements, it is important to determine the position of the anemometers, as shown in Figure 3.2 (b). The anemometers must be close to the cylinders and carefully aligned with them. Therefore, it was defined a scheme for positioning the anemometers, using a movable table that allows the movement in x and y axes, with a scale with a resolution of 0.1 mm. In this scheme, the distance DI (Figure 3.3a) was changed every time the incidence

angle was modified. To determine this distance for every incidence angle, it was considered an initial distance equal to 15.8mm (Figure 3.2b) plus a displacement caused by the rotation of the configuration for each angle. This distance change was necessary to avoid the probes touching the cylinders and breaking, once the cylinders are closer as the angle is increased. The distance $D2$ employed in Figure 3.3 (a) was 6.2 mm, where the probes were aligned with the inner tangents of the cylinders for the side-by-side configuration (Figure 3.2b).

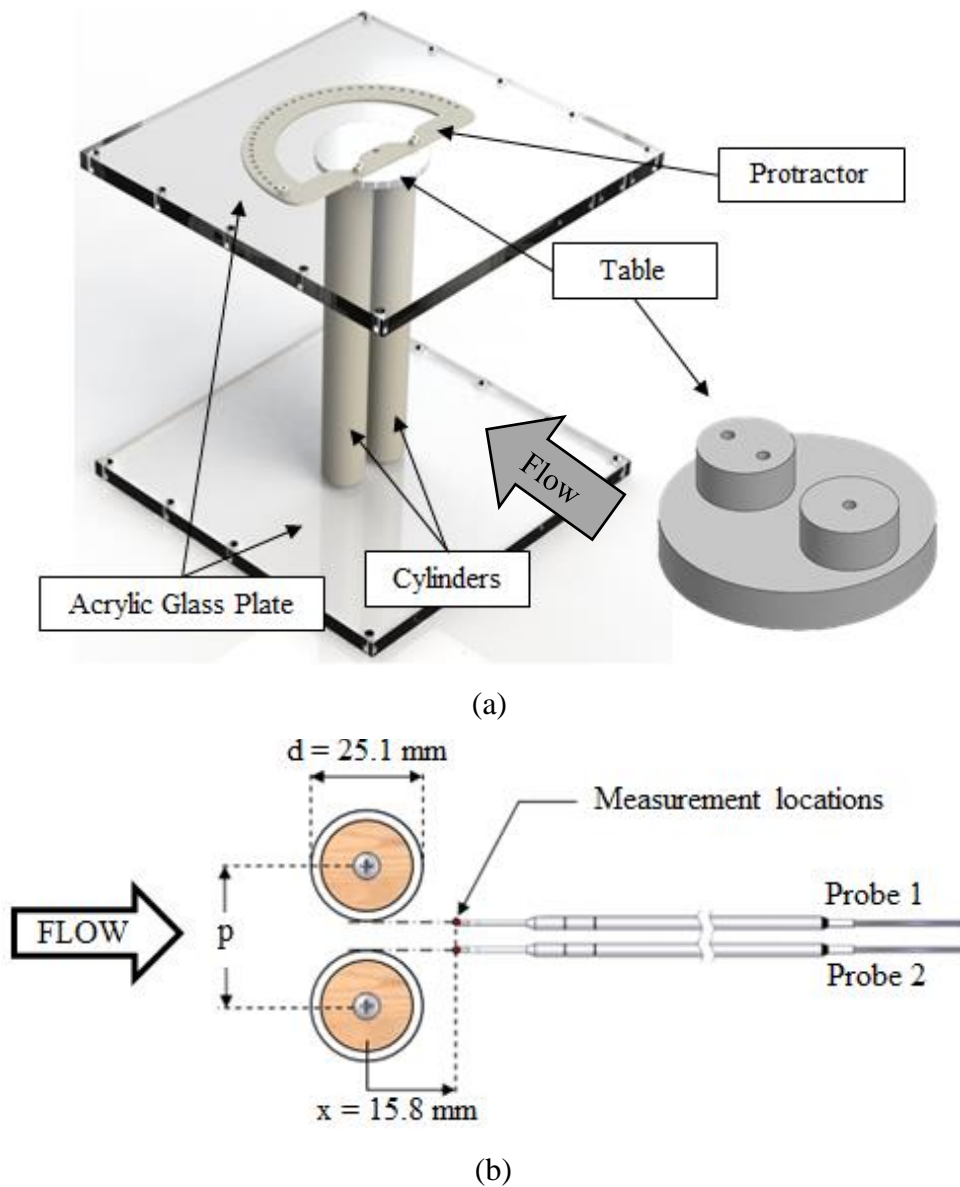


Figure 3.2 – Details about the fixation of the fixed cylinders (a) and the alignment of the probe (b, adapted from De Paula, 2008).

To determine the angles to perform this analysis was considered the “shadow angle”, i.e., the angle between the line that crosses the two tangent walls of each cylinder with the center of the pitch p and the flow, as shown in Figure 3.3 (b). The “shadow angle” represents the angle in which the distance between the two nearest walls of the cylinders is equal to zero considering the central line of the aerodynamic flow channel in a 2D view (Figure 3.3 c). For two cylinders of 25.1 mm of diameter and p/d ratio equal to 1.26, the “shadow angle” is equal to 36.75° . Thus, more angles were explored until the “shadow angle”, and after it were explored some angles to achieve the tandem position. The analyzed angles were 0° (side-by-side configuration), 2.5° , 5° , 15° , 25° , 35° , 45° , 60° , 75° and 90° (tandem position).

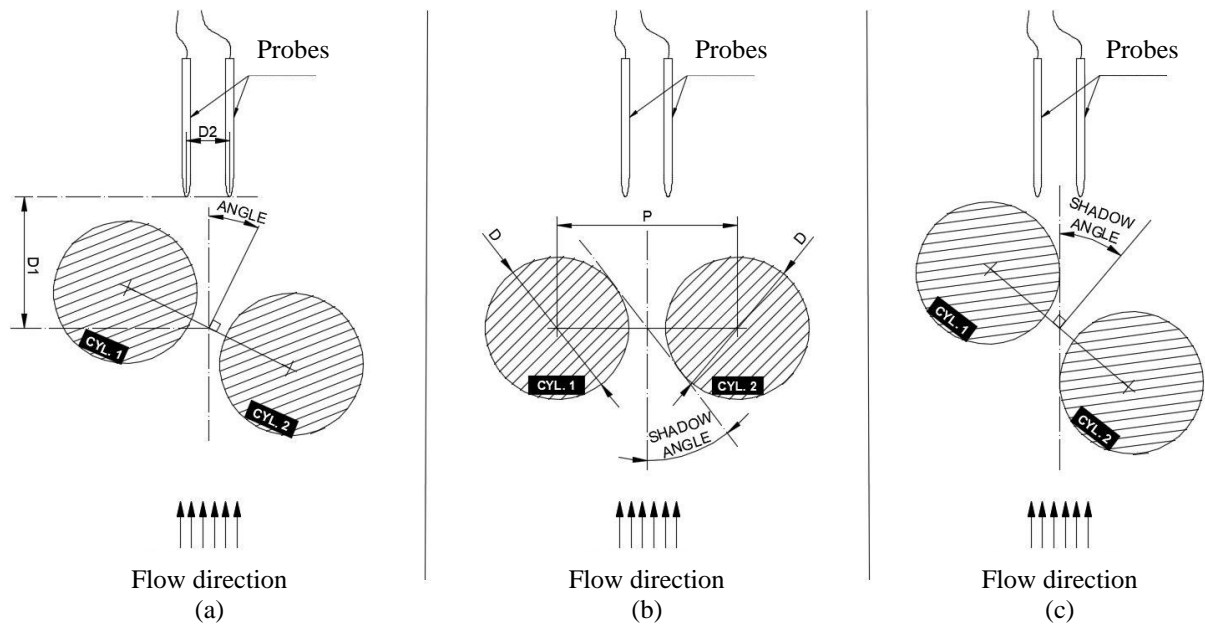


Figure 3.3 – Setup details (a), scheme to define the “shadow angle” (b), and experiment built with “shadow angle” (c).

3.2.2 Free to rotate cylinders

In the free to rotate cylinders experiment, the cylinders were assembled as shown in Figure 3.4 (a). The rotating table is coupled in the acrylic glass using low wear bearings. Therefore, the damping in the system was not accounted in the present study. The p/d used was 1.26, the same for the fixed cylinders. In the initial position, the blockage ratio of the cylinders is 26% and during the rotation, the blockage ratio varies between 13% (tandem

position) to 26% (side-by-side position), due to the instantaneous position of the cylinders. The time acquisition for the free to rotate cylinders was defined as 32.768 s, since the phenomenon of interest occurred before about 15 s.

The chosen position for the anemometers (Figure 3.4b) allows the measurements with the fixed and rotating cylinders, but for the experiment using fixed cylinders, in order to get better results, the probes were approached to the cylinders for the measurements, as explained in the section 3.2.2. For the free to rotate cylinders, the anemometers were distanced, remaining at a fixed distance from the cylinder's walls. The Reynolds numbers for the experiments were 9.00×10^3 , with a reference velocity equal to 5.4 m/s and 1.66×10^4 , with a reference velocity equal to 10 m/s, based on the cylinder diameter and the free flow velocity. The purpose of using two different reference velocities in this experiment is to explore the possibility of generating power in these two cases.

The behavior of the rotating cylinders was studied using a high-speed camera model Phantom V411 – Ametek, equipped with a 50 mm lens model AF-S VR Micro-Nikkor, with a resolution of 640 x 480 pixels and 1000 frames per second, which corresponds to the 1 kHz frequency in the data acquisition of the hot wire signal. The camera is controlled by a computer connected to the camera with an Ethernet cable. It was positioned using a tripod. The synchronization between the velocity signal and the camera was performed by the CTA controller, which controls the anemometer system and owns an auxiliary output signal used to trigger the recording. A mirror was mounted at the top of the flow channel, positioned 45° with the camera, in order to track the angle between the cylinders and the main flow. To do this, a pointer was mounted on the axis of the setup. A white background was placed behind the pointer in order to enhance the contrast for the Tracker software. A scheme with the detailed positioning about the channel and the high-speed camera is presented in Figure 3.5.

The Tracker software considers the angles as shown in Figure 3.6, where the schematic shows the pointer and the white background. It means that when the pointer is moving counter-clockwise, the angular values increase, and when the assembly is moving clockwise, the angular values decrease.

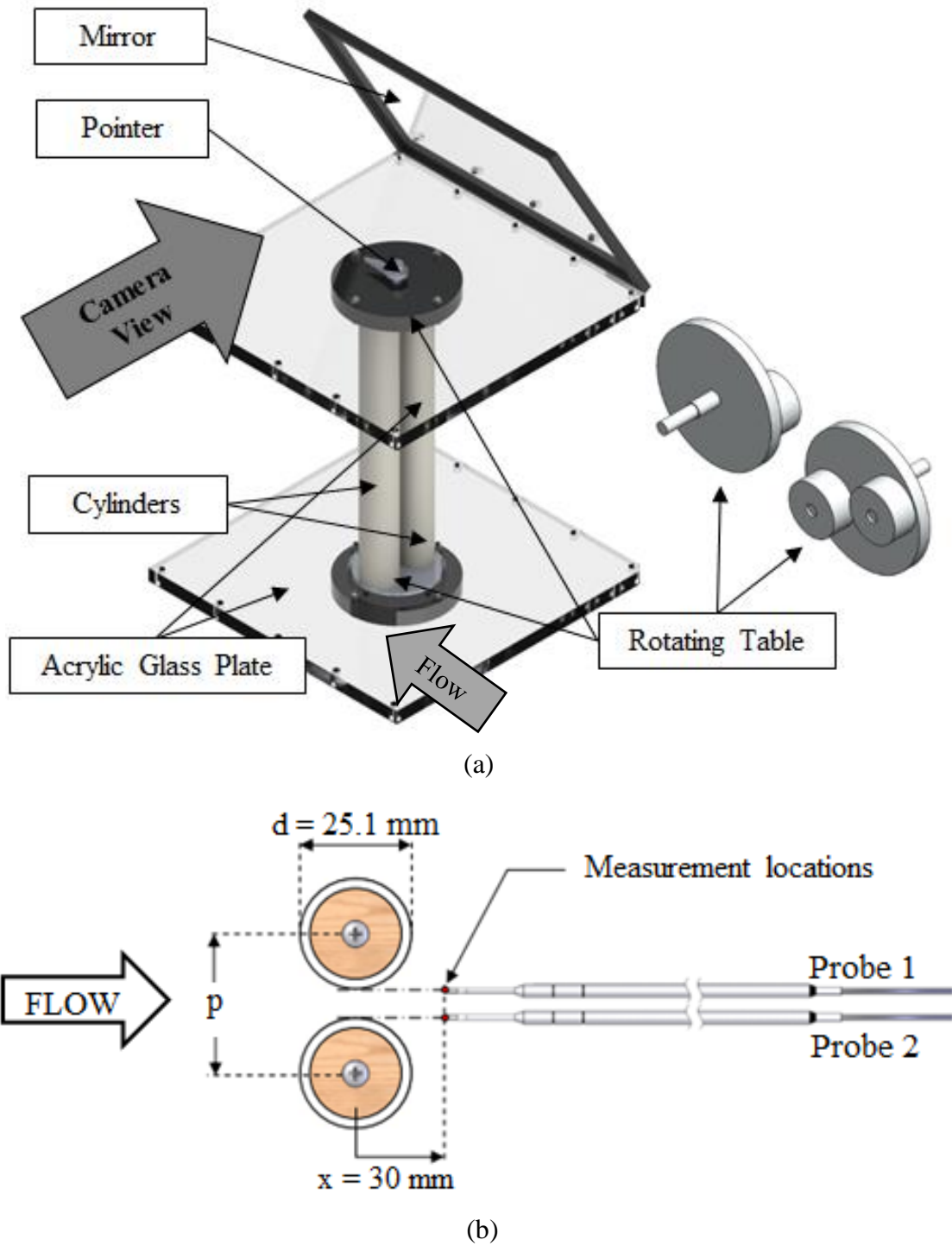


Figure 3.4 – Details about the assembly of the free to rotate cylinders (a) and probes alignment (b, adapted from De Paula, 2008).

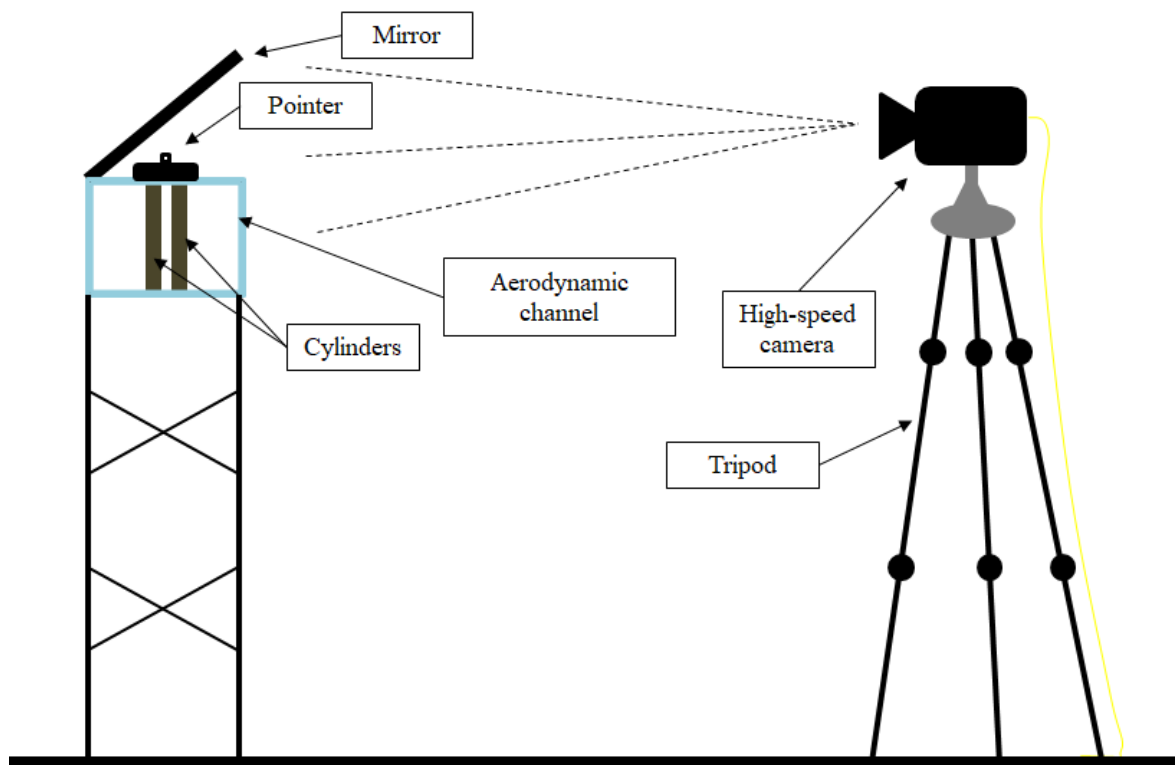


Figure 3.5 - Scheme with the aerodynamic flow channel and the high-speed camera.

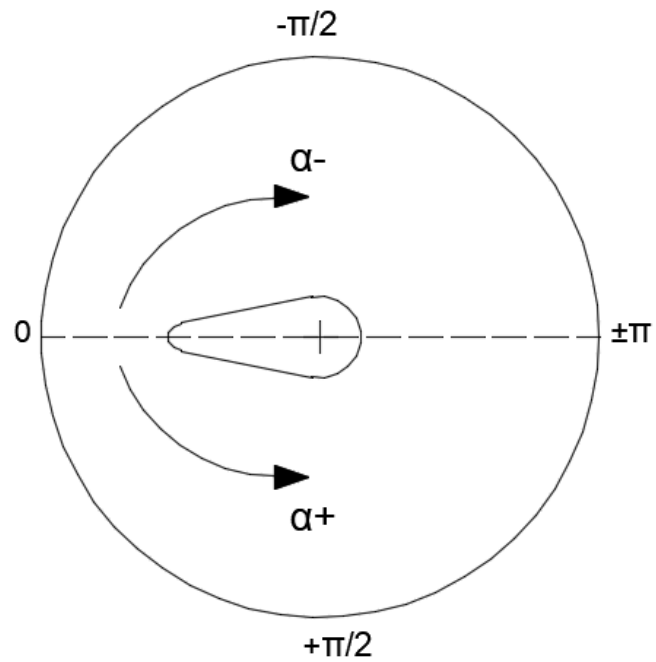


Figure 3.6 – Details about the mirror view (schematic) analyzed in the Tracker software.

The main idea of the Tracker software is tracking a physical point at each time step during the experiment by identifying in the video record the point to be tracked (Figure 3.7). In the interface is possible to analyze the real-time data and, in the case of Figure 3.7, perceive the rotation direction counter-clockwise and the values growing up in the real-time data. The time series is exported after all the points were analyzed by the software, where the parameters which were exported were the time and the angle to the flow. The data parameters are defined to track the point and must be adjusted according to the performed experiment. In the video recording, it is shown the pointer and the white background, as shown in Figure 3.6. The rectangular and circular boxes are parameters to track the point; while the circular is the “picture” for the program searching, the rectangular is the place to look for this “picture”, and the data parameters support this searching.

As the Tracker software has a limited number of storage points, the time series must be divided into blocks with 5,000 to 6,000 points and merged in one file through the Matlab software, where the graphics were generated after the analysis performed by Tracker software. The mean error for this analysis is 0.0239 rad and is explained in APPENDIX A.

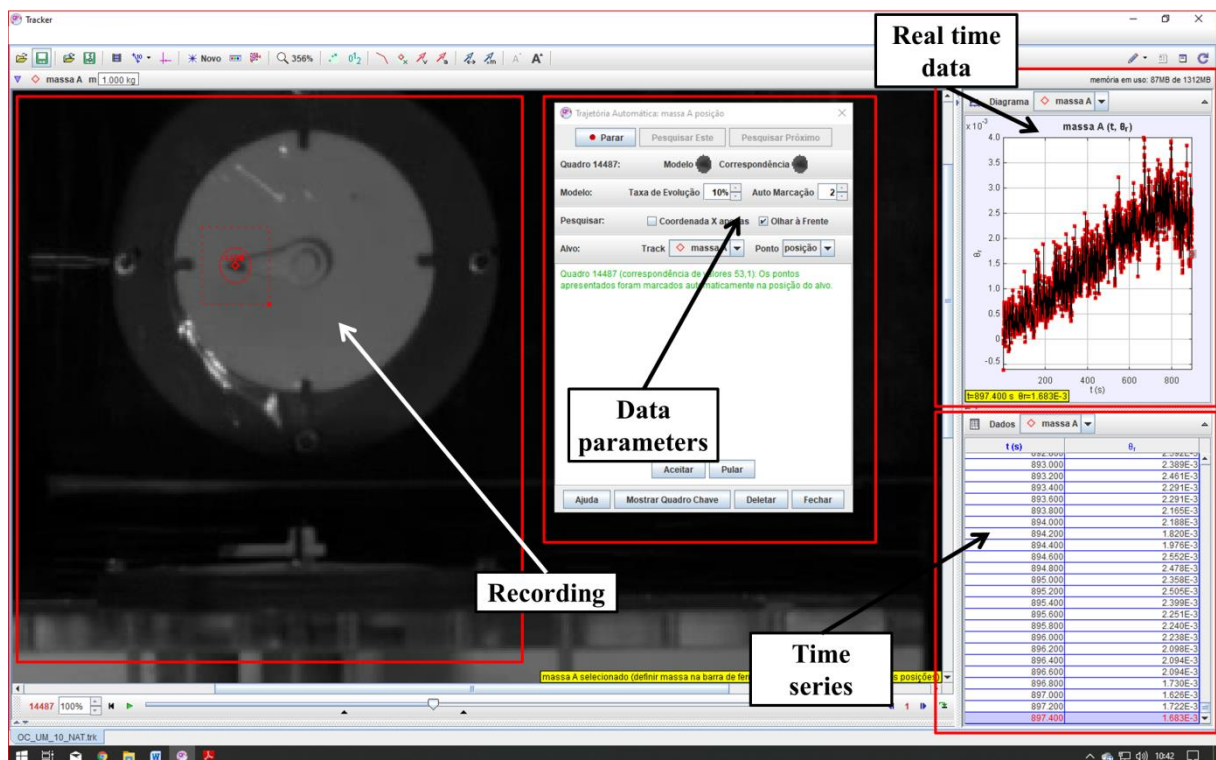


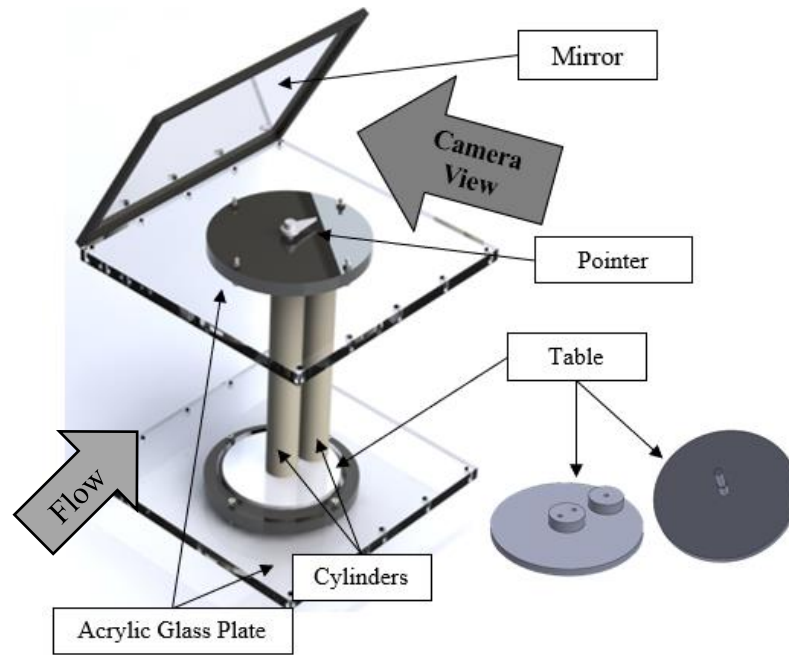
Figure 3.7 – Interface of Tracker software.

3.2.3 Free to oscillate cylinders

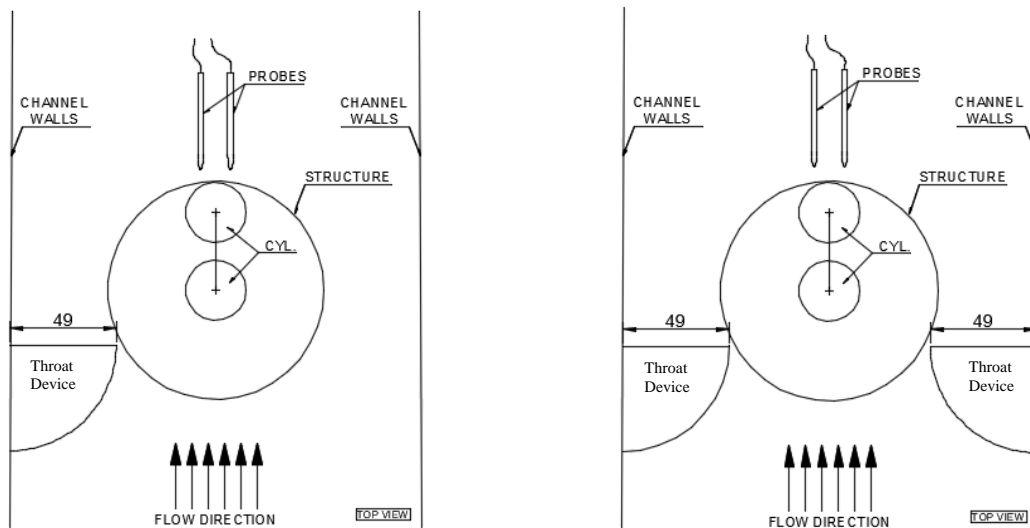
In the free to oscillate cylinders experiment, the cylinders were assembled as shown in Figure 3.8 (a). The oscillating table is coupled in the channel using low wear bearings, the same used in the cases of the free to rotate cylinders. This oscillation table is different from the case of the free to rotate cylinders (Figure 3.8a): one cylinder is coupled in the center of the assembly and a second one close to the border of the table with the same p/d used ($p/d = 1.26$). In the start position, cylinders are aligned, being the blockage ratio 13%. When the oscillation is occurring, the blockage ratio varies between 13% up to a maximum of 26%, in the case the cylinders aligned 90° to the flow. The time acquisition adopted was 32.768 s and the behavior of the assembly was analyzed using a high-speed camera, and the same methodology as explained in section 3.2.2. The pointer and the mirror, used to generate the movies for the Tracker software, were used in this experiment as well.

This experiment was explored using some aerodynamic devices to increase the oscillation level of the assembly. First, the assembly was tested naturally, without any kind of perturbation or devices installed. Then, a “throat device” 3D printed was put in the side of the channel, in order to accelerate the flow and perturb the assembly (Figure 3.8b). This “throat device” was first tested on one side of the channel, and then on both sides of the channel together (Figure 3.8c). Finally, the last test consisted in perturbing the oscillation with a blockage in the channel, and it was performed using a cylinder with 32 mm of diameter fixed in the tip of a metal rod, considering the assembly starting in natural form (without aerodynamic devices). The perturbation applied was momentary, close to the walls of the aerodynamic channel and the metal rod plus the cylinders remained in the flow channel only for a few seconds. This experiment is not related to bistability; however, since the tandem case (90°) was presented (see sec. 3.2.1), it complements those results.

For the free to oscillate cylinders, as the assembly is in the tandem position (90° with the flow), was used only one probe (Figure 3.8d). The Reynolds numbers for the experiments were 8.47×10^3 , with a reference velocity equal to 5 m/s, 1.27×10^4 with a reference velocity equal to 7.5 m/s, and 1.66×10^4 with a reference velocity equal to 10 m/s.

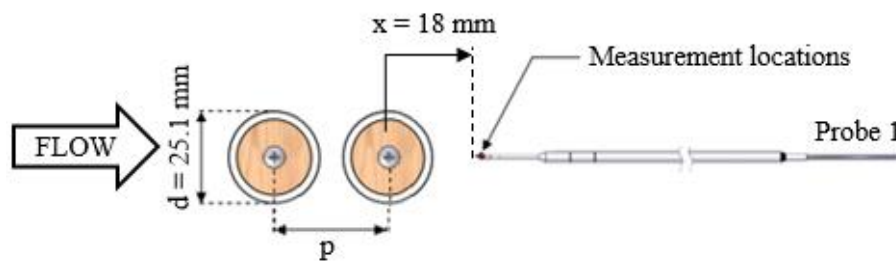


(a)



(b)

(c)



(d)

Figure 3.8 – Details about the assembly of the free to oscillate cylinders (a) and the alignment of the probe (b, adapted from De Paula, 2008).

3.2.4 Savonius wind turbine

In the wind turbine experiment, the Savonius turbine was assembled as shown in Figure 3.9 (a). The wind turbine is coupled to the acrylic glass using low wear bearings, the same structure used in the free to rotate cylinders. In the initial position, the blockage ratio of the wind turbine is 26.0%; during the rotation, the blockage ratio varies between 10.9% and 26.0%, due to the instantaneous position of the wind turbine. The time acquisition considered was 32.768 s, the same as the free to rotate cylinders. Actually, this experiment is very similar to the free to rotate cylinders, once the objective is to compare with those results.

The wind turbine employed in this experiment was a Savonius wind turbine, designed first for the engineer Sigurd J. Savonius in 1922, used by Akwa, 2014. The Savonius wind turbine has a very simple design and ensures good energy generation at a low cost. In this experiment, the wind turbine was printed in a 3D printer and coupled in the aerodynamic channel to analyze the rotational velocity and power generation.

The chosen position for the anemometers for the wind turbine is shown in Figure 3.9 (b), where the anemometers remained at a fixed distance from the wind turbine walls. The reference velocities employed in this experiment are equal to 5.4 m/s and 10 m/s, the same as the free to rotate cylinders.

The Reynolds computed for the turbine diameter and reference velocities equal to 5.4 m/s and 10 m/s are 1.66×10^4 and 3.32×10^4 . These Reynolds numbers are different from the cylinders Reynolds numbers once the characteristic length is not the same. However, the reference velocities employed in both experiments are the same, once the objective is to compare the results with the rotational cylinders.

The behavior of the wind turbine was studied using a high-speed camera, and the same methodology as explained in section 3.2.1. The pointer and the mirror, used to generate the movies for the Tracker software, were used in this experiment as well. For this case, once the main objective is comparing the results of velocity and power generated with the free to rotate cylinders, a detailed analysis of the angular behavior of the Savonius turbine will not be presented.

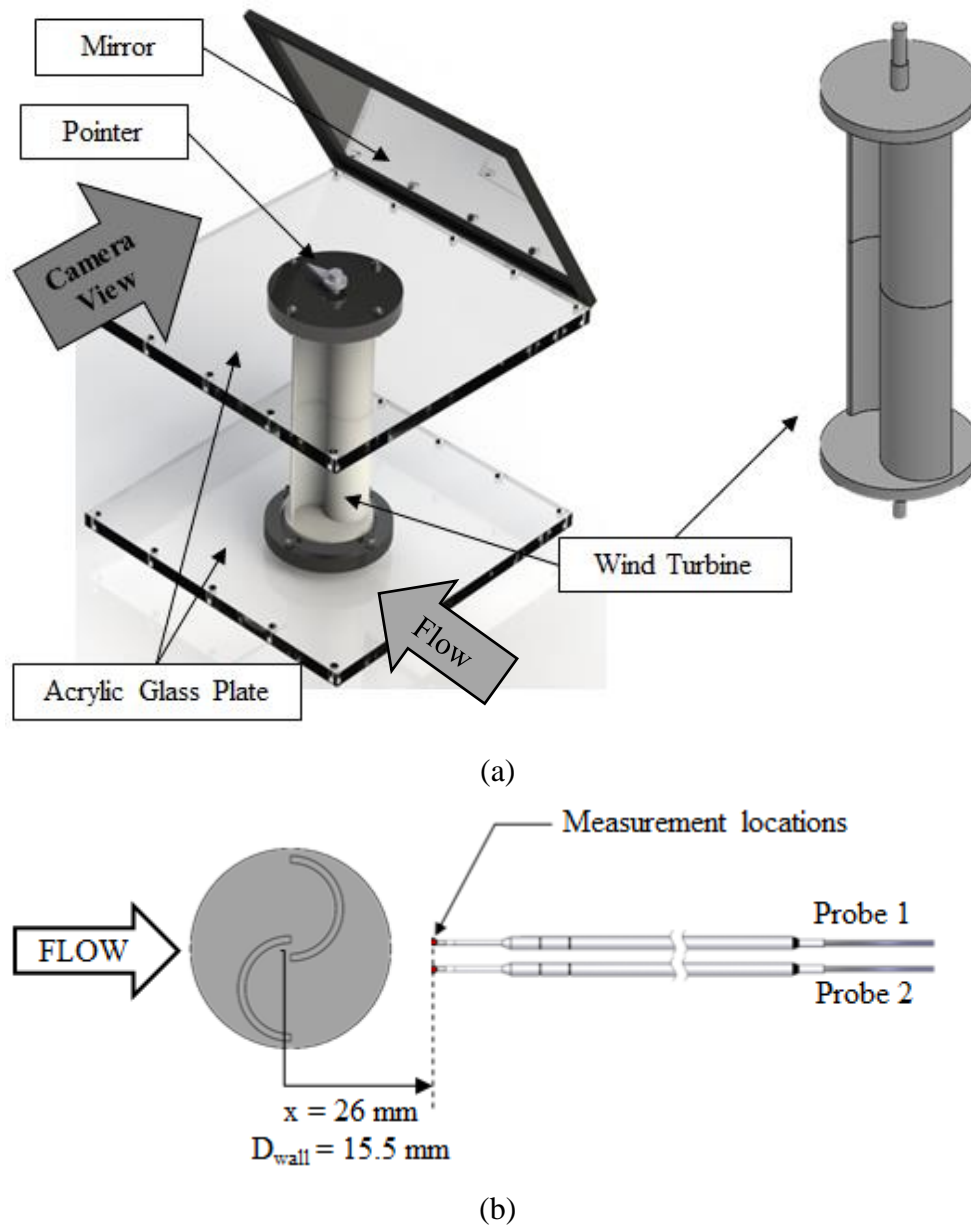


Figure 3.9 – Details about the assembly of the wind turbine (a) and the alignment of the probe (b, adapted from De Paula, 2008)

3.2.5 Electrical generation

The electric experiments performed in this work aimed to determine the electrical current and voltage generated in the experiments and then evaluate the power generated through Equation 3.1. A stepper motor from a Hard Drive Disk (HDD) Seagate 72041–240 (Figure 3.10) was employed as an electrical generator in the experiments. The rotor is a

permanent magnet system and the windings are stationary in the stator, not having a brush system. These characteristics ensure the stepper motor has low electrical losses. The specifications of the used stepper motor are described in Table 3.1. Color LEDs were connected in the generator to analyze if the studied experiment was able to light them on, as shown in Figure 3.10.

$$P = IU_e \quad (3.1)$$

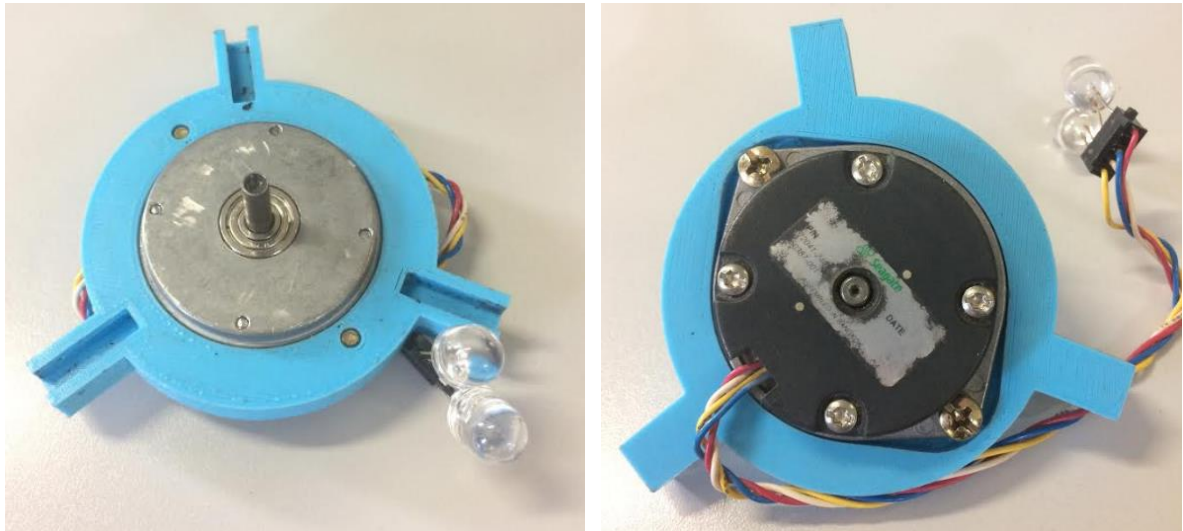


Figure 3.10 – Stepper motor employed in the electrical experiments.

Table 3.1 – Electrical specifications of the generator.

| Electrical generator specifications | |
|--|---------------|
| Type | Stepper motor |
| Brand | Seagate |
| Model | 15PM-M001-01 |
| Wires | 4 |
| Poles | 2 |
| Nominal voltage [V, D.C.] | 12 |
| Resistance [Ω] | 28 |
| Phases | 2 |

The electrical power was measured by means of two digital multimeters Minipa ET-2651 model, with basic precision of 0.1%, operating in the voltage range 200 mV – 1000 V D.C. and 2 V – 750V for A.C. measures. The range of current is 200 μ A – 20A D.C. and 20 mA – 20 A for A.C measures. The rotational velocity was measured by one digital tachometer Minipa MDT-2238A model, with 2.5 – 99,999 rpm range and basic precision of 0.05%.

3.3 Hydrodynamic flow channel

Flow visualization was performed in a water channel with a closed circuit. The channel and the visualization technique are the same used by Woyciekoski et al., 2020. The channel is made of aluminum plates with 0.8 mm thickness, with a test section made by acrylic glass to allow the visualization of the flow. The dimensions are 3.25 m long with a rectangular section with 0.146 m height and 0.193 m width, the same as the aerodynamic channel. Water was driven from a 400 L tank by a set of two Texius model TBHLI centrifugal pumps of 0.37 kW each one with a maximum flow rate of 160 L/min. The flow rate was controlled by means of two globe valves and measured by a hydrometer and a chronometer. Two honeycombs were employed to homogenize the flow. An upper plate made of acrylic glass was used to close the visualization section and to avoid the effect of gravitational waves. The water level was maintained at about 0.2 m in the test section during the experiments, 10 mm above the upper plate. This is the same procedure used successfully by Olinto et al., 2009 and De Paula et al., 2012 in a different hydraulic channel.

There are two ink tanks with colored water, injected in the flow upstream from two holes drilled on the cylinders connected to hoses with 3 mm of diameter. The amount of color dye injected is controlled by two valves in each hose. Figure 3.11 presents a detailed view of the constructive form of the hydrodynamic flow channel. Water needs to be changed every about 2 hours of the experiment, because the amount of dye contaminates the water, reducing the quality of pictures and movies.

In the present work, the visualization was taken with the cylinders in the vertical position, as in the aerodynamic flow channel, and Reynolds number 1.97×10^3 , considering the free stream velocity and tube diameter. For the video recorder, it was used a camera with a resolution of 1080 x 720 pixels and 30 frames per second, fixed on a tripod. A mirror positioned 45° with the camera was fixed on the top of the channel to visualize the side view

and the top view simultaneously, as shown in the detail of Figure 3.11. The experiment was recorded for 25 minutes.

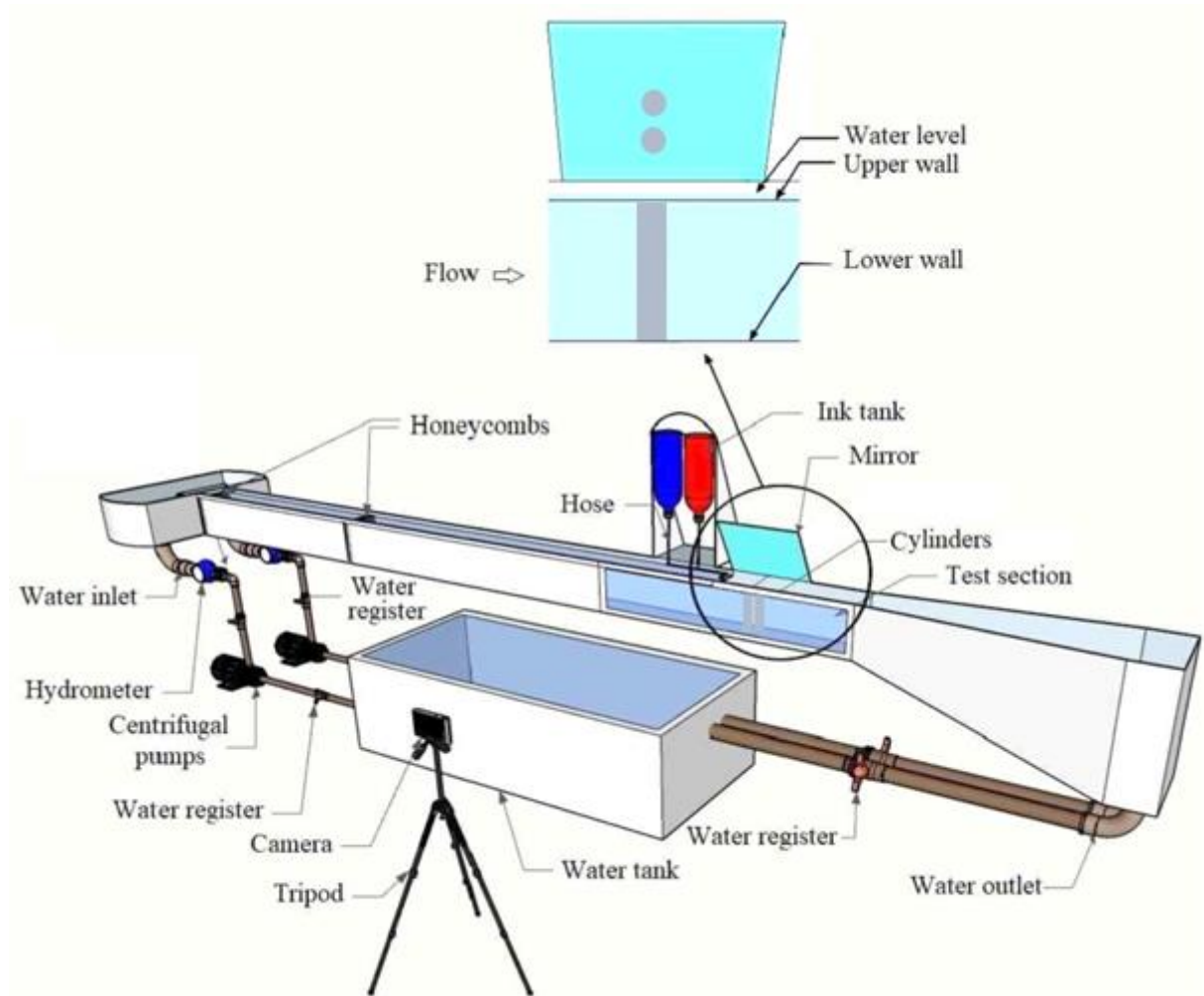


Figure 3.11 – Schematic of hydrodynamic flow channel for the visualization of the flow.

Adapted from Woyciekoski et al., 2020.

Through the analysis of the images from the visualization movies, a time series of the angle formed by the deflected flow emanating from the gap between the cylinders was generated by means of the Tracker and the Matlab software. A geometric point located at 5 mm from the cylinders was assigned, and the deflection angle, defined between the x -line (tangent to the cylinder wall and perpendicular to the flow for all the angles) and the wake

border, was measured as shown in Figure 3.12. Angles were measured at every 200 frames, corresponding to a time interval of 6.67 s and a sampling frequency of 0.15 Hz.

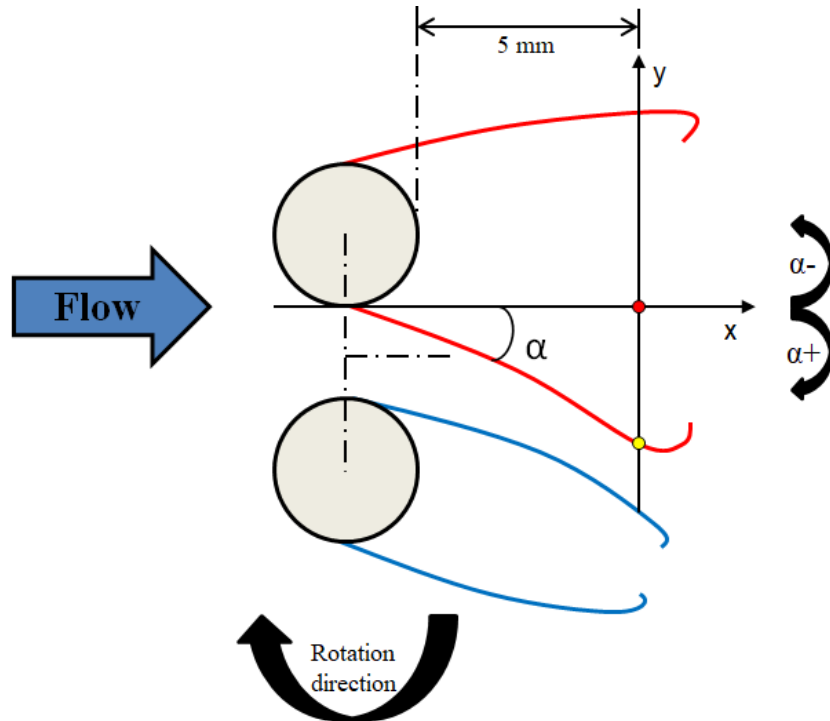


Figure 3.12 – Details about the definitions to analyze the wake angles.

An illumination system is placed over the test section, which is formed by two LED tapes with 4,8 W/m each, and a set of fluorescent lamps with 9 W of power each. The illumination system is the key for good visualizations and recordings, once the contrast and luminosity depend on it.

3.3.1 Experiments performed in the hydrodynamic flow channel

In the hydrodynamic flow channel, an experiment with the fixed cylinders was performed. The cylinders used in this experiment have the same characteristics as the ones used in the experiment in the aerodynamic flow channel, but with two thin hoses inside them to release the dye in the channel through small holes drilled in the walls. The blockage ratio remains the same as the aerodynamic flow channel, defined as 26%.

The main objective of this experiment was complementing the results for the fixed cylinders in the aerodynamic flow channel (sec. 3.2.1), allowing a new perspective for the results together. The angles applied to the flow were the same as the ones used for the similar experiment in the aerodynamic flow channel.

To assembly the setup with the two cylinders and the angles to the flow, an acrylic glass plate was designed for this experiment. Several holes spaced 5° were drilled in the plate through a laser cutting machine, ensuring good precision for the angles, as shown in APPENDIX C. This part needs to be fixed in another part, which is fixed in the hydrodynamic flow channel, shown in the APPENDIX D. Both parts were laser cut at the *Innovation and digital manufacturing laboratory of the Engineering School (LIFEELAB)* of UFRGS and were fixed together through a 3D printed part, as shown in Figure 3.13. This setup is assembled and put in the hydrodynamic channel (Figure 3.11).

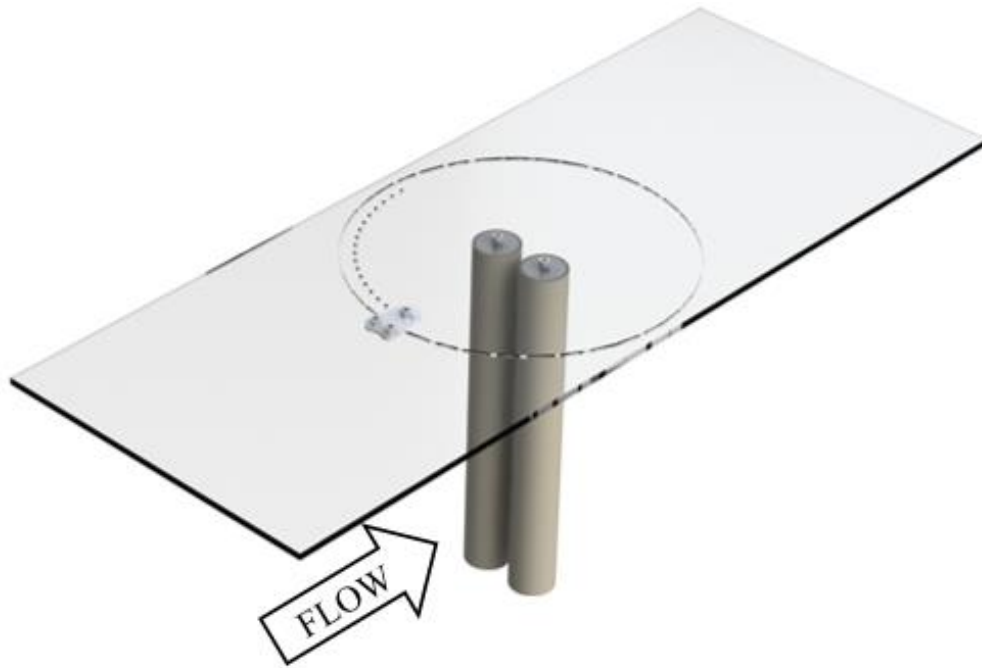
To analyze intermediate angles, the part 3D printed (Figure 3.13) has three holes to fix the acrylic parts. The middle one is the angle predetermined in the laser cut (0° , 5° , 10° and so on) and the other two holes are angularly deviated 2.5° ; it means that when one predetermined angle in the acrylic part is put in one of this holes the angle could be $+2.5^\circ$ or -2.5° than the predefined angle, as shown in Figure 3.13.

3.4 Experiments summary

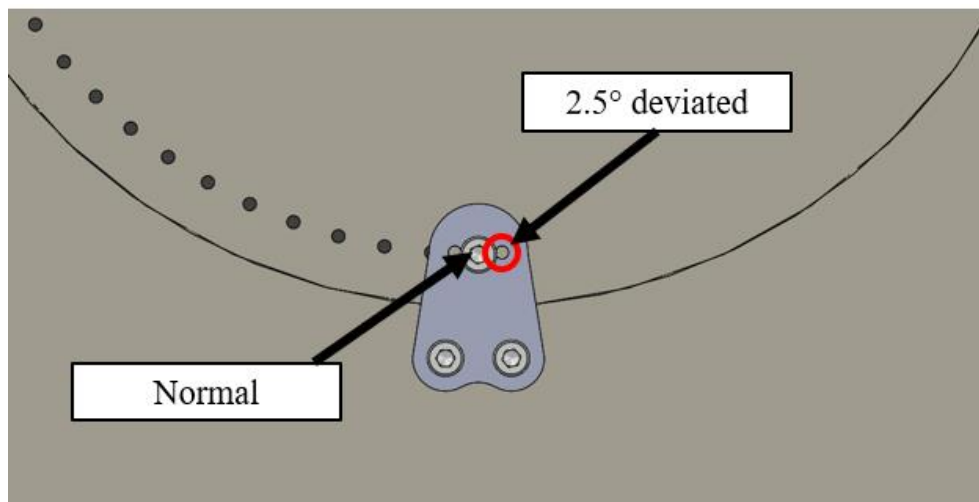
Table 3.2 summarizes the experiments performed in this work with the main objectives, the flow velocities, the section which the experimental procedures are detailed, and which channel was used.

Table 3.2 – Summary of the experiments performed in this work.

| Experiment | Flow channel | Section | U_{ref} [m/s] | Objectives |
|-------------------|---------------------|----------------|-----------------------------------|--|
| Fixed cyl. | Aerodynamic | 3.2.1 | 10 | Investigate the bistable phenomenon in several angles |
| Fixed cyl. | Hydrodynamic | 3.3 | 0.2 | |
| Rotating cyl. | Aerodynamic | 3.2.2 | 5.4,10 | Investigate the dynamic effects of the bistability and explore the ability to generate power |
| Oscillating cyl. | Aerodynamic | 3.2.3 | 5,7.5,10 | |
| Savonius turbine | Aerodynamic | 3.2.4 | 5.4,10 | |



(a)



(b)

Figure 3.13 – Fixation scheme in the hydrodynamic flow channel (a) and the details about the fixation for use angles $\pm 2.5^\circ$ than the predefined angles (b).

4 RESULTS

This section presents the results for the aerodynamic and hydrodynamic channels, for all the experiments mentioned in Table 3.2. The results are organized for the best comprehension of the methodology and chronology adopted in this work.

The aerodynamic results comprehend the velocity signal results, as well the results applying the wavelet transform analysis (CWT and DWT) and the Fourier analysis for the power spectrum generation. The electrical analysis applied for power generation is also presented. Fixed cylinders, free to rotate, free to oscillate, and wind turbine experiments are detailed in the results.

The hydrodynamic experiments comprehend the results for the fixed cylinders, where is presented the recordings performed for this experiment. Statistical analysis is also presented, considering the angle of the wakes to the flow.

4.1 Fixed cylinders – Aerodynamic channel results

The aerodynamic channel results for each angle will be shown in the next topics. The results for the side-by-side position are explained with more details, once there is more interest in the wake characteristics for this angle. Also, for 2.5° and 5° , more results were given, and for the other angles, only a short discussion was made. For the aerodynamic channel was adopted Reynolds number 1.66×10^4 , blockage ratio 26%, and 10 m/s as the free flow for all the angles.

4.1.1 Results for side-by-side cylinders (0° position)

Results of velocity measured with the hot wire probes in the wake of the side-by-side cylinders are presented in Figure 4.1 (a) and (b), where the presence of the bistable flow can be observed by the presence of two velocity levels with a high-velocity level called mode 1 and at about 15 m/s, and a low-velocity level called mode 2 and at about 4 m/s, that alternates between each other. Figure 4.1 (a) shows that the modes are inverse to the ones presented in Figure 4.1 (b), characterizing the wakes alternation. About 24 flow mode changes occurred during the experiment, which is performed during 131.072 s.

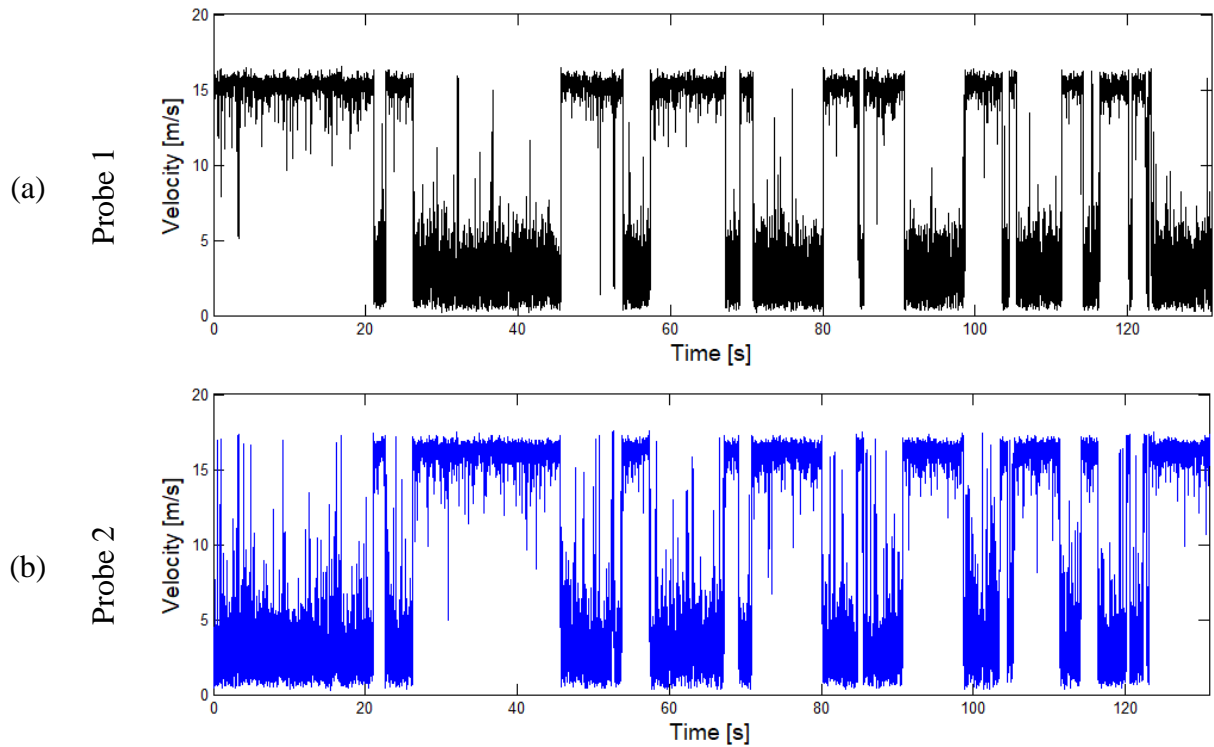


Figure 4.1 – Velocity signals from the hot wire anemometers for Probe 1 (a) and Probe 2 (b), side-by-side position.

The velocity results were statistically processed (Table 4.1), generating the results for mean, minimum, and maximum velocity values, the variance, standard deviation, skewness, and kurtosis, which were discussed in section 2.2.1. The high levels of standard deviation are presented due to the fact of each probe alternate the flow mode during the experiment, causing big differences to the mean velocity value. Low values of skewness show that the signal is reasonably symmetric to the mean value [Tennekes and Lumley, 1972].

Table 4.1 – Statistical data of velocity series for side-by-side cylinders for both probes.

| Probe | Mean vel. [m/s] | Min. vel. [m/s] | Max. vel. [m/s] | Var. [m/s] | Std. dev. [m/s] | Skewness | Kurtosis |
|-------|--------------------|--------------------|--------------------|---------------|--------------------|----------|----------|
| 1 | 9.37 | 0.17 | 16.58 | 39.65 | 6.29 | -0.15 | 1.09 |
| 2 | 9.50 | 0.29 | 17.58 | 45.02 | 6.71 | -0.02 | 1.08 |

The velocity levels can be better observed in Figure 4.2 (a) and (b), where the DWT was applied in the results of velocity signals (Figure 4.1). To reconstruct the signals in Figure 4.2, the wavelet function Db20 and level 8 was applied, generating a reconstructed signal from 0 to 3.9063 Hz. Probes 1 and 2 present different velocity levels for modes 1 and 2 showing that the process is not symmetric, in accordance with Alam et al., 2003 and De Paula and Möller, 2013. The velocity in Figure 4.2 (a) achieves the same levels that in Figure 4.2 (b), characterizing the flow alternation between the same levels of velocity. The bistable phenomenon is clearly viewed in Figure 4.2 with the filtered signal.

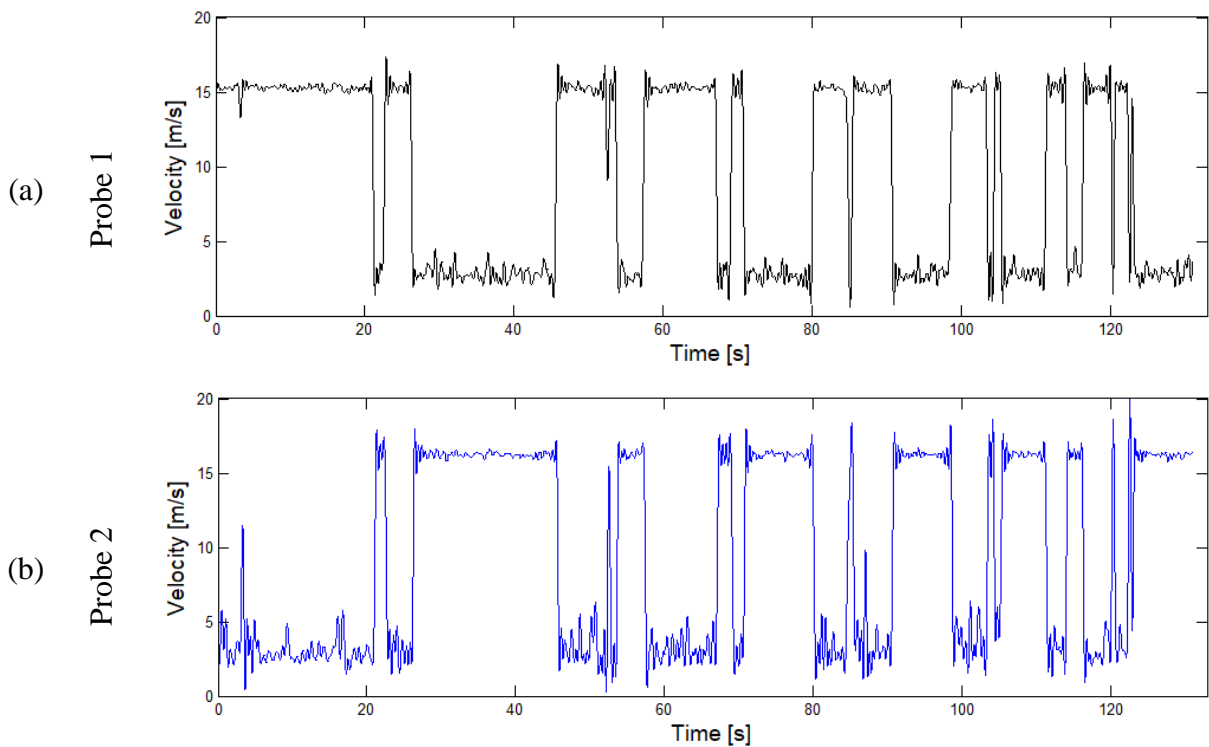


Figure 4.2 – Reconstruction of the signals using DWT for Probe 1 (a) and Probe 2 (b), side-by-side position.

The velocity series were evaluated with CWT and the results are presented in Figure 4.3 (a) and (b). This spectrogram shows the energy distribution in a frequency interval from 1 to 120 Hz, with a bandwidth of 1 Hz and the time. The highest values of energy in the arbitrary scale on the right side are reddish, as shown in the color bar, and are related to the highest values of velocity fluctuations. The lowest values of energy in the arbitrary scale are bluish and are related to the lowest values of velocity fluctuations. All the analysis presented

in Figures 4.1, 4.2, and 4.3 shows the main bistable flow characteristic, the changing in flow modes, expected for the tested spacing ratio.

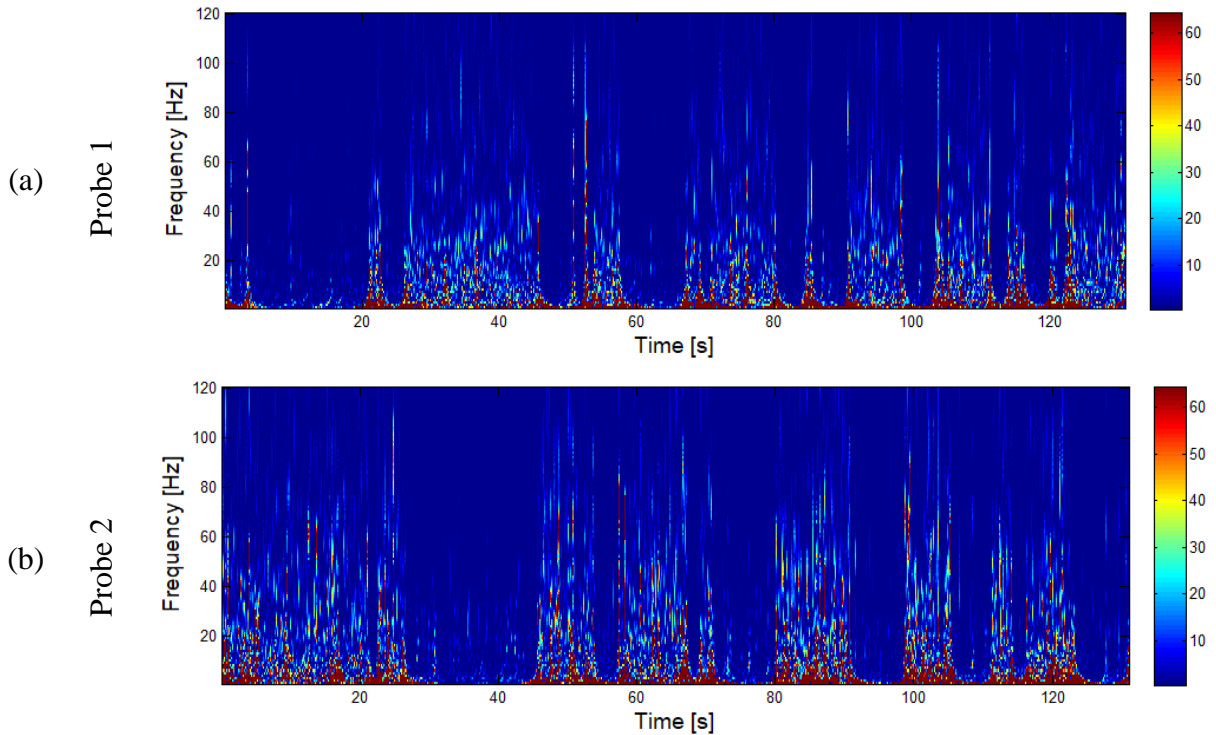
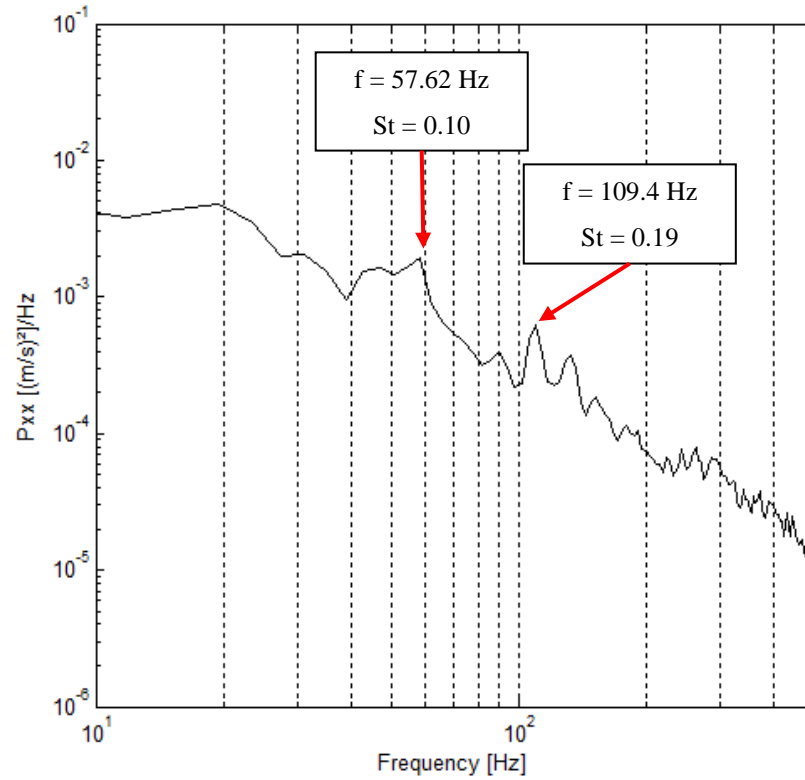
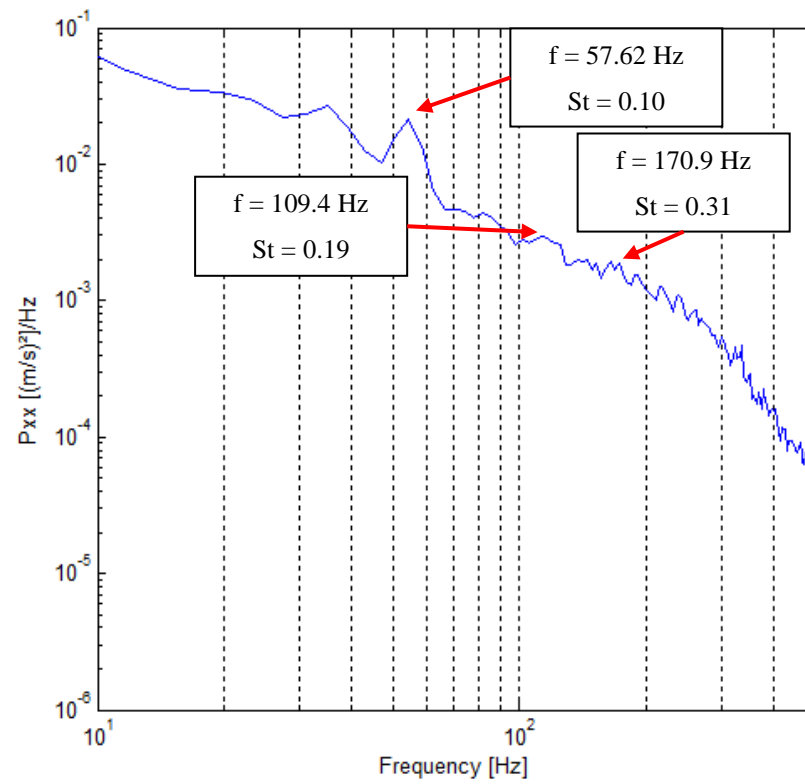


Figure 4.3 – CWT of the velocity signals for Probe 1 (a) and Probe 2 (b), side-by-side position.

The fluctuations from the velocity series in Figure 4.1 from 0 to 16.384 s were used to generate the power spectrum presented in Figure 4.4, and showed a peak in each signal. The Fourier analysis is a support tool very useful to obtain the peaks in the frequencies. However, it can be used only for ergodic signals, which is not the case for bistability. To use the Fourier analysis, in this case, were chosen the time interval 0 to 16.384 s of Figure 4.1, where each probe is in one stable state, not changing the flow mode during this time. The first peak in Probe 1 (Figure 4.4a) is at 57.62 Hz, corresponding to a Strouhal number $St = 0.10$, computed with the reference gap flow velocity (13.60 m/s) and tube diameter (25.1 mm), corresponding to the wide wake. One harmonic is observed at 109.4 Hz. The peak of interest in Probe 2 was observed at 170.9 Hz (Figure 4.4b), corresponding to a Strouhal number $St = 0.31$, related to the narrow wake. These results agree with the values presented in Alam et al., 2003 for the same p/d tested in the present analysis.



(a) Probe 1



(b) - Probe 2

Figure 4.4 – Power spectrum from velocity signals for Probe 1 (a) and Probe 2 (b), 0° position.

Strouhal numbers were also computed for the reference velocity (10 m/s) and the tube diameter, considering the same frequency peaks, generating the Strouhal numbers $St = 0.146$ and $St = 0.446$. The results of Figure 4.4 are complementary to those obtained by the CWT presented in Figure 4.3.

4.1.2 Results from 2.5° to 35° positions

This section discusses the results about the angles up to 35°, which represents the last angle between the shadow angle defined before (sec. 3.2.1). Results for 2.5° are shown in Figure 4.5. Figure 4.5 (a) and (b) show the reconstructed velocity signals (DWT) for both probes. The presence of only one high level of velocity for both probes and high intensity in the velocity fluctuations for Probe 1 (Figure 4.5a) suggests that the probes are in the gap flow, with Probe 1 close to the border of one wake. For Probe 1, the mean velocity along the time is 14.90 m/s, and for Probe 2, the mean velocity is 14.83 m/s. Some attempts to modify the flow mode were perceived (Figure 4.5a), but a second and stable state was not achieved.

In Figure 4.5 (c) and (d), the CWT of the velocity signals is presented, considering the arbitrary scale of energy on the right with 1 Hz bandwidth. For Probe 1 (Figure 4.5c), the energy presents some peaks very similar to the ones presented in Figure 4.3 (a) and (b), but in this case, the bistability phenomenon did not occur. Probe 1 (Figure 4.5c) presents energy distribution in frequencies until 50 Hz and some peaks at about 80 Hz. Probe 2 (Figure 4.5d) presents energy concentration in frequencies until 30 Hz and some peaks at about 60 Hz, showing that the velocity fluctuations are related to higher energy values.

Results for 5° are shown in Figure 4.6. Figure 4.6 (a) shows the velocity signals for both probes. The presence of two levels of velocity suggests that Probe 1 is in the gap flow and Probe 2 is in the wake, once the wake has lower values of velocity than the gap flow (Figure 2.3). For Probe 1, the mean velocity along time is 14.2 m/s, and for Probe 2 the mean velocity is 2.63 m/s. Figure 4.6 (b) shows the reconstructed signals of velocity (DWT), where two attempts to modify the flow mode are perceived at about 100 s, but a second and stable state was not achieved.

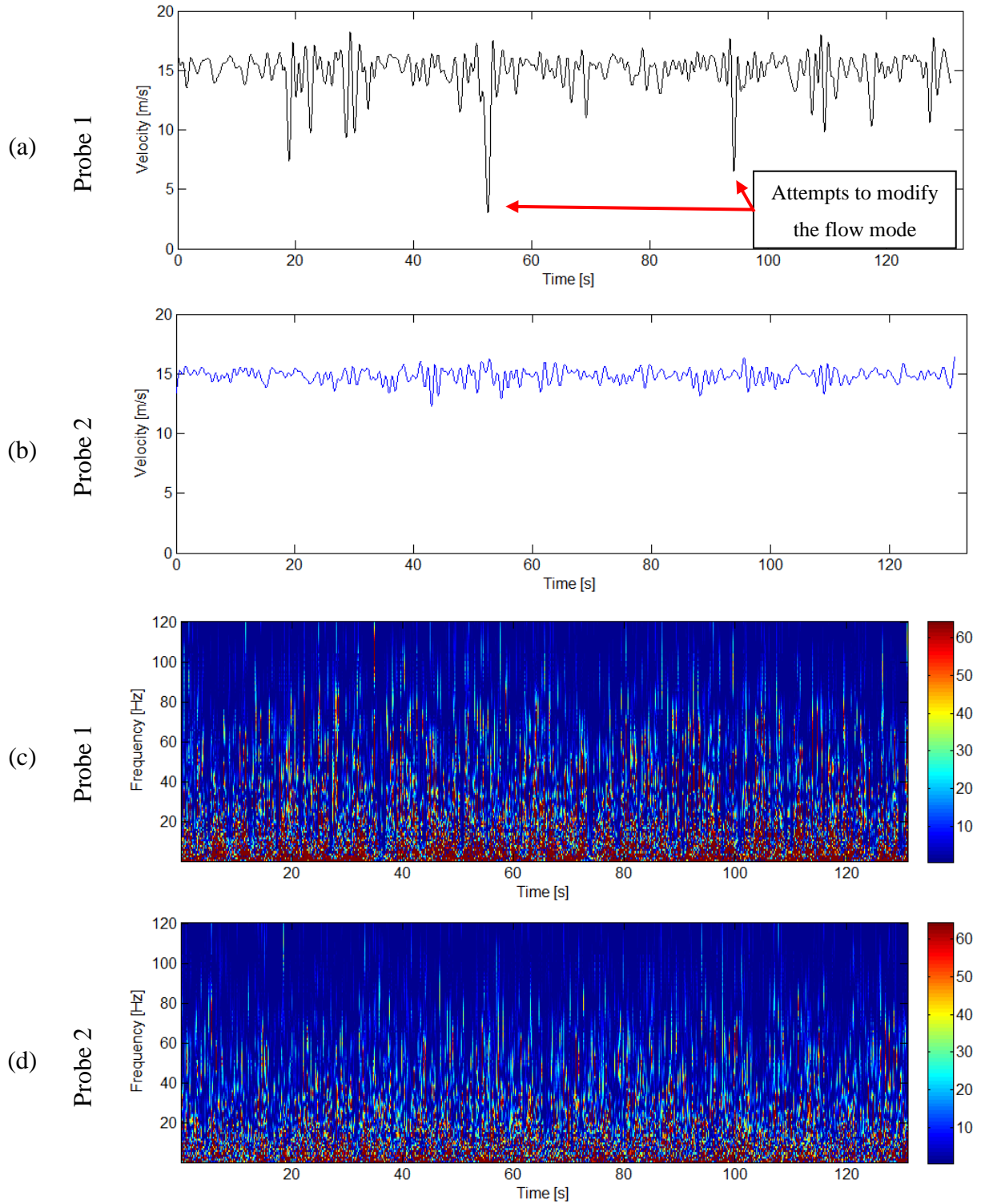


Figure 4.5 – Reconstruction of the signals using DWT for Probe 1 (a) and Probe 2 (b), CWT for the velocity signals for Probe 1 (c) and Probe 2 (d), for the flow incidence angle of 2.5° .

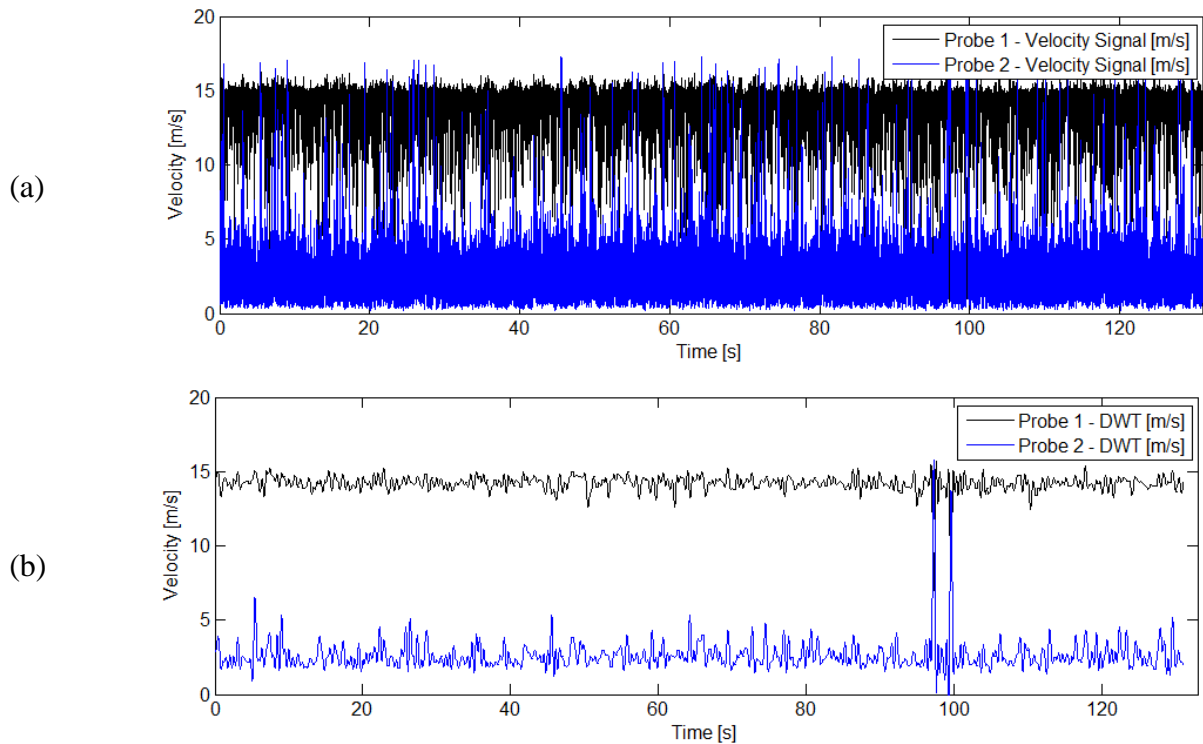


Figure 4.6 – Results of velocity signals (a) and their reconstruction using DWT (b), flow incidence angle of 5° .

In Figure 4.7 (a) and (b) the CWT of the velocities signals are shown for Probe 1 (Figure 4.7a), where energy is distributed from 1 up to 50 Hz, and for Probe 2 (Figure 4.7b) the energy is distributed since 1 up to 40 Hz, considering the arbitrary scale of energy on the right and 1 Hz as bandwidth. Energy concentration is present in the lower values of frequency at about 100 s for Figure 4.7 (a) due to the attempts to modify the flow mode shown in Figure 4.6 (b).

Figure 4.8 (a, b, and c) shows the reconstructed signals using DWT for the angles 15° , 25° , and 35° , respectively. For these angles, the probes are in only one flow mode. No flow mode changes occurred during these experiments. Despite the fact that in Figure 4.8 (a) two levels of velocity are present, the mean velocity of Probe 1 is 7.49 m/s, which is lesser than half of the gap flow velocity (13.60 m/s), suggesting that, for this angle, the Probe 1 is somewhere over the main flow between the border of the wake and the gap flow.

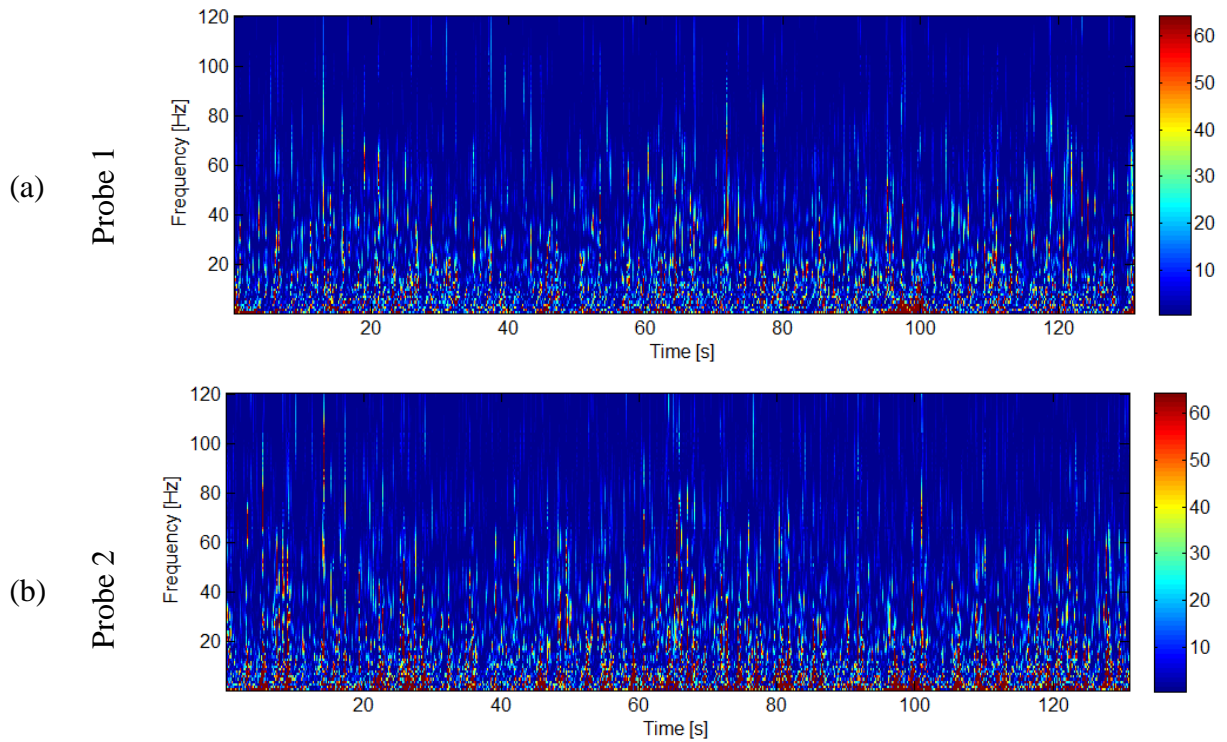


Figure 4.7 - CWT for the velocity signals for Probe 1 (a) and Probe 2 (b), flow incidence angle of 5° .

The velocity results for Probe 1 and Probe 2 and all the angles presented in this section were statistically processed, generating the data shown in Table 4.2. The mean values are bigger for the incidence angles 2.5° and 5° and probes which were located in the gap flow during the experiments. The standard deviation presented higher values for Probe 1 and incidence flow angle of 2.5° , where the flow oscillated and presented two attempts to modify the flow mode. Standard deviation also presented a high value for Probe 1 for incidence flow angle 15° , where several oscillations were perceived during the experiment. High values of kurtosis are presented for both probes of flow incidence angle of 5° , which represents that the function presents high values in the tails [Tennekes and Lumley, 1972]. The values of mean velocity for the flow incidence angles 15° , 25° and 35° presented similar and low values, once for these three cases the probes were only in one wake. Skewness values do not present a trending behavior, once the peaks presented in some flow incidence angles varied only in one direction (Figure 4.5a, from high values to low values), not generating good symmetry.

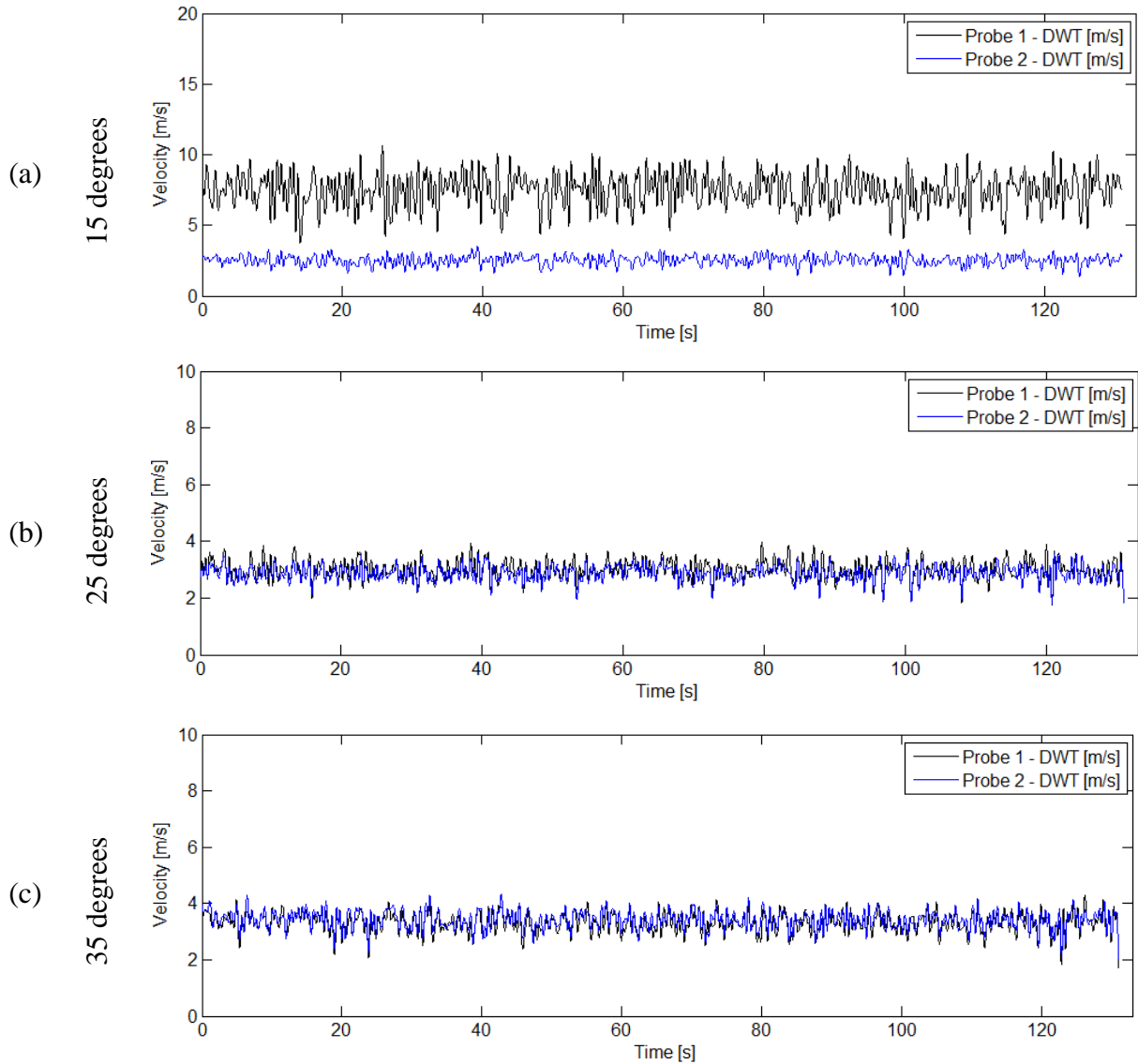


Figure 4.8 – Reconstructed signals of velocities using DWT for 15° (a), 25° (b), and 35° (c).

Table 4.2 – Statistical data for velocity results for 2.5° to 35° and both probes.

| Ang.°/ Probe | Mean vel. [m/s] | Std. dev. [m/s] | Skewness | Kurtosis | Ang.°/ Probe | Mean vel. [m/s] | Std. dev. [m/s] | Skewness | Kurtosis |
|-----------------|-----------------------|-----------------------|----------|----------|-----------------|-----------------------|-----------------------|----------|----------|
| 2.5/1 | 14.90 | 3.38 | -2.47 | 8.33 | 2.5/2 | 14.83 | 2.10 | -2.17 | 8.51 |
| 5/1 | 14.19 | 1.34 | -3.47 | 21.11 | 5/2 | 2.63 | 1.92 | 3.71 | 23.42 |
| 15/1 | 7.49 | 3.92 | 0.58 | 2.42 | 15/2 | 2.52 | 1.45 | 1.61 | 10.80 |
| 25/1 | 3.00 | 1.78 | 2.10 | 12.67 | 25/2 | 2.88 | 1.51 | 0.87 | 3.90 |
| 35/1 | 3.31 | 1.72 | 1.08 | 5.22 | 35/2 | 3.42 | 1.68 | 0.88 | 4.02 |

4.1.3 Results for 45° to 75° positions

Figure 4.9 (a, b, c, and d) shows the reconstructed signals using DWT for the angles 45°, 60°, and 75° respectively, for both probes. For these angles, the probes have only one flow mode. No flow mode changes occurred during these experiments, as happened in Figure 4.8. Also, the velocity levels were decreasing as long the angles were increasing.

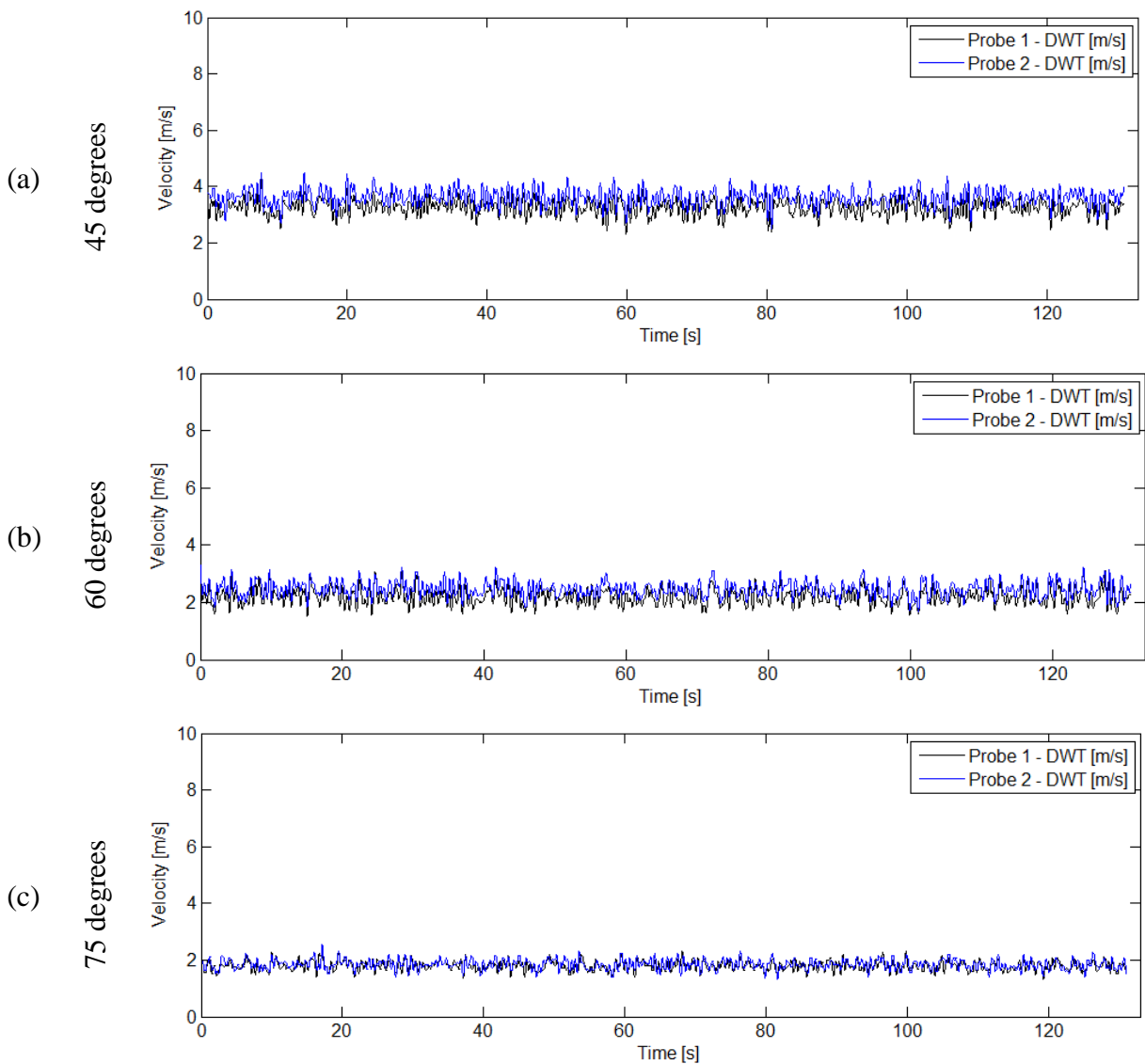


Figure 4.9 – Reconstructed signals of velocities using DWT for 45° (a), 60° (b), and 75° (c).

Table 4.3 presents the statistical results for both probes and all the angles of this section. Mean values of velocity are low for all the incidence flow angles, once the probes are in the wake. The standard deviation and skewness also presented low values, due to the fact that the oscillations are not intense for these incidence flow angles. Kurtosis presented higher values for incidence angle 45° , where the velocity fluctuations were bigger than the other angles, but still is lesser than the results in sections 4.1.1 and 4.1.2.

Table 4.3 – Statistical data for velocity results for 45° to 75° and both probes.

| Ang. [°] /Probe | Mean vel. [m/s] | Std. dev. [m/s] | Skewness | Kurtosis |
|--------------------|-----------------|-----------------|----------|----------|
| 45/1 | 3.26 | 1.64 | 1.12 | 4.84 |
| 45/2 | 3.60 | 1.68 | 0.89 | 4.18 |
| 60/1 | 2.20 | 1.20 | 1.03 | 4.42 |
| 60/2 | 2.46 | 1.22 | 0.78 | 3.61 |
| 75/1 | 1.79 | 1.00 | 0.89 | 3.69 |
| 75/2 | 1.84 | 1.02 | 0.77 | 3.33 |

4.1.4 Results for tandem configuration (90° position)

Figure 4.10 presents the DWT for the tandem position (90°), where low values of velocity are presented throughout the experiment and the probes have only one flow mode. Statistical results are presented in Table 4.4. The values of mean velocity and standard deviation are lesser than the other sections (4.1.1, 4.1.2, and 4.1.3), once the probes present lower levels of velocity and are in the wake. Skewness and kurtosis presented low values since the function is reasonably symmetric and there are no peaks in the tails.

Table 4.4 – Statistical data for velocity results for tandem position and both probes.

| Probe | Mean vel. [m/s] | Std. dev. [m/s] | Skewness | Kurtosis |
|-------|-----------------|-----------------|----------|----------|
| 1 | 1.31 | 0.70 | 0.89 | 3.75 |
| 2 | 1.57 | 0.79 | 0.74 | 3.52 |

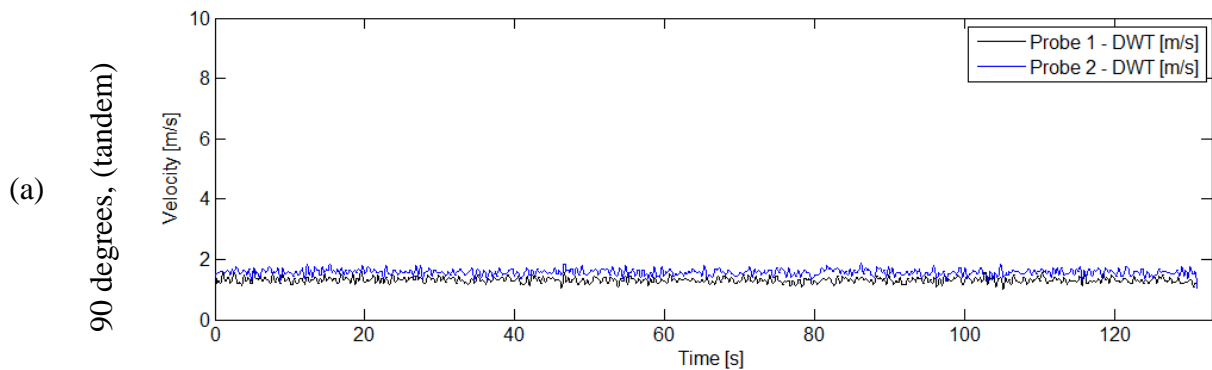


Figure 4.10 – Reconstructed signals of velocities using DWT for 90° and both probes.

4.2 Fixed cylinders – Hydrodynamic flow channel results

Visualization in a hydrodynamic flow channel was performed with the Reynolds number equal to 1.97×10^3 with the same geometry employed in the aerodynamic flow channel. Despite the fact that the Reynolds numbers are different between the experiments performed in hydrodynamic and air channels, both are included in the subcritical flow range [Blevins, 1990], resulting in wakes with similar geometric characteristics.

4.2.1 Results for side-by-side cylinders (0° position)

Through the flow visualization, it was possible to see the two wakes developed by this phenomenon. For the angle 0°, the changes in flow modes occurred, in accordance with the results presented for the aerodynamic flow channel in Figure 4.1 and Figure 4.2. Some photos about the bistability phenomenon for the side-by-side position are shown in Figure 4.11.

During the process shown in Figure 4.11, the wake behind cylinder 1 is 40 mm width ($O \sim 1.6d$) and the wake behind cylinder 2 is 30 mm width ($O \sim 1.2d$) at the beginning of the observation time considered in Figure 4.11 (a). Then, the flow became unstable, with the wakes oscillating between the states of Figure 4.11 (a) and (b), until the flow had been a low bit biased to the left side (Figure 4.11c) and, finally, became stable in another flow mode (Figure 4.11d), where the wake in the cylinder 1 is 30 mm width ($O \sim 1.2d$) and the wake in the cylinder 2 is 42 mm width ($O \sim 1.7d$). This phenomenon occurred only once throughout the

observation time, about 25 minutes. It was also observed the oscillation between the states of Figure 4.11 (a) and (b) more times, but without flow mode changes in these occurrences. These results are in agreement with those found by De Paula, 2008 and Destefani, 2016.

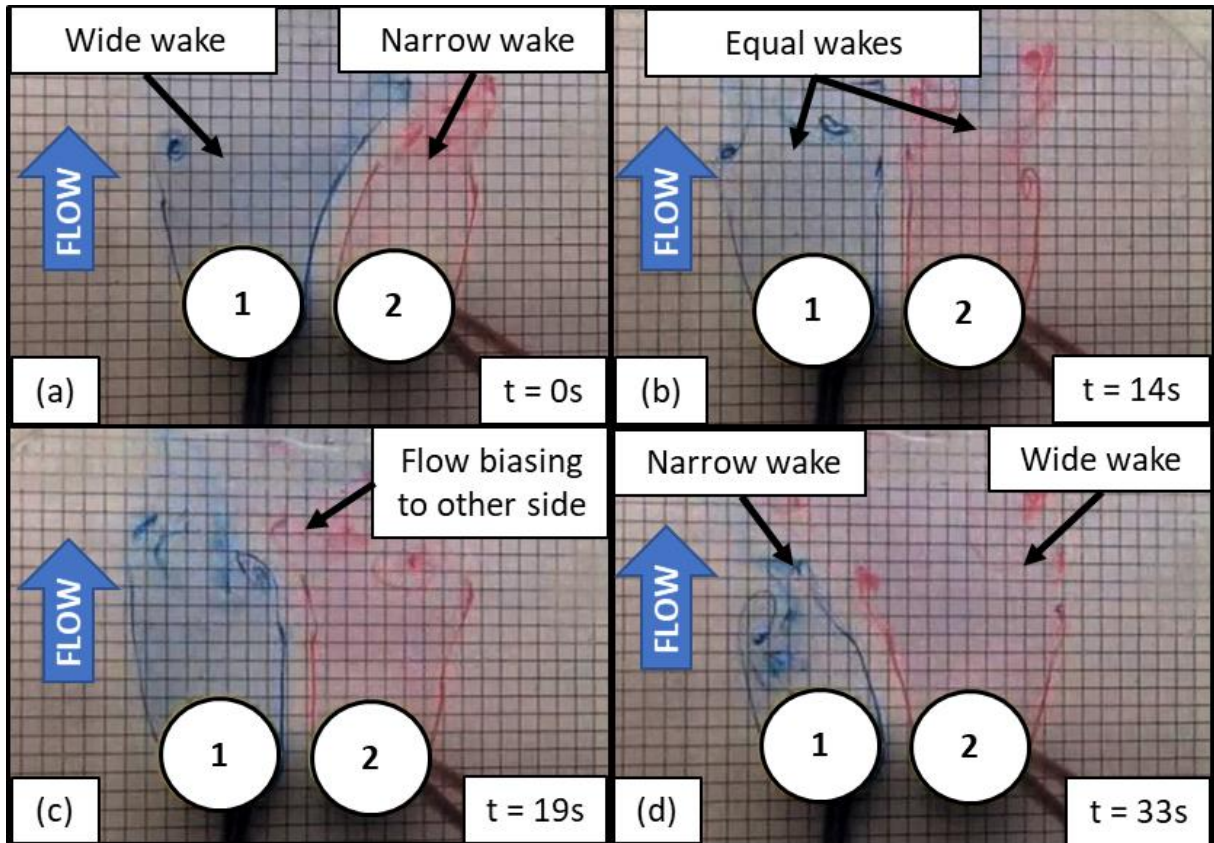


Figure 4.11 – Photos from the visualization of the bistable flow phenomenon (side-by-side position).

The time series generated for the side-by-side cylinders are shown in Figure 4.12 (a), considering the details described in Figure 3.12. The flow started with the gap flow biased to the right side with oscillations until the wake became unstable and the process described in Figure 4.11 happened. During this process, which occurred at about 300s in Figure 4.12 (a), the wake came out from $+9.2^\circ$ and went to -13° . After the gap flow had changed to the left side, the flow remained on the same side during the whole experiment, but a lot of oscillations were visualized.

4.2.2 Results for 2.5° up to 90°

Results for the time series generated for the flow incidence angle 2.5° (Figure 4.12b) showed a flow mode change at about 1182 s, where in Figure 4.13 the process is described. A sample with 67 s was extracted from the recordings, so that in Figure 4.13 (a) $t=0$ s represents the time of 1160 s in the recordings (Figure 4.12b). Figure 4.13 (a) shows the wakes stable in one mode, forming a narrow and wide wake, with the gap flow biased to the left side. Then, the wake became unstable, alternating between equal wakes (Figure 4.13b) and two different wakes, one narrow and one wide (Figure 4.13c). Suddenly, the gap flow is biased to the right side (Figure 4.13d), and the flow achieve another stable state, so that in Figure 4.13 (e) the flow is stable in another mode, with two different wakes, one wide and one narrow, but now the gap flow is biased to the right side. After this process, this flow mode remained stable during the rest of the experiment. This process is very similar to the process presented for side-by-side cylinders in Figure 4.11.

In the other angles (5° to 90°), the gap flow started and remained biased for all the angles from 5° to 90° during the whole experiment, as shown in Figure 4.12 (c) up to (j), respectively. For these angles, the gap flow was biased according to the flow incidence angle and was not perceived any flow mode changes, in accordance with the results presented for the aerodynamic flow channel in Figure 4.6, Figure 4.8, and Figure 4.9. The wakes formed in these angles are presented in Figure 4.14 for the angles 5° (a), 15° (b), 25° (c), 35° (d), 45° (e), 60° (f), 75° (g) and 90° (h).

Statistical data from Figure 4.12 are presented in Table 4.5 and Figure 4.15, where the minimum and maximum angle represents the extreme value reached by the deviated flow at every analyzed angle. For the side-by-side configuration (0°) and for 2.5°, where the bistability phenomenon occurred, the statistical data are very similar, with positive and negative values corresponding to the positive or negative deflection angle of the switching process. For all remaining angles, the deflection is positive, corresponding to the orientation of the cylinders. For angles up to 60°, the minimal and maximum angles increased, as well the mean angle, as the angular position increased. For 75°, the wake is much deviated due to the position of the cylinders, generating oscillations with large amplitudes, as shown in Figure 4.12 (i). The standard deviation characterizes the oscillations in the wake, being more noticeable for the angle 75°, due to the oscillations observed, and for side-by-side and 2.5°

cases, where the bistability phenomenon is present. These results are complementary to those presented by Habowski et al., 2019.

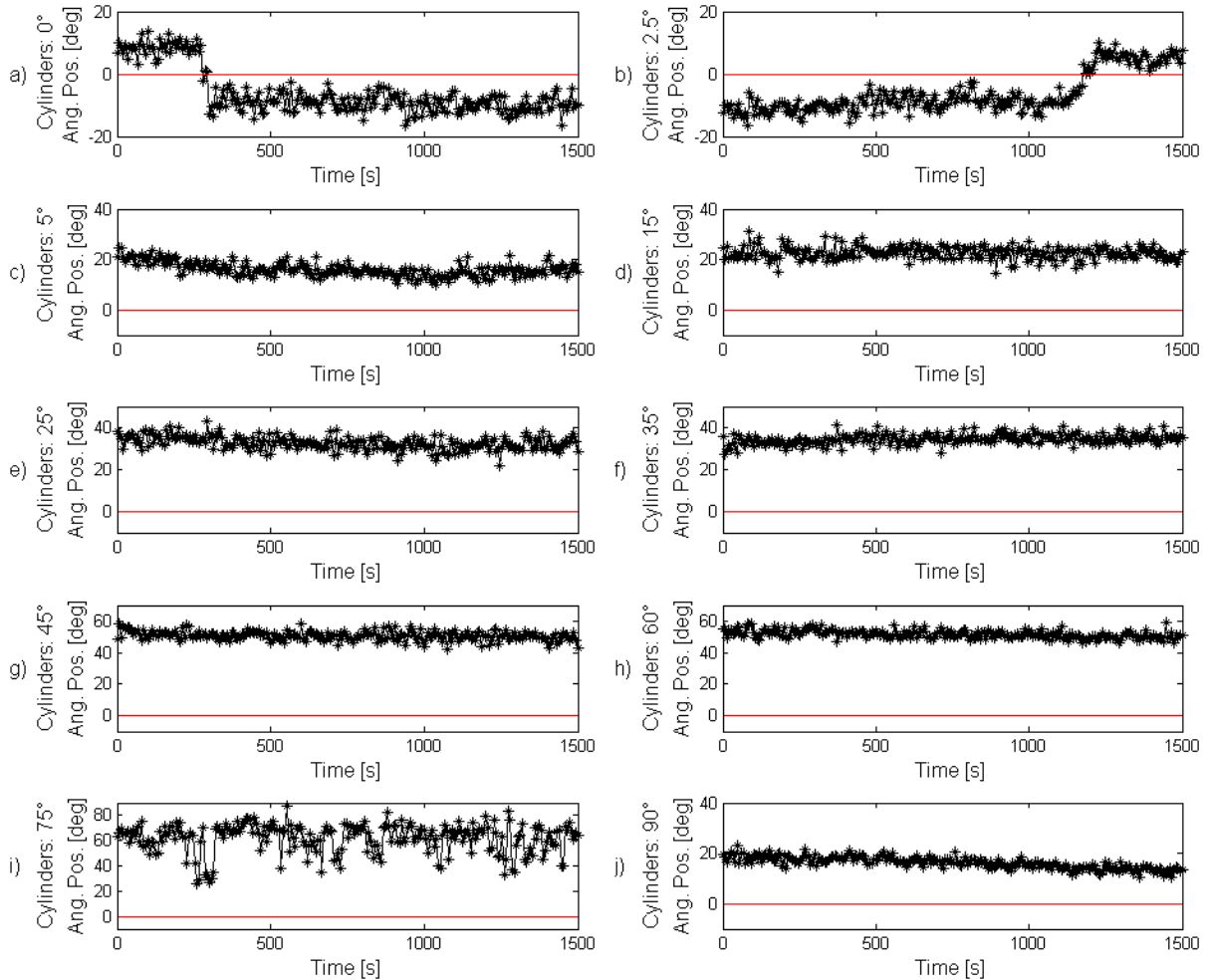


Figure 4.12 – Results of flow visualization for side-by-side cylinders (a), 2.5° (b), 5° (c), 15° (d), 25° (e), 35° (f), 45° (g), 60° (h), 75° (i) and 90° (j).

The results of flow incidence angle of 2.5° were not expected. Since the results for the aerodynamic flow channel did not present flow mode changes (Figure 4.5), it was expected that the hydrodynamic visualization (Figure 4.12b) also did not present flow mode changes, but the experiment presented one flow mode change. These results suggest that the inertia, perturbations, and the scales involved in this phenomenon may affect the results obtained.

The results of velocity for 5° (Figure 4.6) showed some attempts of changing the flow mode, but the flow is stable in one single mode. The results of flow visualization for 5°

(Figure 4.12c) showed only one stable flow mode, with the gap flow biased during all the experiment, being very similar to the behavior of angle 15° , shown in Figure 4.16, and several disturbances in the wake were observed, even in the vertical direction (Figure 4.16b). The results for this flow incidence angle can be compared with the results obtained by De Paula and Möller, 2013, where the flow has two stable states, but the authors found a path that the flow tries to switch from an initial stable mode to another one, but cannot achieve this second state, and then goes back to the first.

Table 4.5 – Statistical data for analyzed angles in the hydrodynamic channel. The positive signal means that the angle is in the same direction as the rotated angle.

| Angular position ($^\circ$) | Min. angle ($^\circ$) | Max. Angle ($^\circ$) | Mean angle ($^\circ$) | Std. deviation ($^\circ$) |
|-------------------------------|-------------------------|-------------------------|-------------------------|-----------------------------|
| 0 | -16.38 | 13.58 | -5.89 | 7.49 |
| 2.5 | -16.51 | 9.82 | -6.33 | 6.48 |
| 5 | 10.16 | 24.68 | 16.10 | 2.84 |
| 15 | 14.35 | 31.23 | 22.58 | 2.50 |
| 25 | 22.01 | 43.25 | 32.61 | 3.23 |
| 35 | 27.18 | 40.98 | 34.44 | 2.37 |
| 45 | 41.80 | 58.02 | 50.65 | 2.84 |
| 60 | 45.94 | 58.94 | 51.58 | 2.53 |
| 75 | 25.81 | 87.69 | 61.84 | 11.67 |
| 90 | 10.47 | 22.93 | 16.23 | 2.26 |

In Figure 4.16 the top and side views for the angle 15° are detailed. It is possible to perceive two different wakes in Figure 4.16 (a): a narrow wake, with about 30 mm of width ($O \sim 1.2d$), and a wide wake, with 43 mm of width ($O \sim 1.7d$). Figure 4.16 (b) shows that the flow in blue color is biased to the downside, and this oscillated upwards and downwards during the observation time.

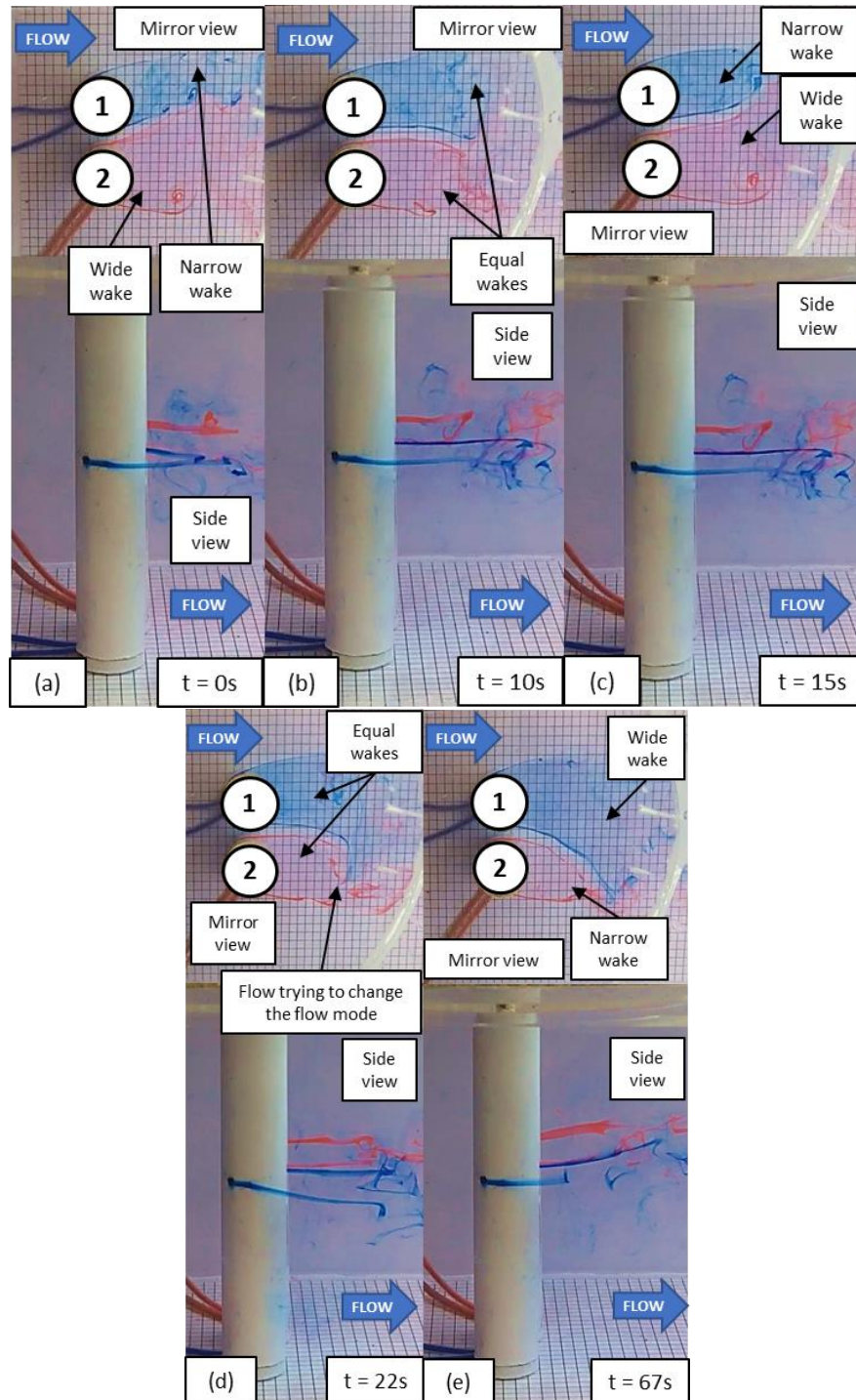


Figure 4.13 - Wake behavior behind cylinders for flow incidence angle of 2.5° ; flow biased to the left side (a), flow with equal wakes (b), returning to the left-biased flow (c), formation of two equal wakes with an attempt to change the flow mode (d) and, finally, the flow mode change, with the flow deviated to the right side (e).

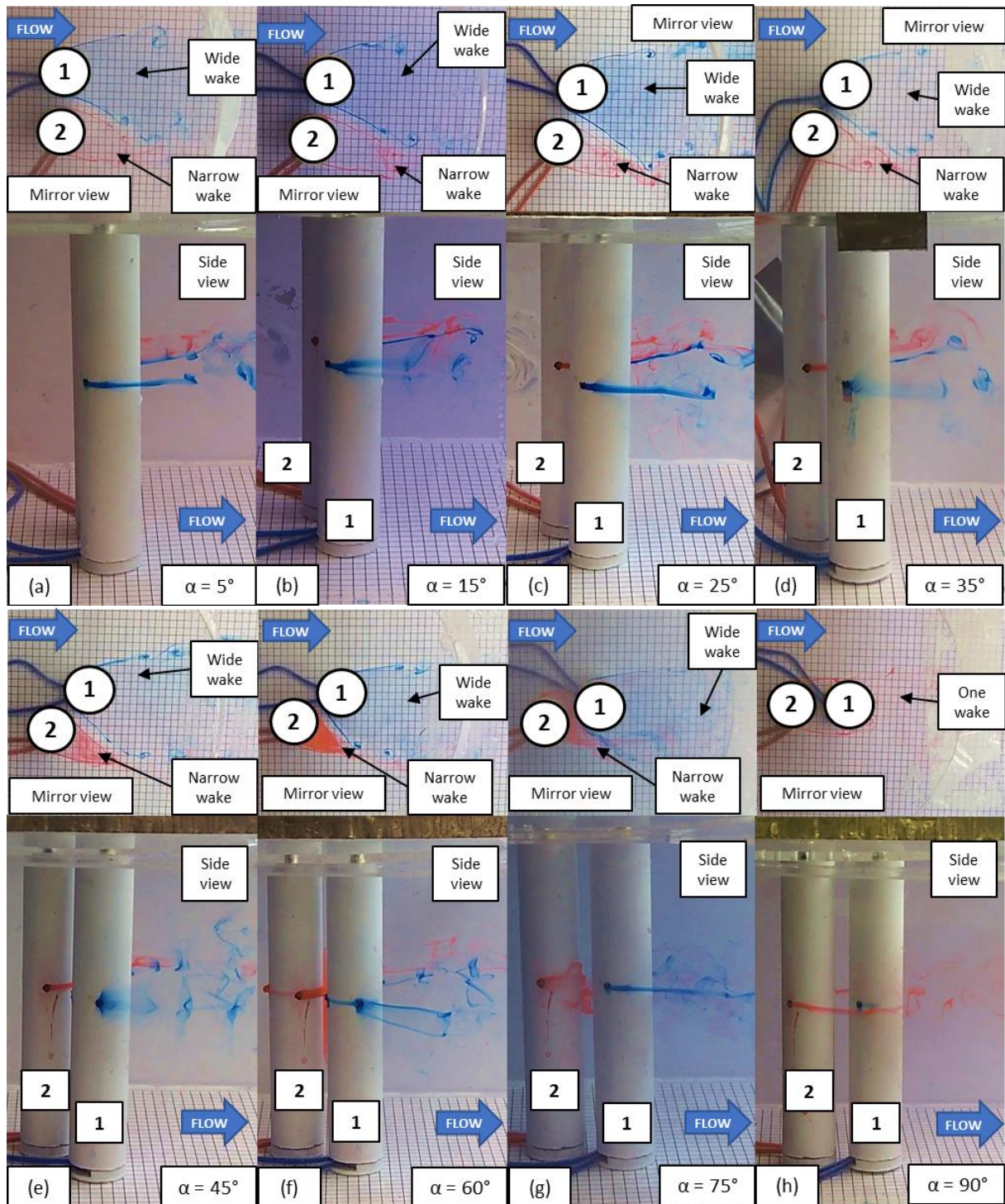


Figure 4.14 – Wake behavior behind cylinders for flow incidence angle of 5° (a), 15° (b), 25° (c), 35° (d), 45° (e), 60° (f), 75° (g) and 90° (h). Side and mirror views are shown for all the angles.

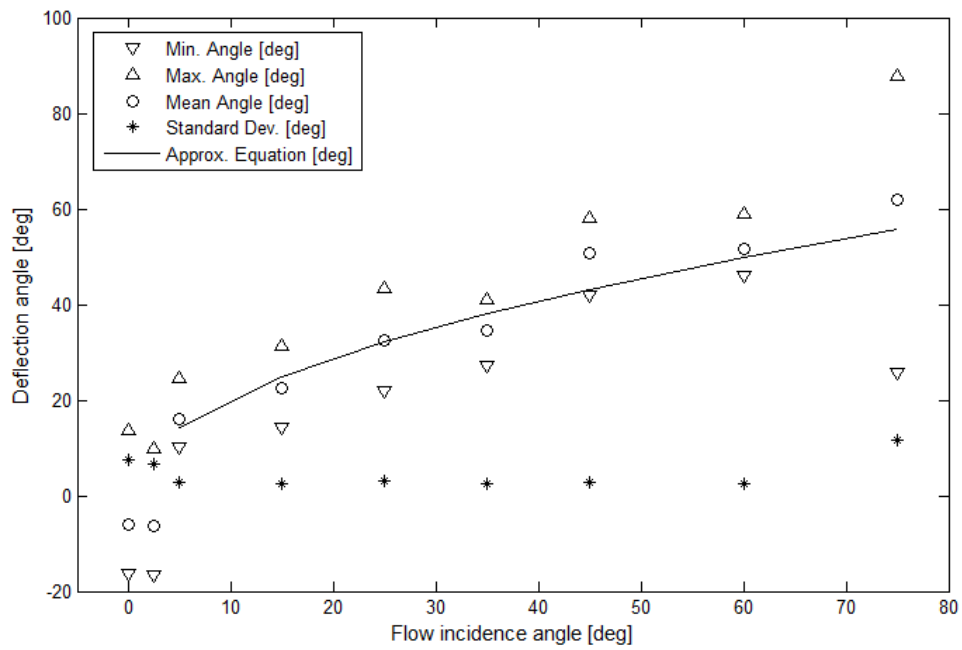


Figure 4.15 – Statistical data for analyzed angles in the hydrodynamic channel. The positive signal means that the deflection angle is in the same direction as the rotation angle.

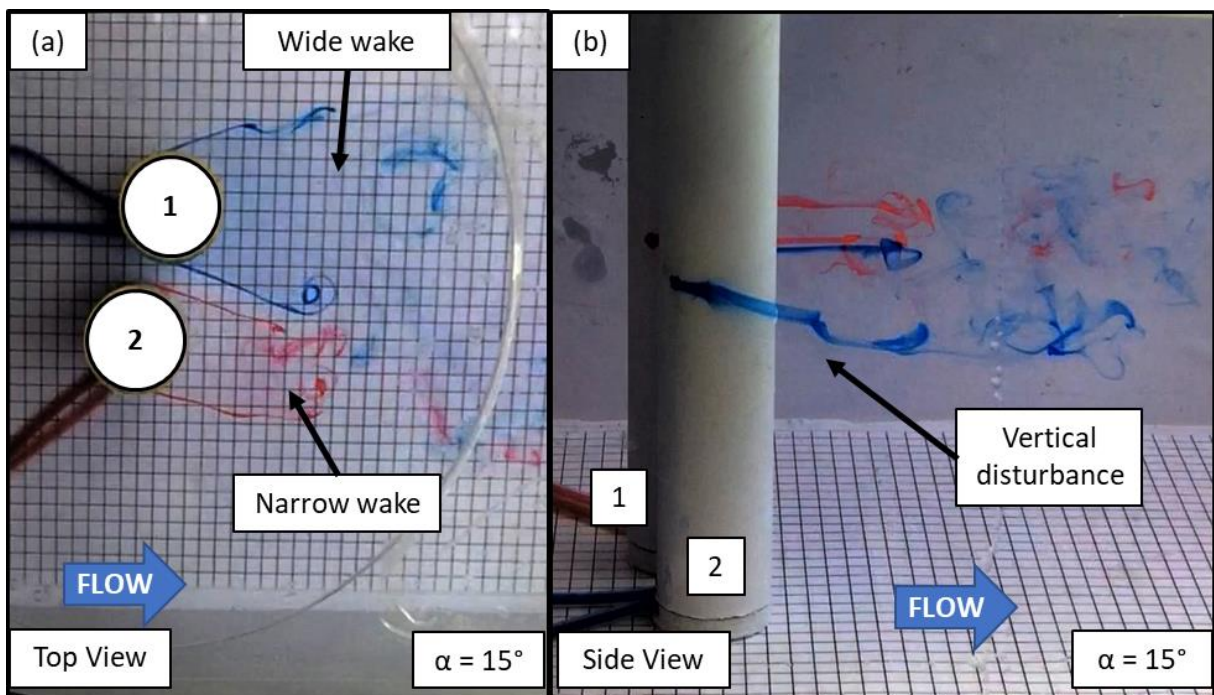


Figure 4.16 – Configuration with two different wakes: a narrow and a wide one (a, mirror view), and the side view of the cylinders (b) for the flow incidence angle equal to 15° .

In Figure 4.15, the continuous line represents a fit of the values of the mean deviation angle δ as a function of the incidence angle α , for values of α between 5° and 75° , given by Equation 4.1.

$$\delta = 6.44\alpha^{0.51} \quad (4.1)$$

The regression coefficient is 0.956. The tandem configuration (90°) is different from the other configuration investigated, once the cylinders are aligned with the flow and generate a well-behaved wake, not included in the graph.

4.3 Results for free to rotate cylinders

The velocity results obtained for the two cylinders with the freedom to rotate are presented in Figure 4.17, Figure 4.20, and Figure 4.21 for $Re = 9.00 \times 10^3$. The flow starts from rest, as in Varela et al., 2018, since it was started previously of the data acquisition. Figure 4.17 (a) and (b) shows the velocity signals with oscillations at the initial time and stabilization in one velocity level after the oscillation time.

From the time series of Figure 4.17, the flow is accelerated until 8.53 s, and a wake starts to be formed with higher values in the signal of Figure 4.17 (a) and lower values in Figure 4.17 (b), presenting the characteristics of one wide and one narrow wake between about 4 s up to 8 s: low-velocity values, wide wake; high-velocity values, narrow wake.

To observe the oscillation and rotation behavior, a high-speed camera was placed at one side wall and a mirror was positioned 45° with the camera, in order to track the angular position of the cylinders. The acquisition rate was 1000 frames per second, i.e., the time from the movies represents 0.001s for each second recorded, and the visualizations started with the assembly stopped and aligned in 0.00 rad. Figure 4.18 shows the angular position of the assembly to the flow along the time. When the results of the time series are increasing, it means that the assembly is rotating in counter-clockwise and the opposite occurs when the values of the time series are decreasing. The process of oscillation shown in Figure 4.18 is described in Table 4.6.

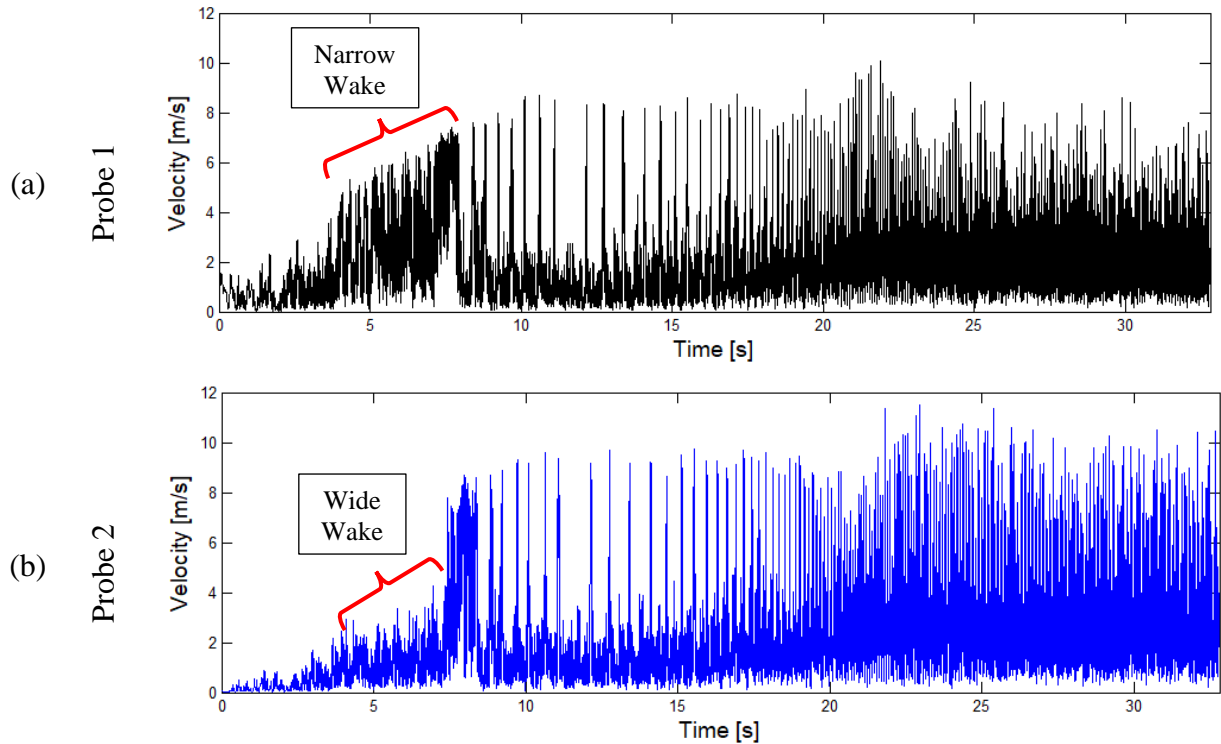


Figure 4.17 – Velocity signals for rotational cylinders for Probe 1 (a) and Probe 2 (b), free to rotate cylinders for $Re = 9.00 \times 10^3$.

After 8.53 s, an initial oscillation in the velocity is observed and is linked to the oscillation of the cylinders, observed in Figure 4.18. In this oscillation process, the assembly starts with oscillations, alternating clockwise and counter-clockwise, with an angular peak of 0.69 rad at 11.23 s (detail G in Figure 4.18). Then, the assembly turns $\pi/2$ clockwise, achieving another quasi-stable state. At 12.84 s (detail H in Figure 4.18), the assembly changes the rotation direction to counter-clockwise and starts the rotational regime, being accelerated until achieving about 580 rpm and remaining in this regime along the rest of the experiment. Some photographs are presented in Figure 4.19, which represents the view of the mirror, showing some moments described in Table 4.6, where (a) is the rest condition, (b) is one moment in which the setup change the oscillation direction, (c) shows another changing in the oscillation direction and (d) is when the configuration starts to rotate.

The signals from Figure 4.17 (a) and (b) were analyzed with discrete wavelet transform applying the Db20 wavelet; the results are presented in Figure 4.20 (a) and (b). The results show higher velocities between 5.6 s and 8.53 s (before the peaks in velocity) in the

first signal and lower for the second signal, as observed in Figure 4.17, indicating the two modes characteristics presented in Figure 2.3. After 8.53 s, where peaks in velocity are observed for both probes, the cylinders start the oscillation regime, described with details in Table 4.6 and Figure 4.18, presenting some oscillations in the velocity values as well. After 19 s the velocity values stabilizes when the assembly was already rotating, and the velocity remains constant during the rest of the experiment.

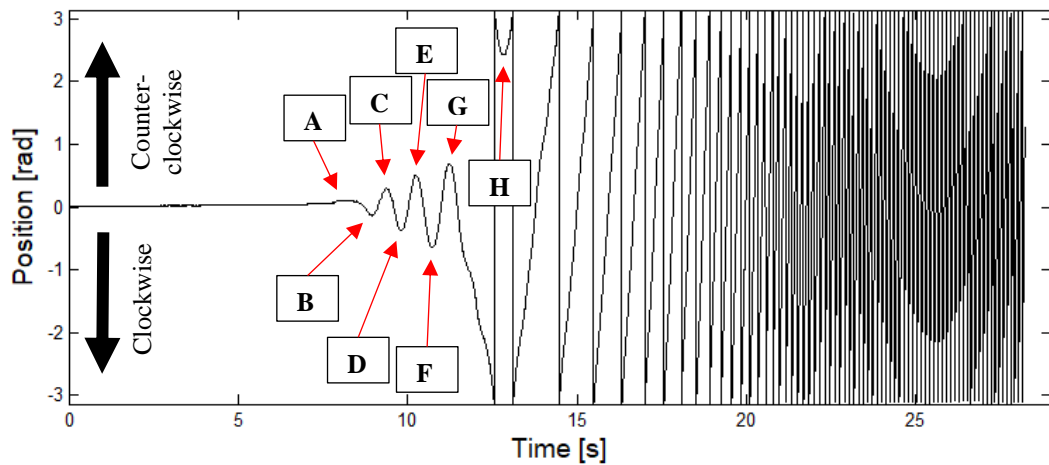


Figure 4.18 – Angular positions for Reynolds number of 9.00×10^3 .

Table 4.6 – Described oscillation process of the assembly for Reynolds number of 9.00×10^3 .

| Event | Time [s] | Oscillation event of the assembly |
|-------|----------|--|
| A | 8.53 | Started to rotate clockwise |
| B | 8.96 | Changed to counter-clockwise |
| C | 9.38 | Changed to clockwise |
| D | 9.78 | Changed to counter-clockwise |
| E | 10.29 | Changed to clockwise |
| F | 10.74 | Changed to counter-clockwise |
| G | 11.23 | Changed to clockwise |
| H | 12.84 | Turned $\pi/2$ and started the rotational regime |

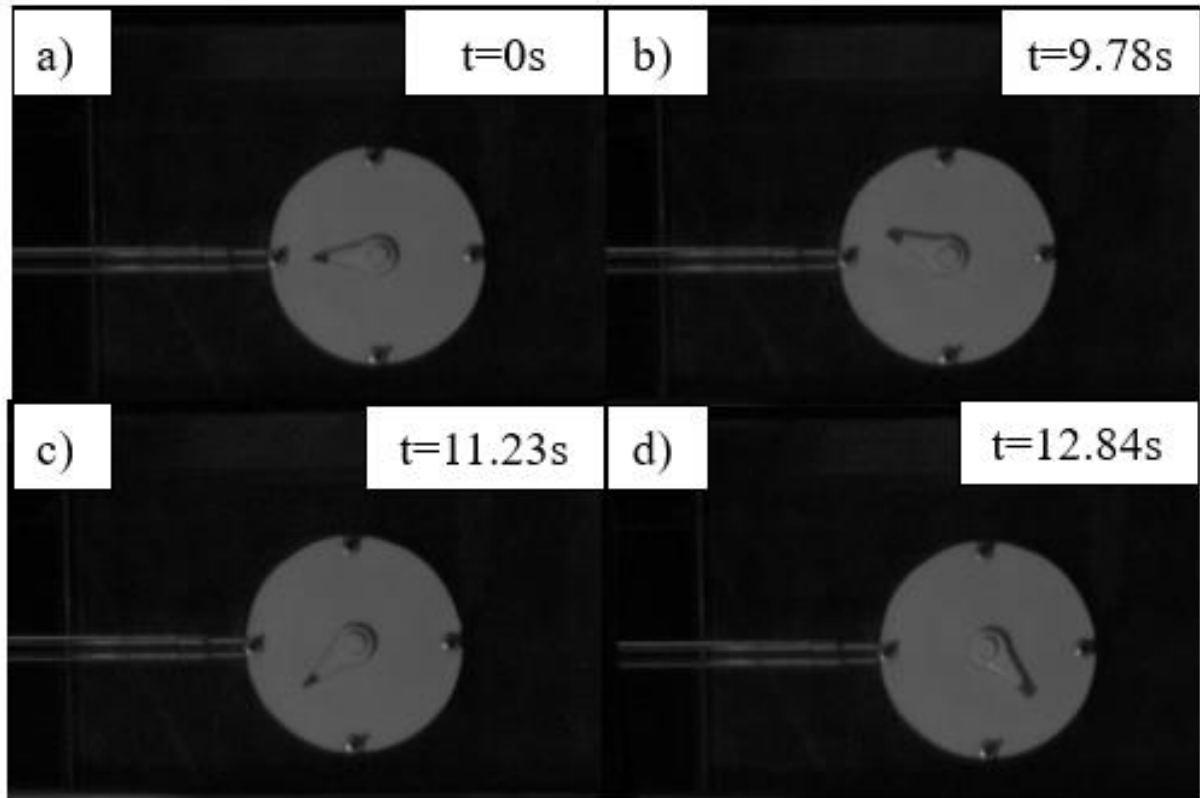


Figure 4.19 – Photographs of the oscillation process of the free to rotate cylinders, $Re = 9.00 \times 10^3$; rest position (a), change in the rotational direction (b and c), and starting the rotational regime (d).

Figure 4.21 (a) and (b) present the continuous wavelet analysis for the velocity signal (Figure 4.17) in the range between 1–250 Hz in step of 1 Hz and show the energy linked to the velocity series with the same main characteristics in both results. The energy stabilizes in higher levels after the oscillations ($t = 19$ s), about 20Hz.

Figure 4.22 presents the power spectrum from the velocity signals presented in Figure 4.17 and the results from both signals presents peaks in 18.55 Hz and harmonics in 54.69 Hz, 72.34 Hz, and 127.9 Hz. The Strouhal numbers, considering the cylinder diameter and the gap flow (7.29 m/s) are 0.06, 0.18, 0.25, and 0.43, respectively. Results are similar to those found by Varela, 2017, where the author also found several harmonics but did not evaluate the Strouhal numbers. Strouhal numbers computed for the reference velocity (5.4 m/s) and the diameter of the cylinders are 0.09, 0.25, 0.34, and 0.59, respectively.

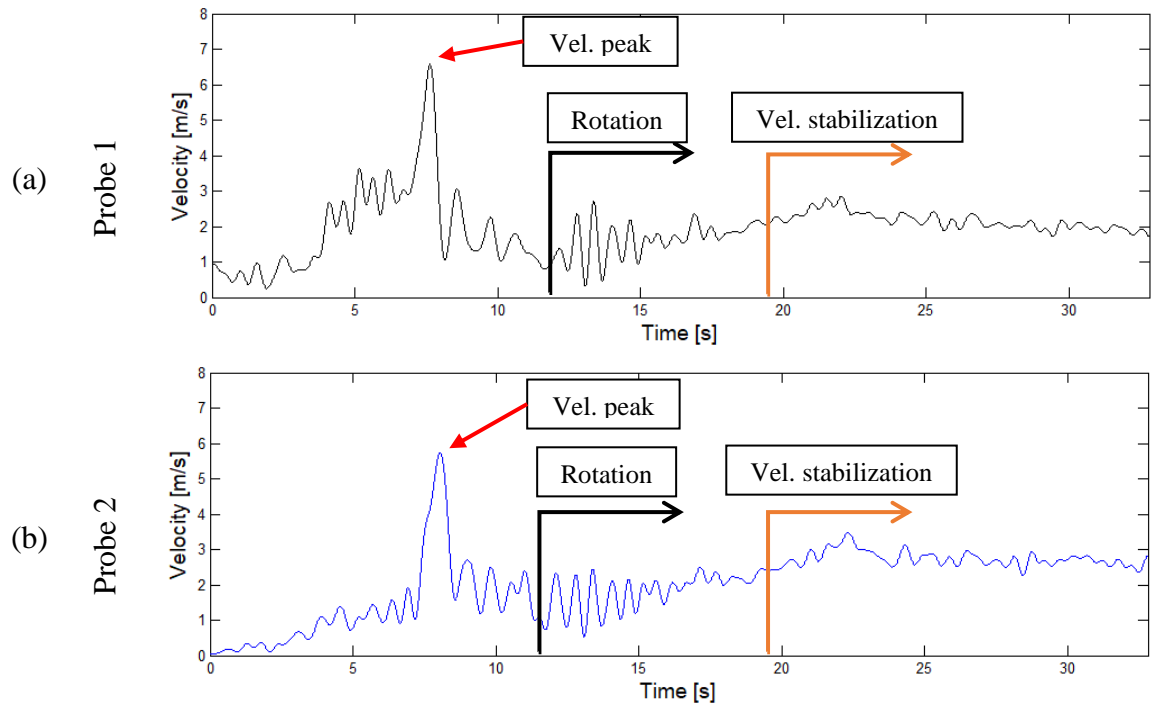


Figure 4.20 – Reconstructed signals of velocities using DWT for Probe 1 (a) and Probe 2 (b), free to rotate cylinders for $Re = 9.00 \times 10^3$.

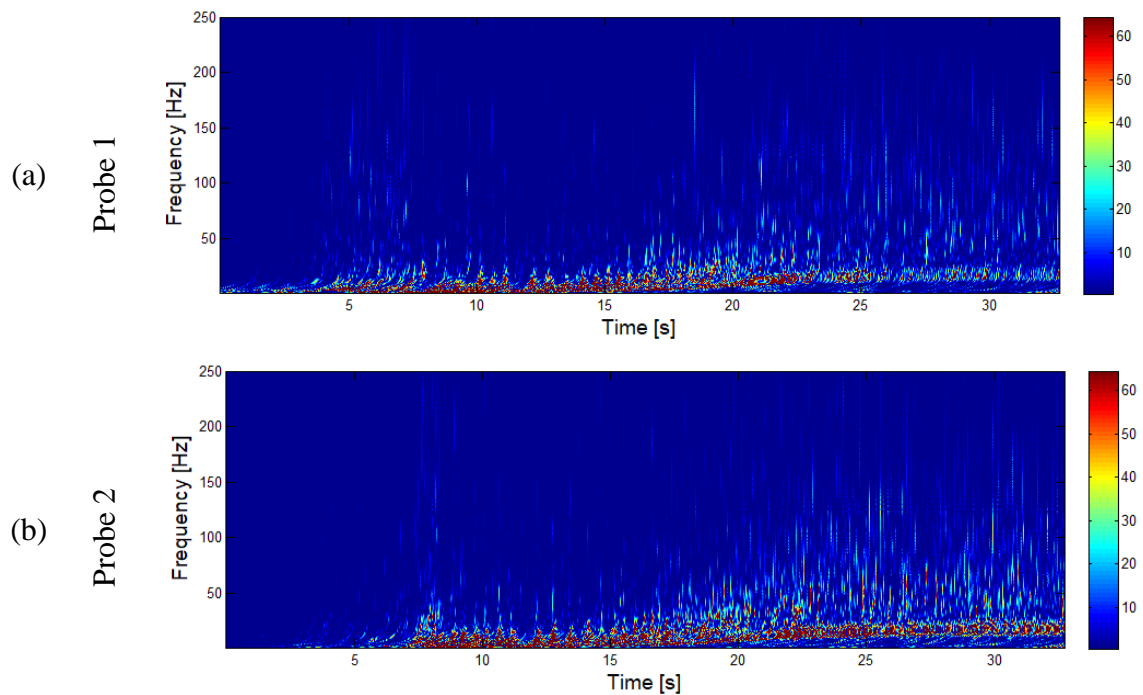
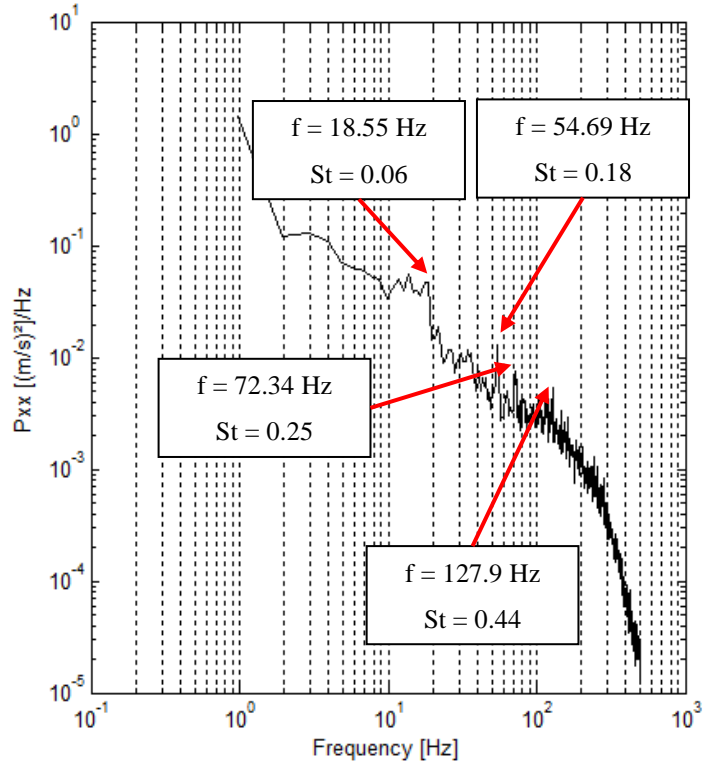
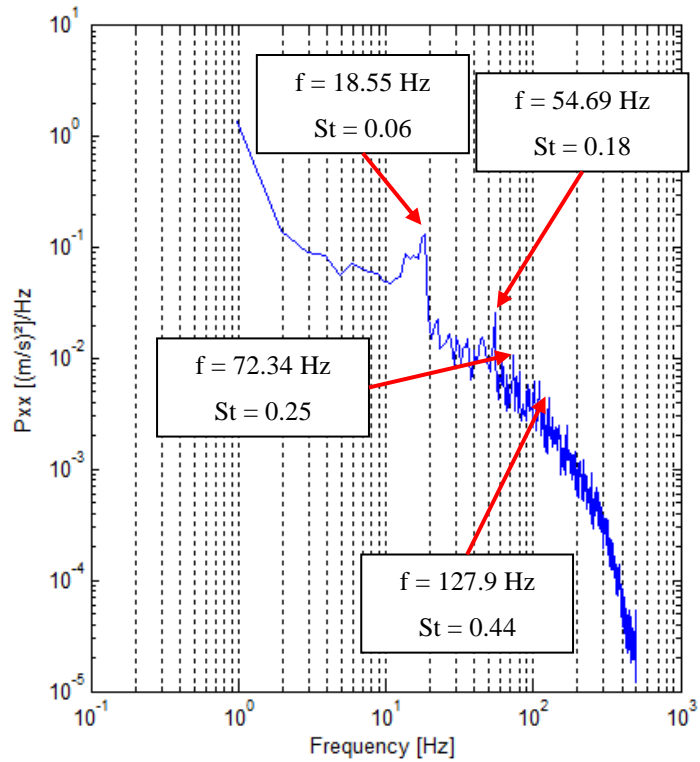


Figure 4.21 – CWT for the velocity signals for Probe 1 (a) and Probe 2 (b), free to rotate cylinders for $Re = 9.00 \times 10^3$.



(a) - Probe 1



(b) - Probe 2

Figure 4.22 – Power spectrum from velocity signals (Figure 4.17) for Probe 1 (a) and Probe 2 (b), free to rotate cylinders for $Re = 9.00 \times 10^3$.

For Reynolds number 1.66×10^4 the same analysis applied for Reynolds number 9.00×10^3 was performed. Figure 4.23 shows the results for the flow velocity. From the time series of Figure 4.23 (a) and (b), the flow is accelerated until 9.38s, and a wake starts to be formed with higher values in the signal of Figure 4.23 (a) and lower values in Figure 4.23 (b), presenting the characteristics of one wide and one narrow wake, as occurred for $Re=9.00 \times 10^3$.

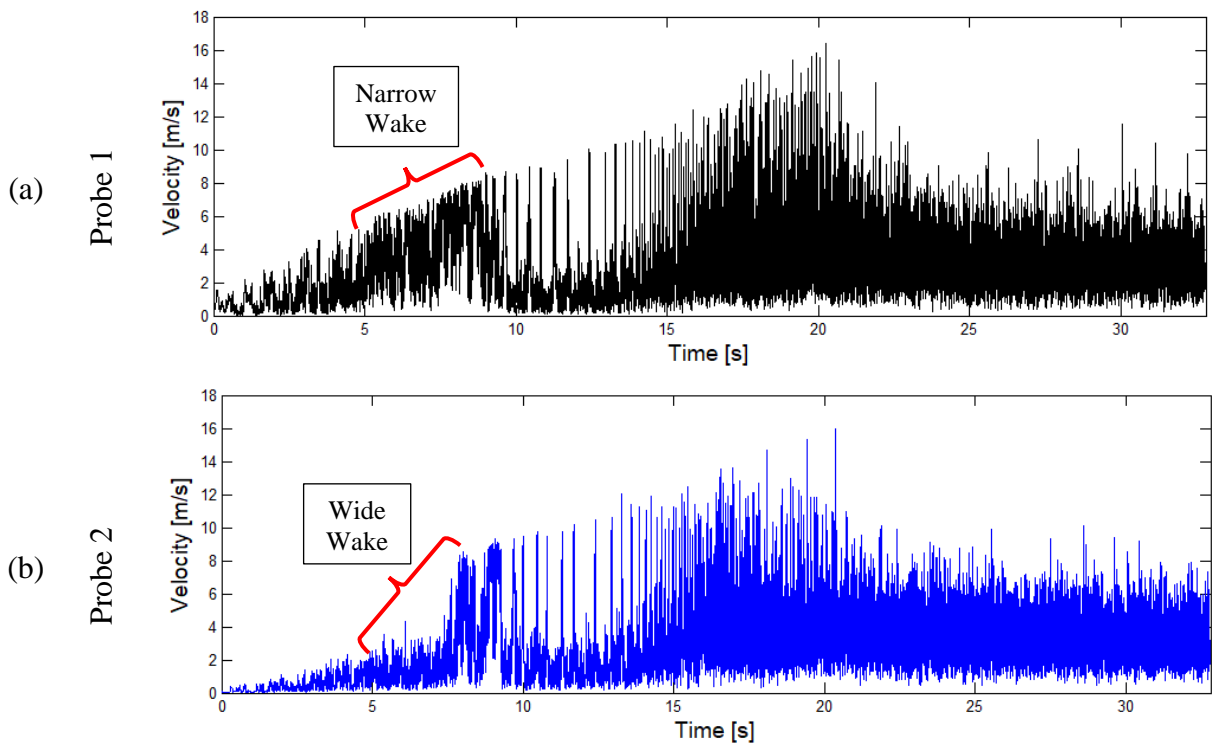


Figure 4.23 – Velocity signals for rotational cylinders for Probe 1 (a) and Probe 2 (b), free to rotate cylinders for $Re = 1.66 \times 10^4$.

Figure 4.24 shows the angular position of the assembly to the flow along the time for $Re=1.66 \times 10^4$. The assembly starts stopped and aligned with 0.00 rad. The process of oscillation shown in Figure 4.24 is described in Table 4.7. After 9.78 s, an initial oscillation in the velocity is observed and is linked to the oscillation of the assembly that can be observed in Figure 4.24. In this oscillation process, the assembly starts with oscillations for both clockwise and counter-clockwise, achieving a peak position of 0.77 rad at 11.88 s (detail F in Figure 4.24). Then, the assembly turns clockwise, starting the rotational regime. The assembly

is accelerated until achieves about 1250 rpm and remains in this regime and rotational velocity along the rest of the experiment.

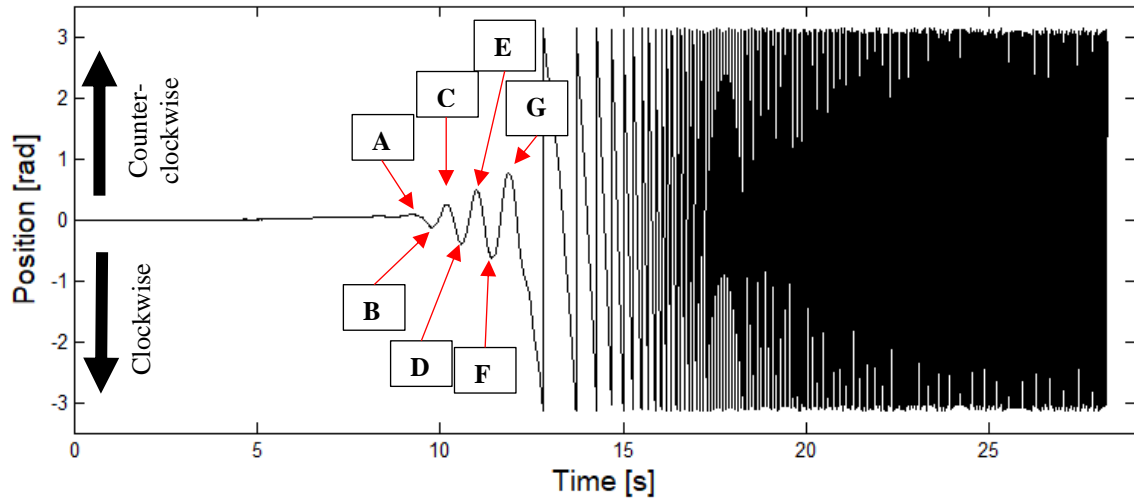


Figure 4.24 – Angular positions for Reynolds number of 1.66×10^4 .

Table 4.7 – Described oscillation process of the assembly for Reynolds number of 1.66×10^4 .

| Event | Time [s] | Oscillation event of the assembly |
|-------|----------|-----------------------------------|
| A | 9.38 | Started to rotate clockwise |
| B | 9.74 | Changed to counter-clockwise |
| C | 10.23 | Changed to clockwise |
| D | 10.60 | Changed to counter-clockwise |
| E | 11.01 | Changed to clockwise |
| F | 11.44 | Changed to counter-clockwise |
| G | 11.88 | Started the rotational regime |

Figure 4.25 presents some photographs from the recordings performed by the high-speed camera for Reynolds number 1.66×10^4 , detailing the mirror and side views for two instants: changing in the rotational direction (a) and the configuration with the rotational regime already achieved (b).

The signals from Figure 4.23 (a) and (b) were filtered with discrete wavelet transform applying the Db20 wavelet and the results are presented in Figure 4.26 (a) and (b). The results showed higher velocities between 5 s and 9.38 s in the first signal and lower for the second signal, indicating the two characteristics modes, also found in Figure 4.23. After 9.38 s, oscillation in velocity values is perceived and after 20 s the velocity values stabilizes when the assembly is already rotating. Figure 4.28 (a) and (b) presents the continuous wavelet transform in the range between 1–250 Hz in step of 1 Hz and shows the energy linked to the velocity series with the same main characteristics in both results. The energy stabilizes in higher levels after the oscillations, about 40 Hz.

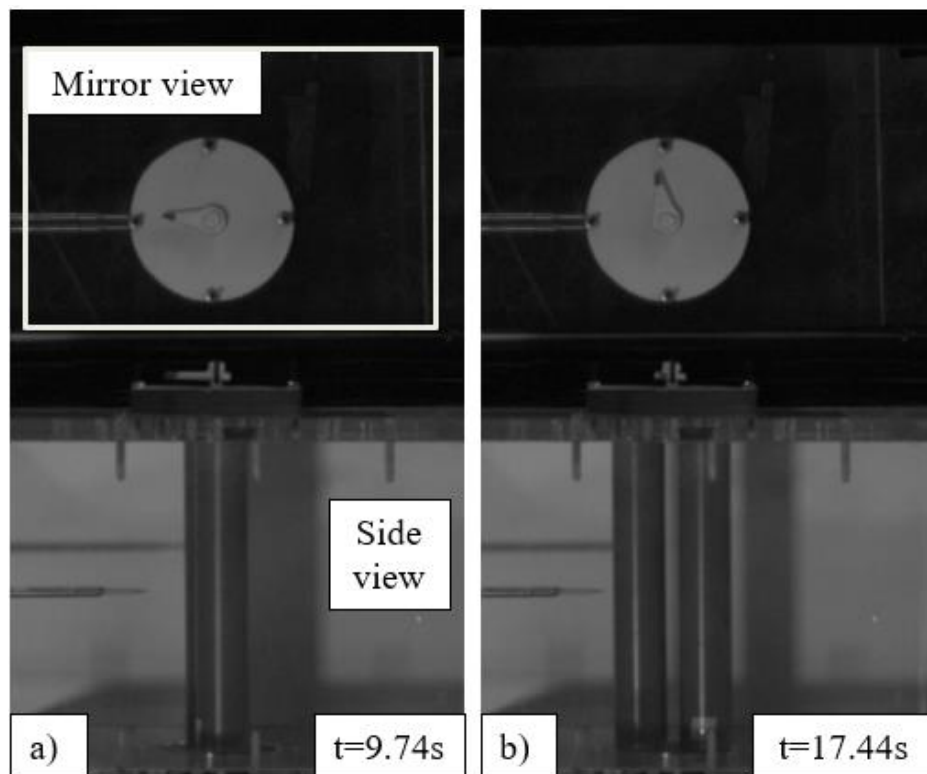


Figure 4.25 – Photographs of the oscillation/rotational process of the free to rotate cylinders, $Re = 1.66 \times 10^4$; instant in which the configuration is changing the rotational direction, with details about the side and mirror view (a) and instant in which the configuration is already rotating (b).

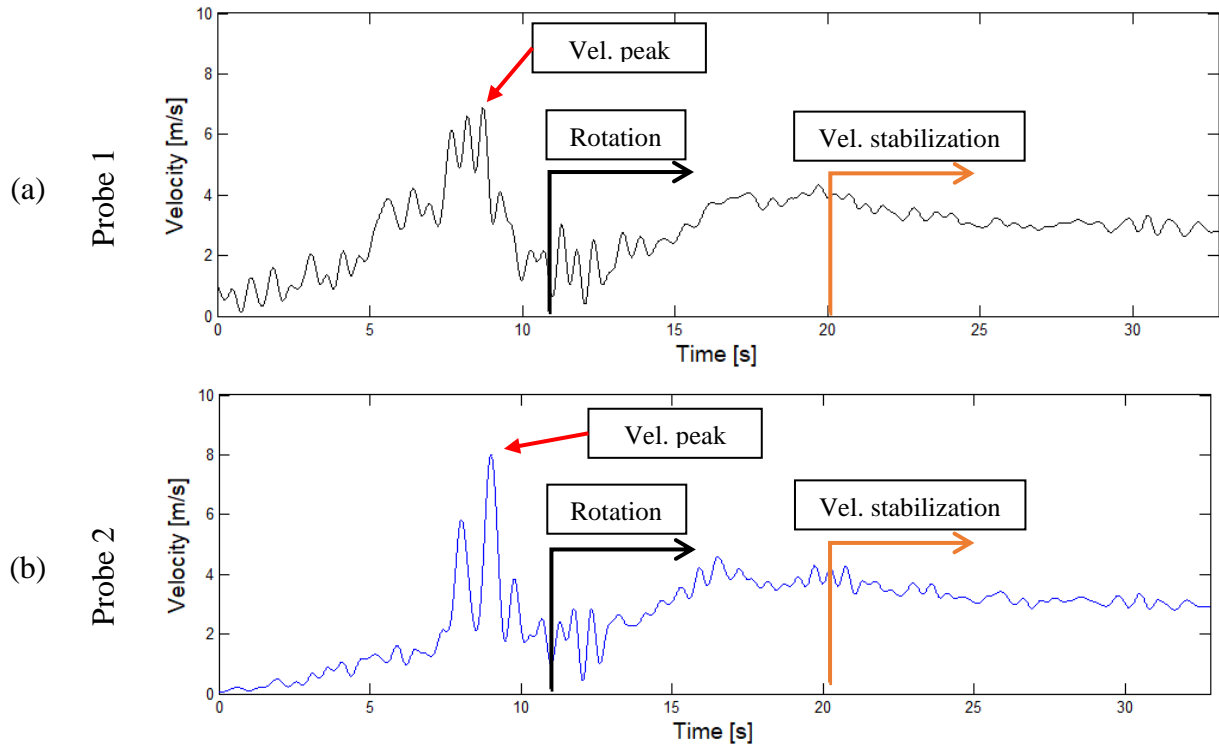
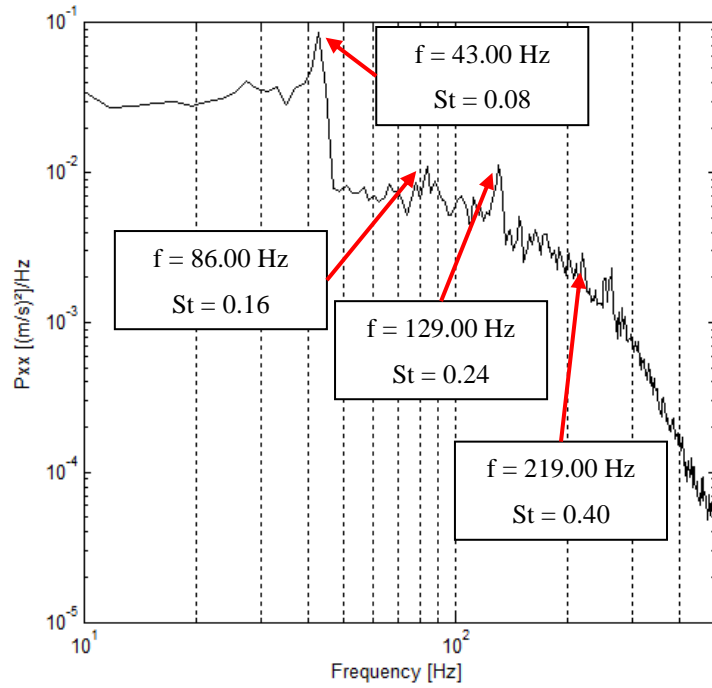


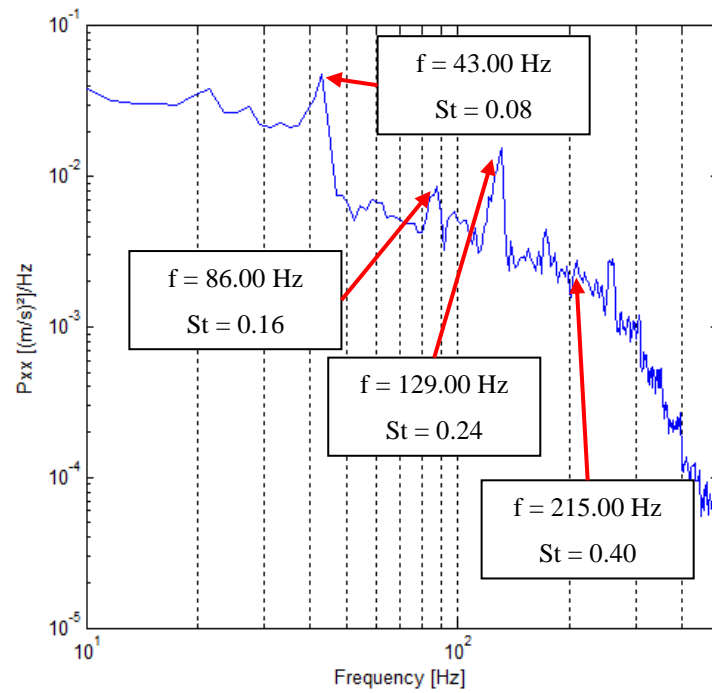
Figure 4.26 – Reconstructed signals of velocities using DWT for Probe 1 (a) and Probe 2 (b), free to rotate cylinders for $Re = 1.66 \times 10^4$.

Figure 4.27 presents the power spectrum from the velocity signals presented in Figure 4.23 and the results from both signals present peaks in 43 Hz and harmonics in 86 Hz, 129 Hz, and 219 Hz. The Strouhal numbers, considering the cylinder's diameter and the gap flow (13.50 m/s), are 0.08, 0.16, 0.24, and 0.4, respectively. Strouhal numbers computed for the reference velocity (10 m/s) and the cylinders diameter are 0.11, 0.22, 0.32 and 0.55, respectively. These results are in agreement with Varela, 2017.

How the oscillation starts and how it behaves along with time present variation in each test, without maintaining a sequential pattern. This destabilization/oscillation is a result of a chaotic process, as shown in De Paula and Möller, 2018, and of the alternation of the drag forces on each cylinder demonstrated by Varela et al., 2018. It is suggested that it also can be influenced by other factors such as transversal misalignment of the tubes in the rest condition before flow starts, geometrical imperfections, and the blockage ratio oscillation. In any case, bistability also has no pattern of flow deviation [De Paula and Möller, 2018], which must be taken into account in the analysis of the direction of rotation.



(a) - Probe 1



(b) - Probe 2

Figure 4.27 – Power spectrum from velocity signals (Figure 4.23) for Probe 1 (a) and Probe 2 (b), free to rotate cylinders for $Re = 1.66 \times 10^4$.

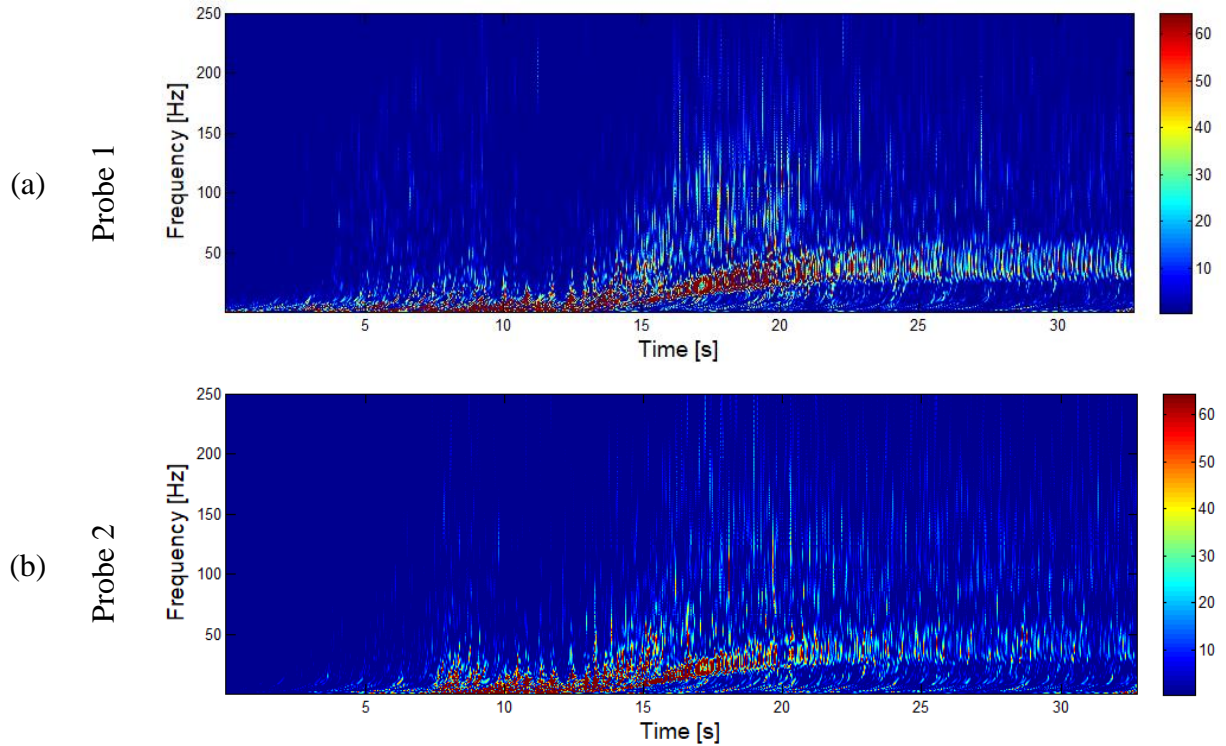


Figure 4.28 – CWT for the velocity signals for Probe 1 (a) and Probe 2 (b), free to rotate cylinders for $Re = 1.66 \times 10^4$.

4.3.1 Results for power generation for free to rotate cylinders

For free to rotate cylinders, the electrical generation experiment happened as described in section 3.2.5. The experiment consisted in coupling the generator in the assembly with the cylinders, turning on the blower with the generator off, and when the rotational velocity was stabilized, turning the generator on.

The velocities used to present the results for the aerodynamic channel (section 4.3), 5.4 m/s and 10 m/s, were not sufficient to rotate the generator, even with the help of aerodynamic devices to accelerate the flow close to the cylinders. Therefore, higher flow velocities were imposed in the flow, in order to generate electrical power. The velocity of 12.6 m/s was selected to present the results and compare them with the wind turbine.

Even with the free stream velocity of 12.6 m/s, the “throat device” was placed to improve the rotational velocity of the rotational cylinders (similar to presented in Figure 3.8b). The results for 12.6 m/s are presented in Table 4.8 and Figure 4.29.

Table 4.8 – Power generation results for free to rotate cylinders with the “throat device”, the reference flow velocity of 12.6 m/s

| N° de LEDs [un.] | rpm | U [V] | i [mA] | P [mW] |
|------------------|------|-------|--------|--------|
| 0 | 2330 | – | – | – |
| 1 | 2140 | 1.10 | 50.20 | 55.22 |
| 2 | 2140 | 1.11 | 51.32 | 56.97 |
| 3 | 2140 | 1.13 | 51.11 | 57.75 |
| 4 | 2140 | 1.16 | 52.96 | 61.43 |
| 5 | 2100 | 1.18 | 53.52 | 63.15 |
| 6 | 2100 | 1.20 | 54.32 | 65.18 |
| 7 | 2100 | 1.20 | 54.80 | 65.76 |
| 8 | 2060 | 1.22 | 55.40 | 67.59 |
| 9 | 2060 | 1.23 | 54.75 | 67.34 |

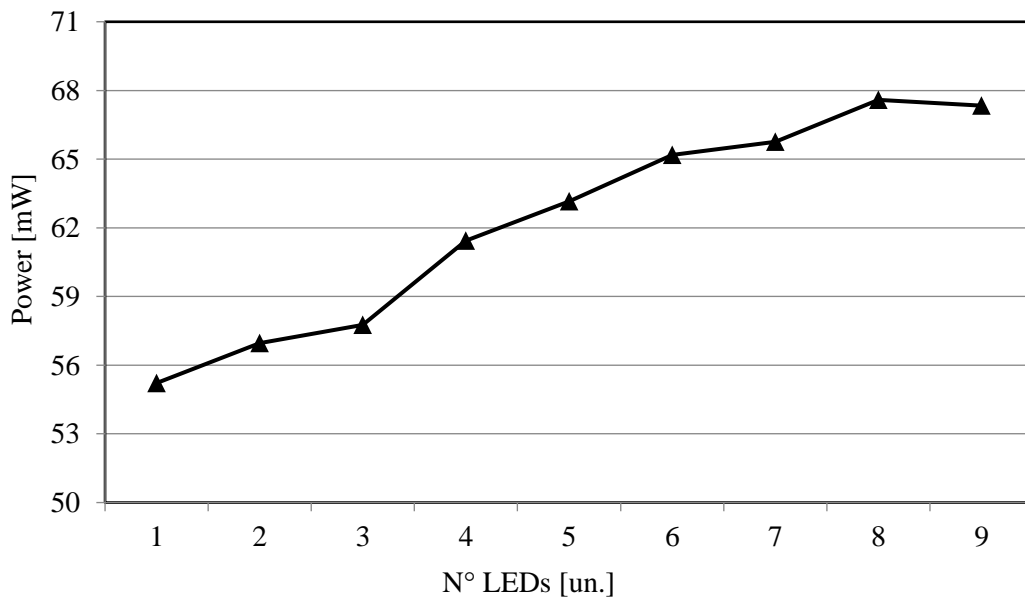


Figure 4.29 – Power generation for reference flow velocity of 12.6 m/s and assist of the “throat device”.

Table 4.8 shows the results for the number of LEDs used, rotational velocity, electrical voltage, electrical current, and power for each number of LEDs tested. Each LED has one defined resistance (about 150 Ω) and they are linked with each other parallelly, decreasing the

equivalent resistance of the system, allowing more power generation in the electrical system up to the limit of the power extracted from the flow by the tested device. The rotational velocity with the generator off is about 10% higher compared with the generator turned on. The power is almost constant after adding 8 LEDs in the system, about 67.59 mW.

Even with the velocity of 12.6 m/s imposed in the free stream flow and the generator off, the assembly with two cylinders free to rotate needed assistance to start and stabilized the rotational velocity. Once the velocity was stabilized, the generator was turned on. Section 4.5.1 will compare these results with the wind turbine results.

Another attempt to generate power consisted in using a cylinder instead of the “throat device”. This cylinder was placed on the side of the setup, fixed with a distance to obtain the p/d ratio equal to 1.26 with the other cylinders. The objective is to analyze if a great increase in the blockage ratio is really necessary to generate power or just a punctual acceleration near the cylinders is sufficient for that.

The experiment started with the generator off and a free stream velocity of 12.6 m/s. When the rotational velocity is stabilized, the generator was turned on and the values of rotational velocity, electrical current, and tension were evaluated, as shown in Table 4.9 and Figure 4.30.

Table 4.9 – Power generation results for free to rotate cylinders with the extra cylinder, the reference flow velocity of 12.6 m/s.

| N° de LEDs [un.] | rpm | U [V] | i [mA] | P [mW] |
|------------------|------|-------|--------|--------|
| 0 | 1000 | – | – | – |
| 1 | 805 | 0.38 | 17.77 | 6.75 |
| 2 | 805 | 0.42 | 18.31 | 7.69 |
| 3 | 805 | 0.43 | 18.95 | 8.15 |
| 4 | 805 | 0.44 | 19.32 | 8.50 |
| 5 | 790 | 0.44 | 19.45 | 8.56 |
| 6 | 790 | 0.45 | 19.26 | 8.67 |
| 7 | 790 | 0.44 | 20.43 | 8.99 |
| 8 | 790 | 0.46 | 20.02 | 9.21 |
| 9 | 790 | 0.45 | 20.73 | 9.33 |
| 10 | 760 | 0.46 | 21.89 | 10.07 |

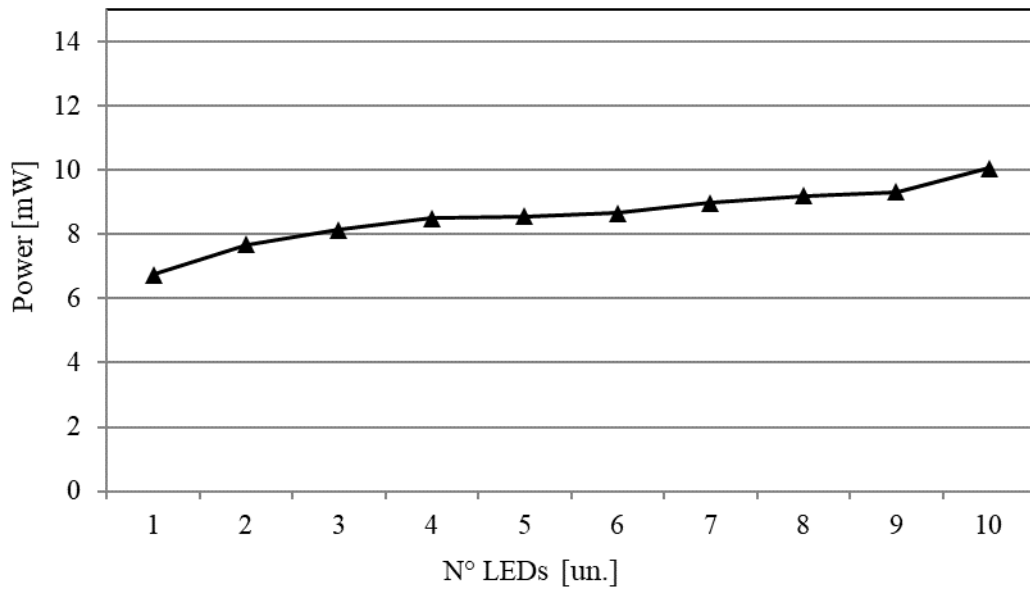


Figure 4.30 – Power generation for reference flow velocity of 12.6 m/s with the extra cylinder.

From Table 4.9 and Figure 4.30, the electrical power produced is 6.7 times less than the experiment with the “throat device”. The levels of rotational velocity are lesser as well. These results show that the blockage ratio influences much more in the power generation than only adding one more cylinder. Although the lower levels of power generation, this experiment showed that the power can be generated without the “throat device”, which besides accelerating the flow, increases the blockage ratio to 51.3%, while the additional cylinders remain the blockage ratio at 38.8%.

4.4 Results for the free to oscillate cylinders

For the experiments regarding the free to oscillate cylinders, the figures with the results will present the velocity values only for one probe, once the experiment was performed with only one probe. The sections with the results are organized according to the technique used to evaluate the behavior of the assembly, and in each one is presented the results for 5 m/s, 7.5 m/s, and 10 m/s. The power generation analysis was not applied to this configuration of cylinders. The main objective of the following experiments is to analyze the behavior of the cylinders in a configuration with a central cylinder, similar to tandem positioning.

4.4.1 Natural

The velocity results for the assembly without the assistance of aerodynamic devices are presented in Figure 4.31, including the results for 5 m/s (a), 7.5 m/s (b), and 10 m/s (c). The results showed low levels of velocity, being better visualized with the reconstructed signals by means of DWT in Figure 4.32. Several oscillations are perceived in Figure 4.32 (b) and (c), but the angular oscillation of the assembly is about 0.1 rad for reference velocity 10 m/s (Figure 4.34c), and for the other velocities the system is in rest position (Figure 4.34b and c). As the probe is downstream and close to the cylinder, low velocities were expected.

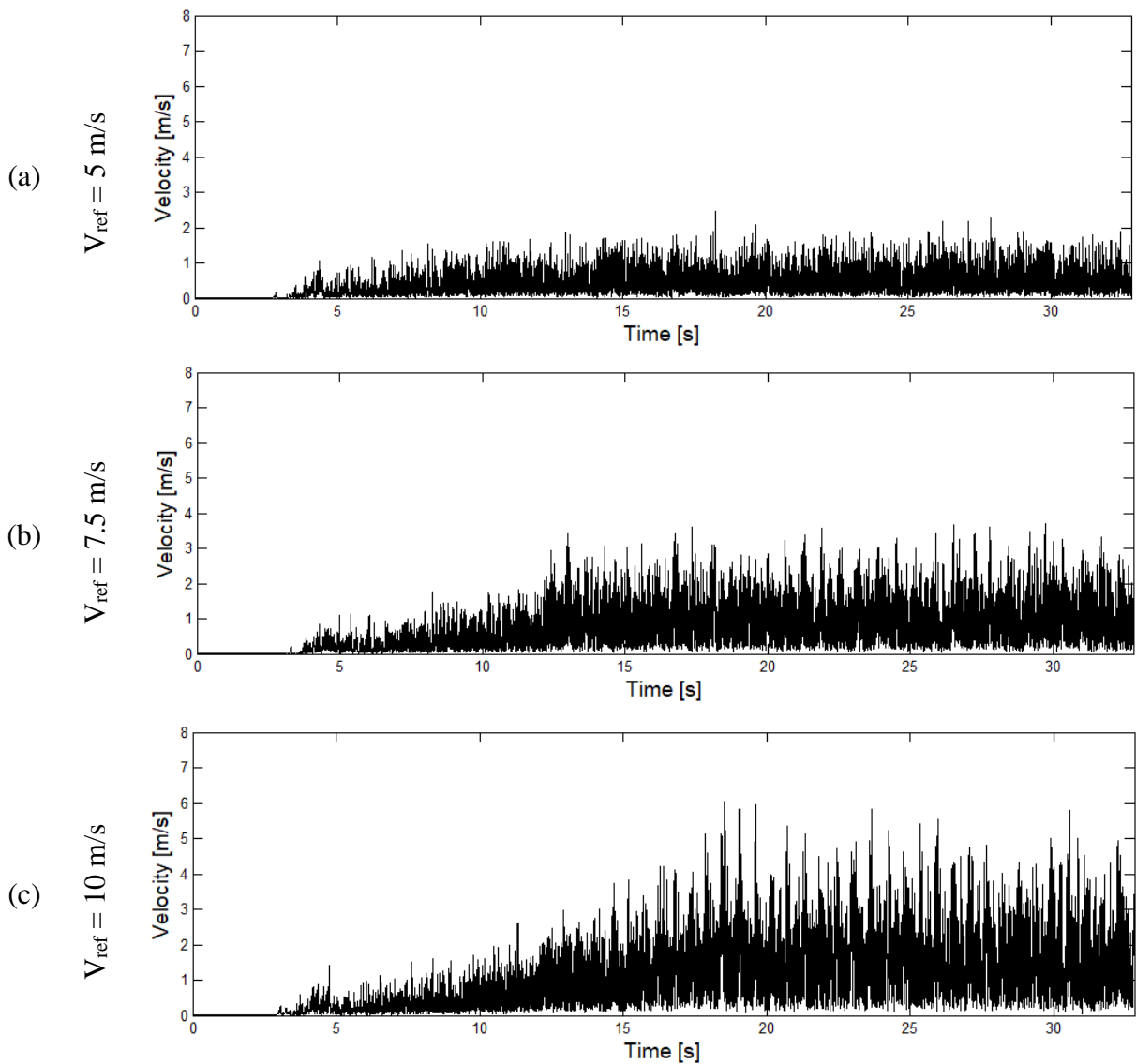


Figure 4.31 – Velocity signals reference velocity 5 m/s (a), 7.5 m/s (b) and 10 m/s (c), respectively; free to oscillate cylinders, natural setup.

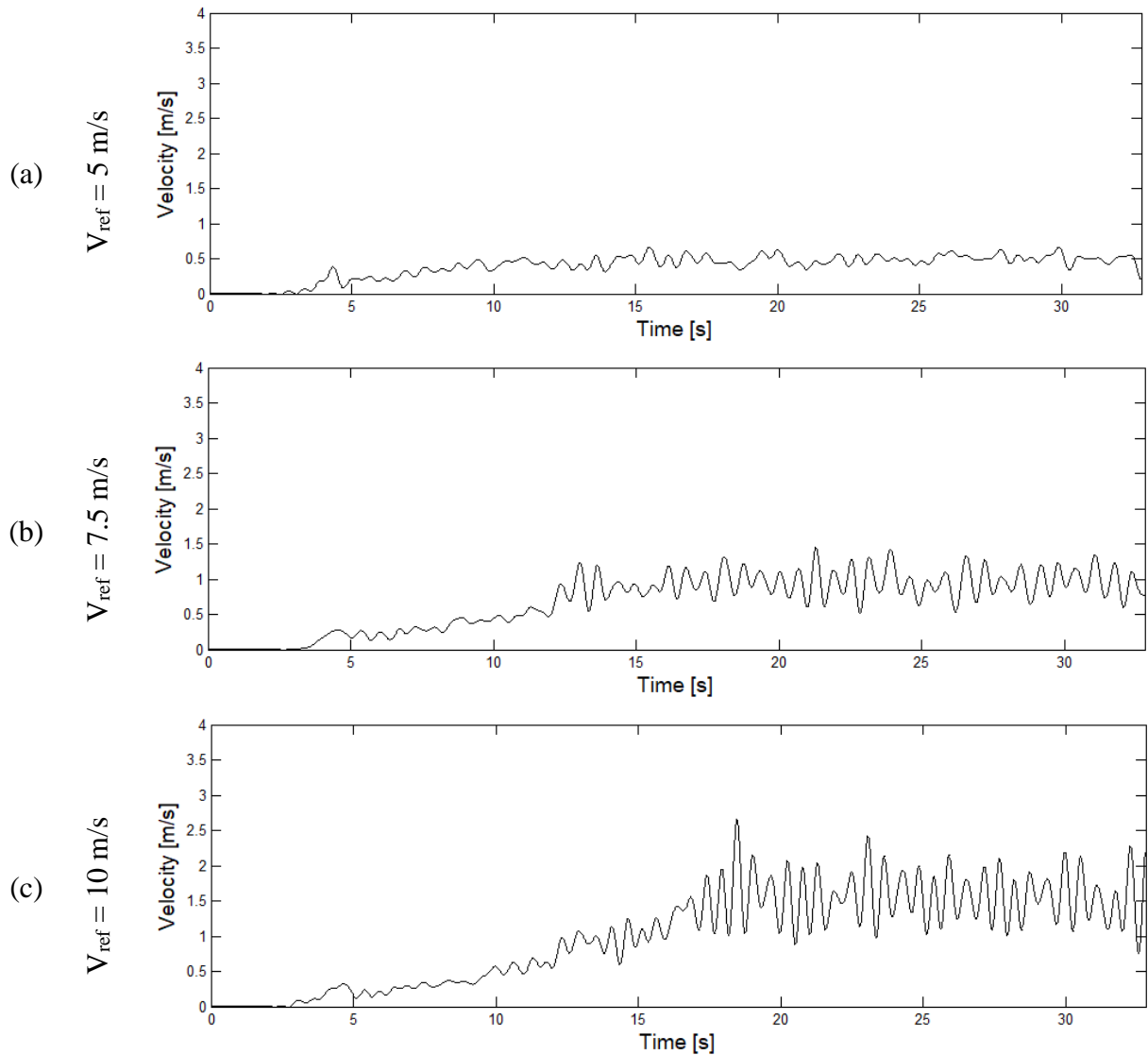


Figure 4.32 – Reconstruction of the signals using DWT for reference velocity 5 m/s (a), 7.5 m/s (b) and 10 m/s (c), respectively; free to oscillate cylinders, natural setup.

Figure 4.33 (a), (b), and (c) presents the continuous wavelet transform results for the velocity signals of Figure 4.31, in the range between 1–150 Hz and bandwidth of 1 Hz. Once the values of velocity signals in Figure 4.31 are low and velocity fluctuations are observed only in the case of Figure 4.32 (b) and (c), corresponding to velocities 7.5 m/s and 10 m/s, respectively, the energy of the flow is low in this case, with some small peaks of energy in Figure 4.33 (c) due to the velocity fluctuations.

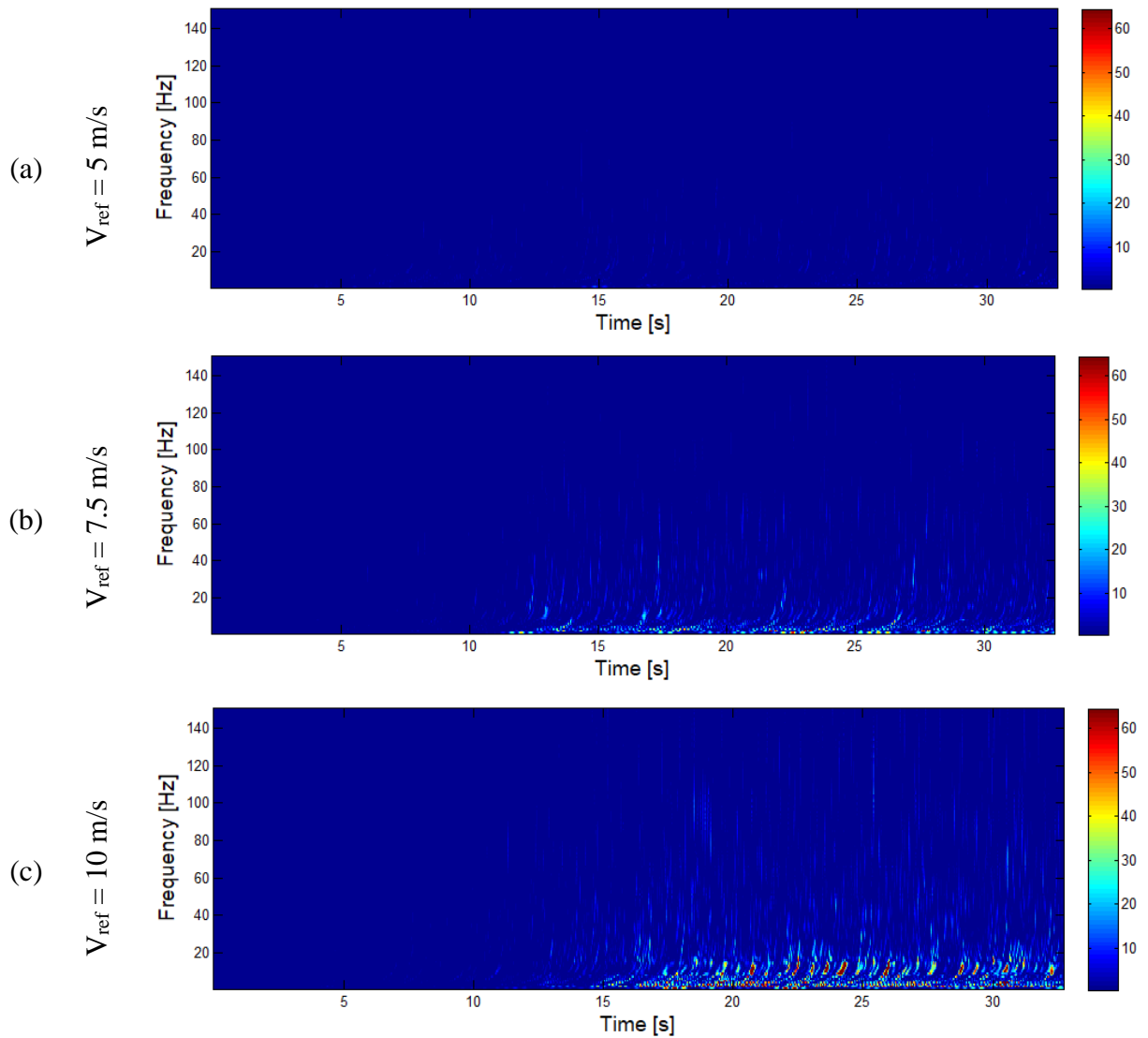


Figure 4.33 – CWT from the velocity signals for reference velocity 5 m/s (a), 7.5 m/s (b) and 10 m/s (c), respectively; free to oscillate cylinders, natural setup.

The behavior of this configuration for reference velocity 10 m/s is presented in Figure 4.35, supporting the results shown in Figure 4.34. Figure 4.35 (a) shows the moment in which the acquisition system of the velocity signal is turned on, and (b) represents the angular peak obtained for this configuration. With this configuration, without aerodynamical devices, the system is practically in rest position for all the reference flow velocities.

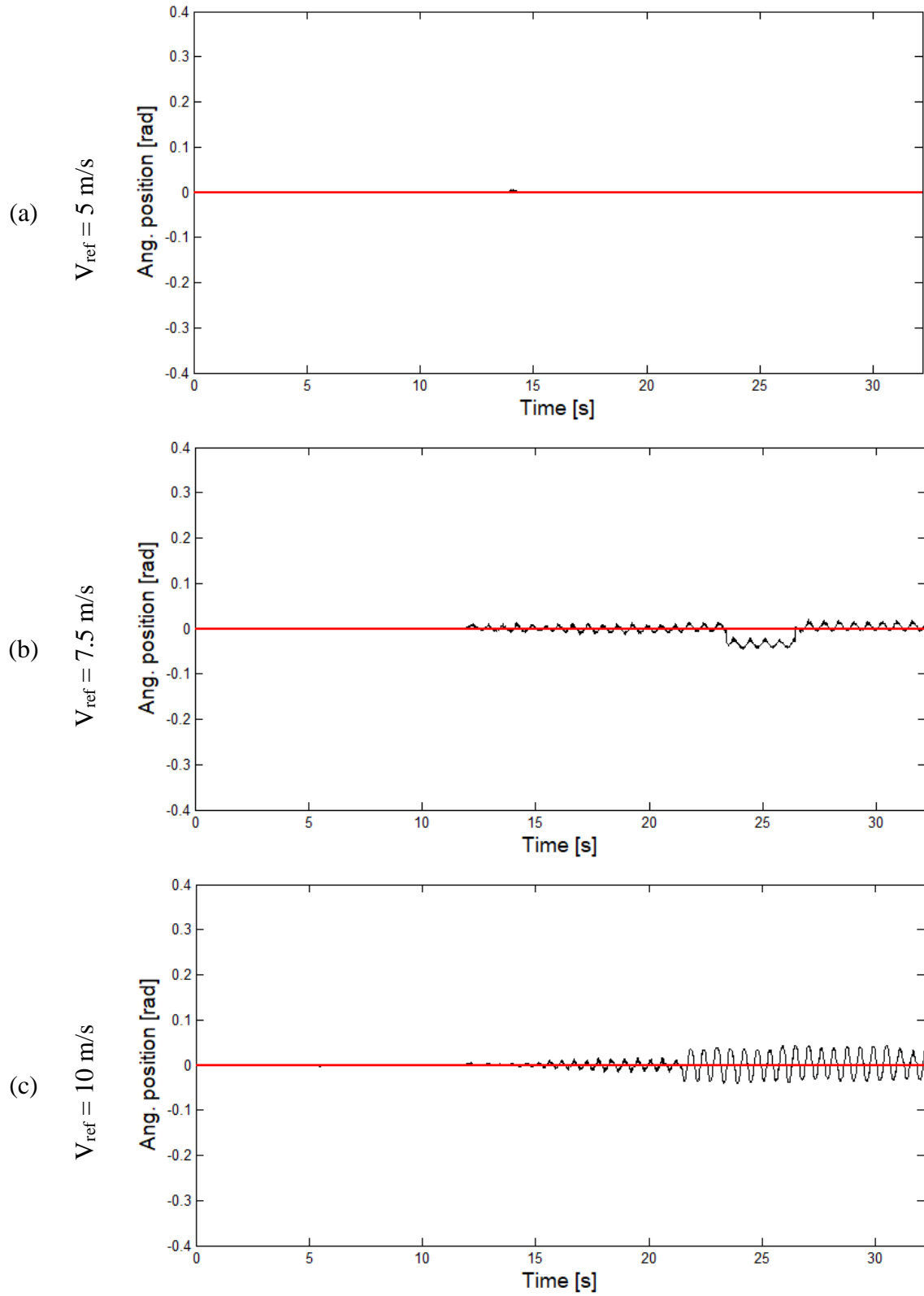


Figure 4.34 – Angular behavior for the natural free to oscillate cylinders for 5 m/s (a), 7.5 m/s (b) and 10 m/s (c).

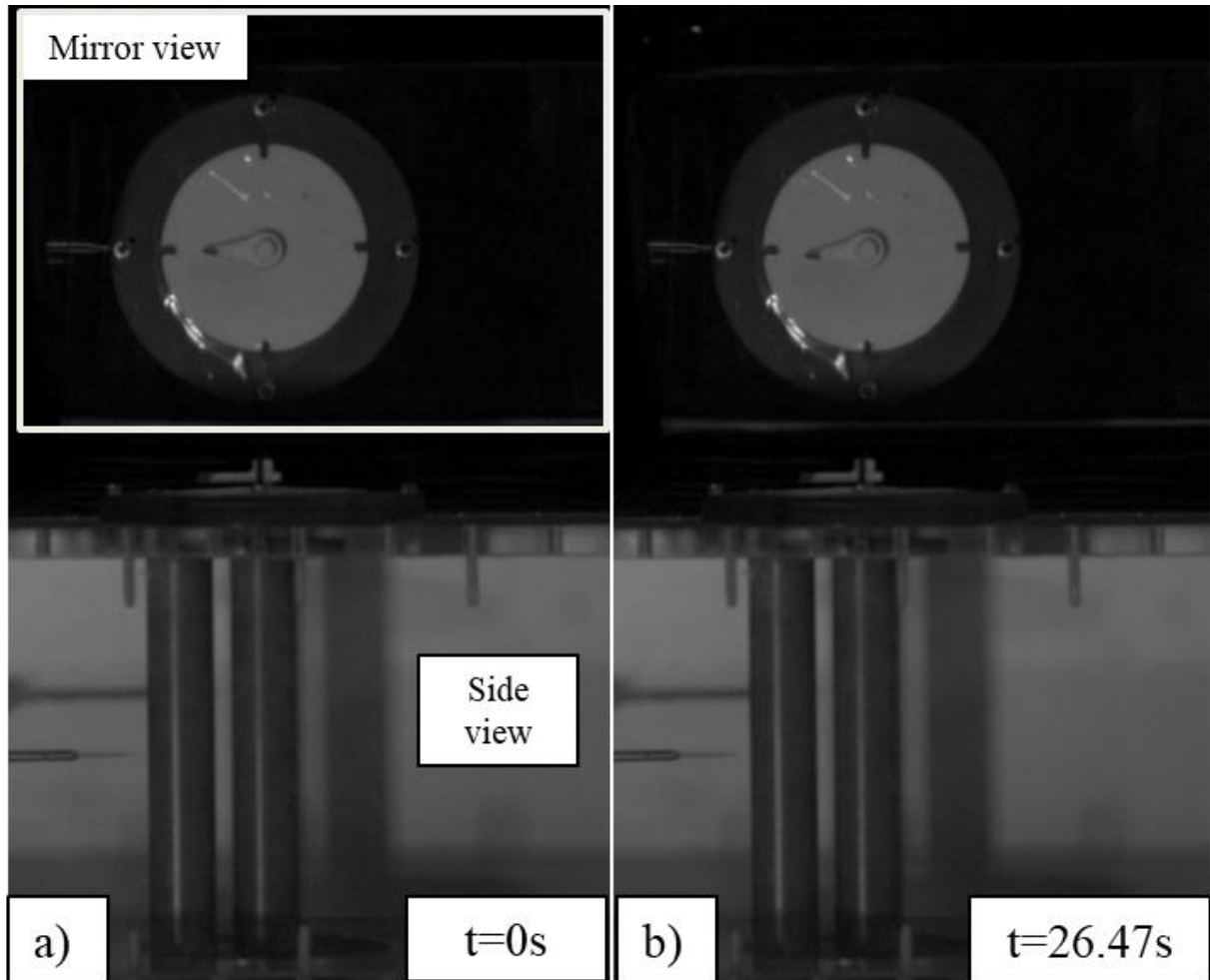


Figure 4.35 – Photographs from the high-speed camera for the natural oscillation cylinders, for the reference flow velocity of 10 m/s; the moment in which the acquisition is turned on (a) and the angular peak of this configuration (b).

4.4.2 One obstacle

This subsection presents the results for the free to oscillate cylinders with one obstacle, i.e., the “throat device” was put in the aerodynamic flow channel, as shown in Figure 3.8 (b). The objective of this “throat device” is to accelerate and deviate the flow to the assembly with the cylinders and analyze the effects on the assembly behavior and the amplitudes of the oscillation process. The blockage ratio increased to 51.3 % with the addition of the “throat device”.

Figure 4.36 presents the results for 5 m/s (a), 7.5 m/s (b), and 10 m/s (c), where the peaks of velocity are higher compared with the natural setup, with no aerodynamical devices, presented in Figure 4.31. As the flow is accelerated, it was expected higher values for this case. For the angular oscillation of the system and reference velocity of 5 m/s, the system is practically stopped. For reference velocities 7.5 m/s and 10 m/s, the angular amplitude is about ± 0.4 rad for both cases, as shown in Figure 4.39.

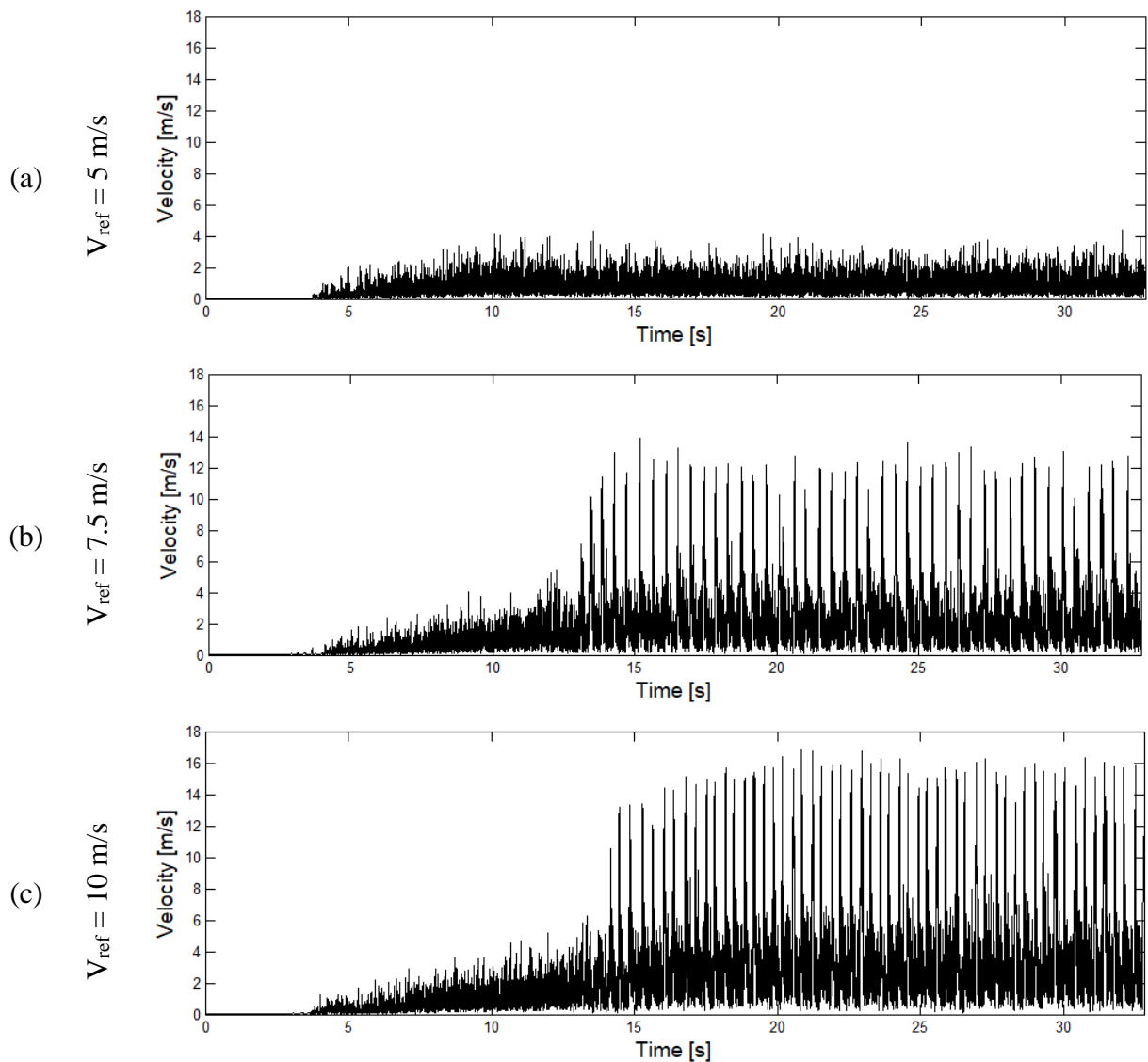


Figure 4.36 – Velocity signals for reference velocity 5 m/s (a), 7.5 m/s (b), and 10 m/s (c), respectively; free to oscillate cylinders, one obstacle setup.

The reconstructed signal of velocity with DWT is shown in Figure 4.37 for 5 m/s (a), 7.5 m/s (b) and 10 m/s (c). Figure 4.37 presents higher values of velocity compared with the experiment in Figure 4.32, but with lower amplitudes and less quantity of oscillations.

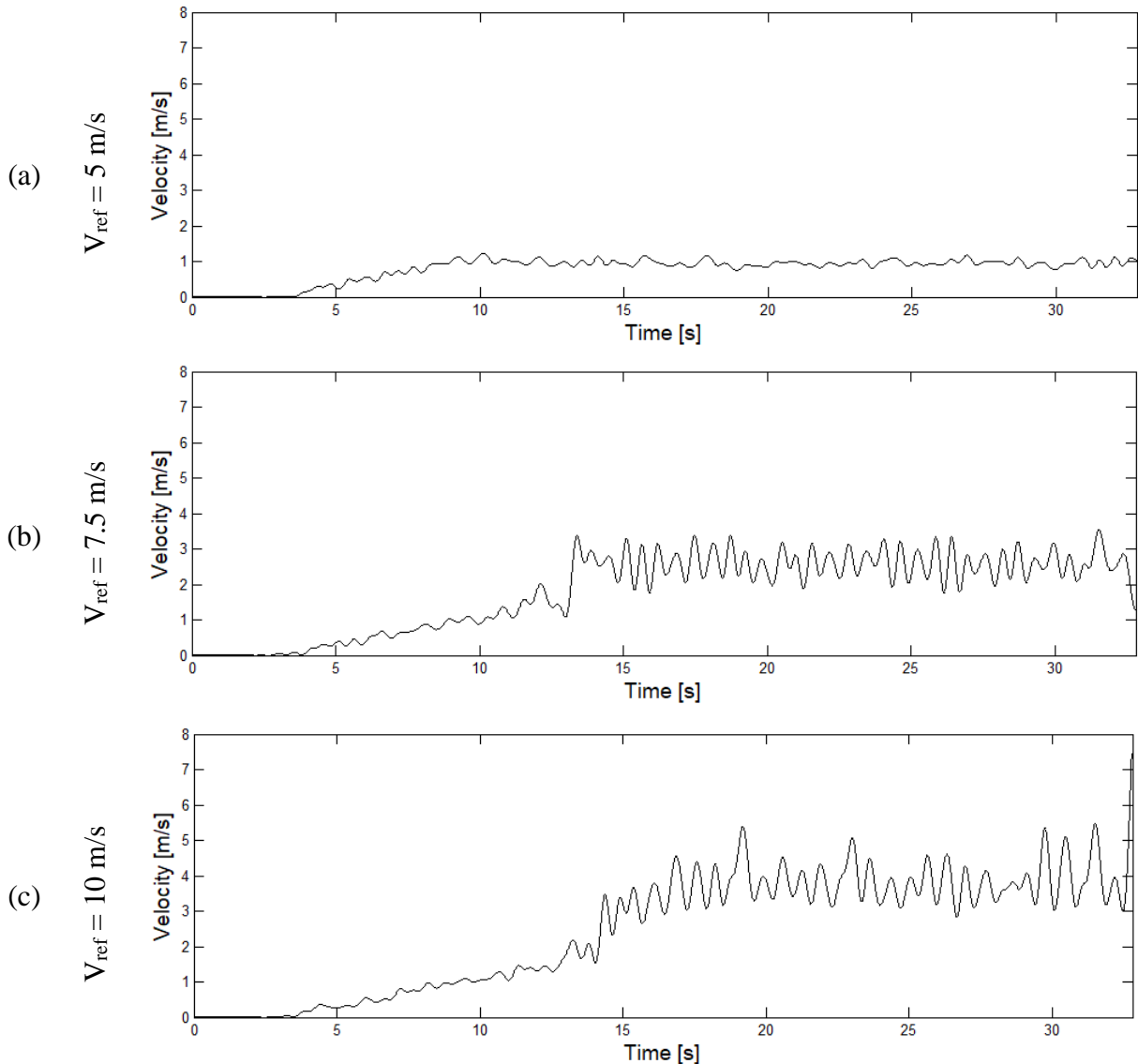


Figure 4.37 – Reconstruction of the signals using DWT for reference velocity 5 m/s (a), 7.5 m/s (b), and 10 m/s (c), respectively; free to oscillate cylinders, one obstacle setup.

Figure 4.38 (a), (b), and (c) presents the continuous wavelet transform results for the velocity signals of Figure 4.36, in the range between 1–250 Hz and bandwidth of 1 Hz. In this case, energy concentration is perceived in the lower values of frequency (20–30 Hz) for the cases with a velocity equal to 7.5 m/s and 10 m/s, corresponding to Figure 4.38 (b) and (c),

respectively. This energy concentration is due to the fact of higher amplitudes in velocity fluctuations, which was not visible in the natural experiment (Figure 4.33).

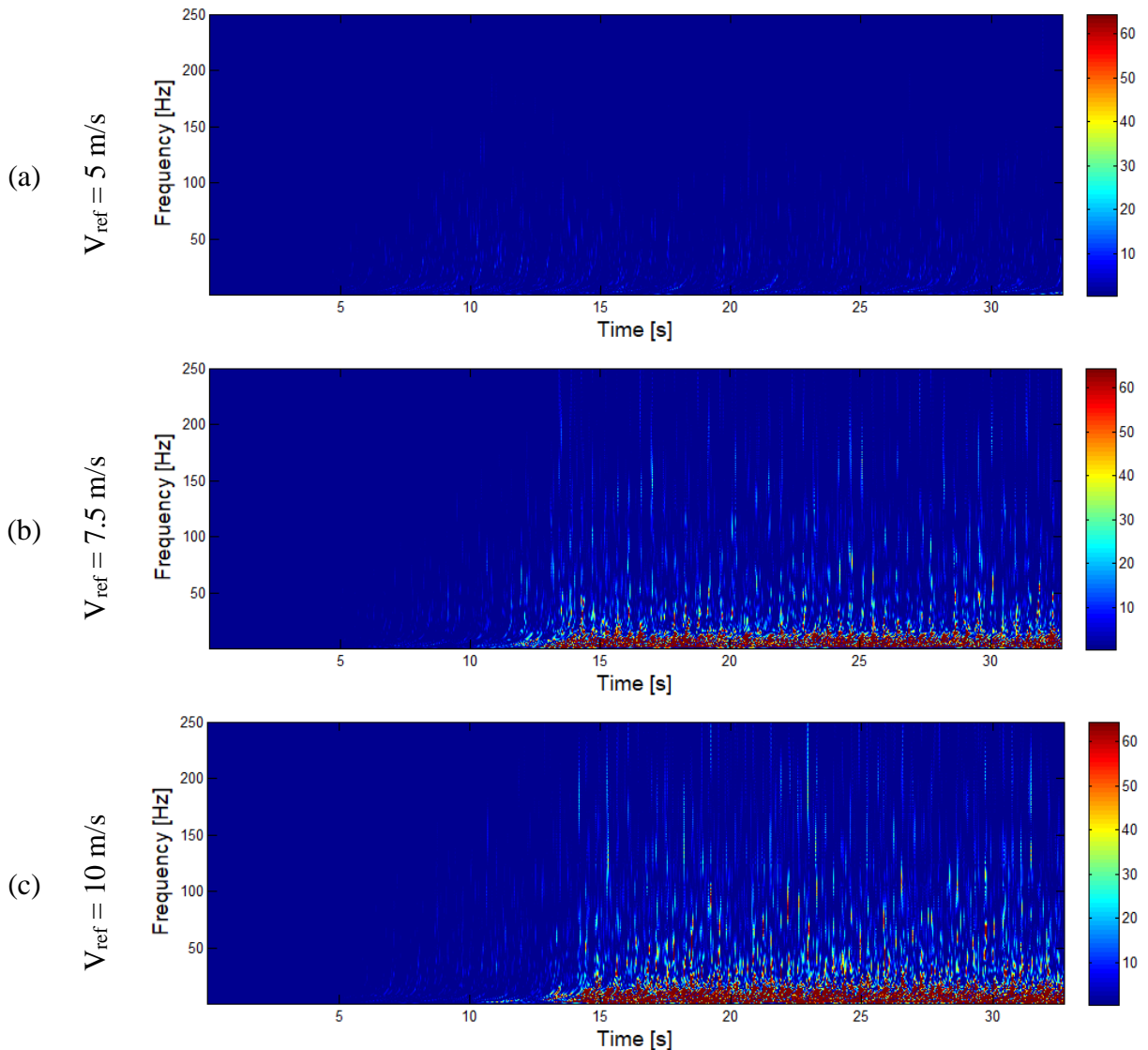


Figure 4.38 – CWT from the velocity signals for reference velocity 5 m/s (a), 7.5 m/s (b), and 10 m/s (c), respectively; free to oscillate cylinders, one obstacle setup.

The behavior of the configuration for reference velocity 10 m/s with one obstacle is presented in Figure 4.40, supporting the results shown in Figure 4.39. Figure 4.40 (a) shows the moment in which the acquisition system of the velocity signal is turned on and (b) represents the angular peak obtained for this configuration. For the case of the reference flow velocity equal to 5 m/s (Figure 4.39a), the assembly was deviated from the center, and for the other velocities, it oscillated deviated from the center. This fact occurred because the flow was accelerated only on one side of the cylinders, deviating the cylinders from the center.

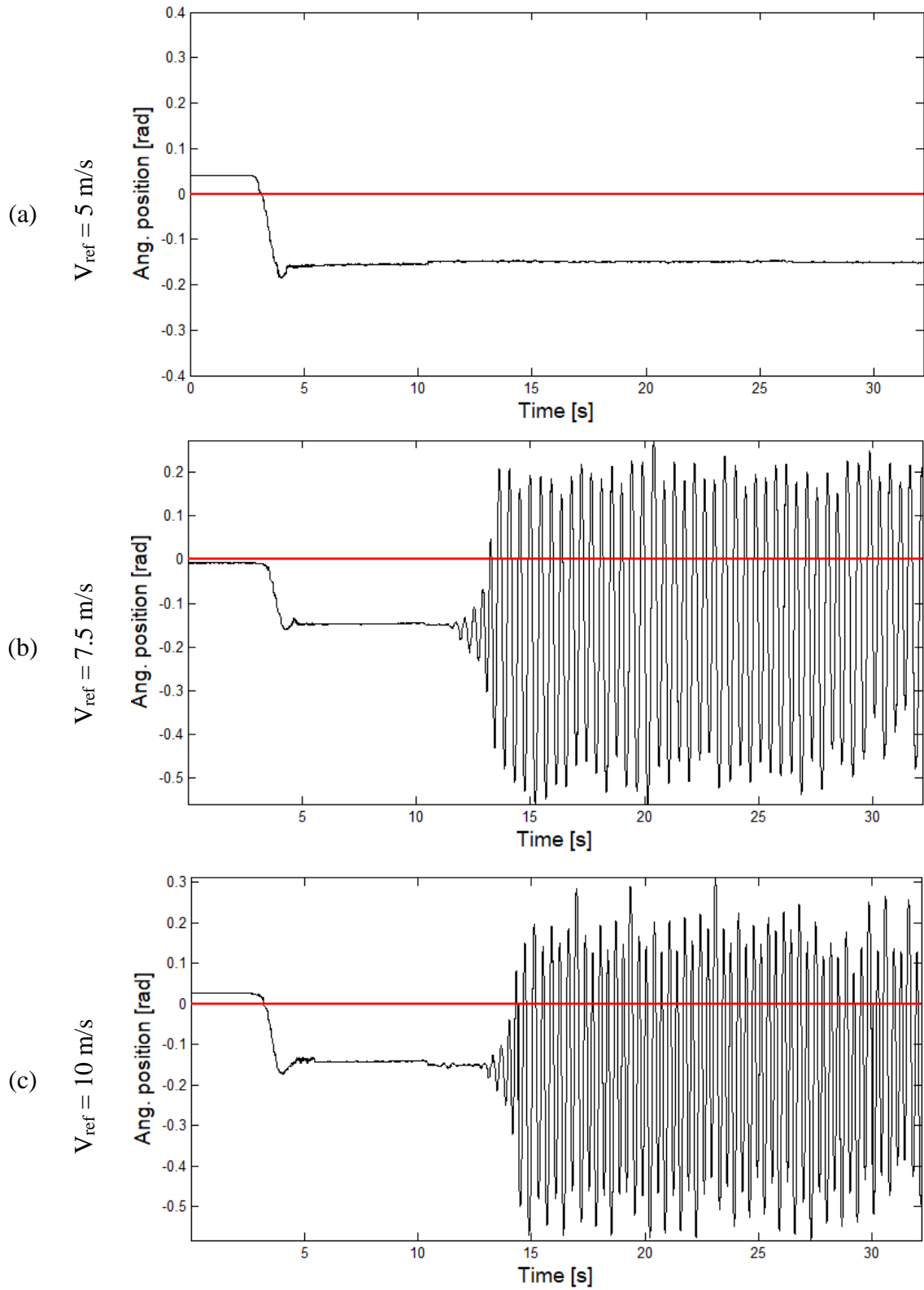


Figure 4.39 – Angular behavior for the free to oscillate cylinders with one obstacle for 5 m/s (a), 7.5 m/s (b) and 10 m/s (c).

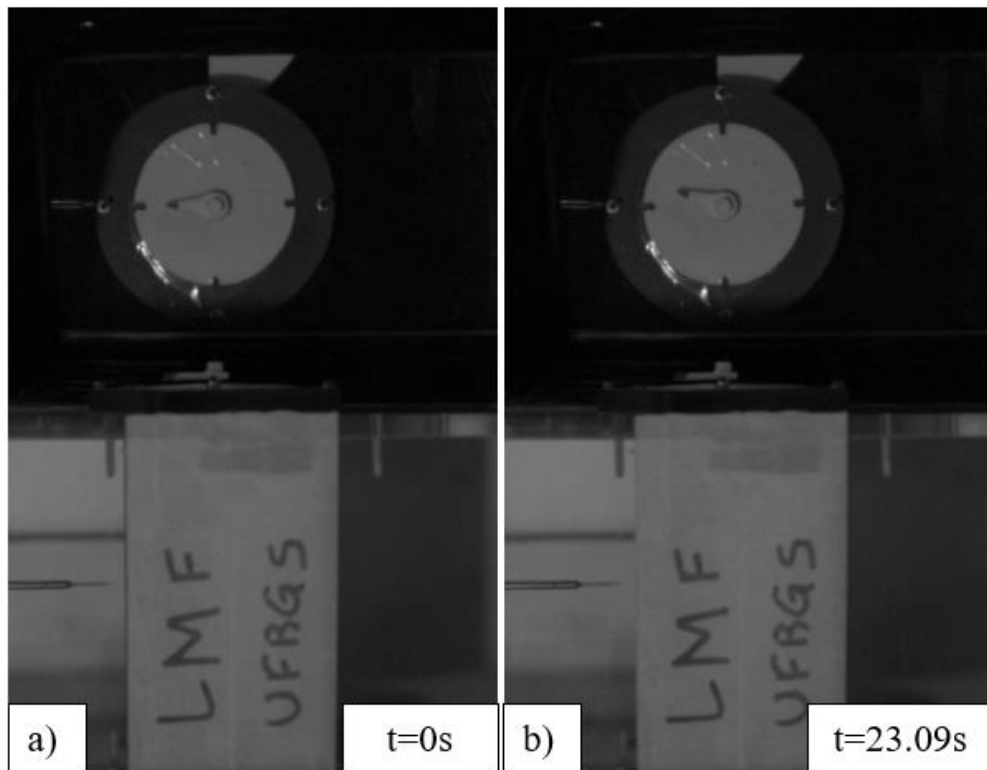


Figure 4.40 – Photographs from the high-speed camera for the oscillation cylinders with one obstacle, for the reference flow velocity of 10 m/s; the moment in which the acquisition is turned on (a) and the angular peak of this configuration (b).

4.4.3 Two obstacles

The two obstacles experiment comprehends the results considering two “throat devices” placed in the aerodynamic flow channel (Figure 3.8c), in order to accelerate the flow more than the experiment proposed in section 4.4.2. Every “throat device” increases the blockage ratio; for this case, the blockage ratio increased to 76.7%.

Figure 4.41 presents the results for 5 m/s (a), 7.5 m/s (b), and 10 m/s (c), where the peaks of velocity are higher compared with the natural and one obstacle assemblies. Higher oscillations and amplitudes in the peaks of velocity are visible even in Figure 4.41 (a), a fact which was observed in the angular oscillations as well, shown in Figure 4.44 (a), achieving ± 0.6 rad as amplitude for reference velocity equal to 5 m/s, and ± 0.7 rad as amplitude for the other velocities.

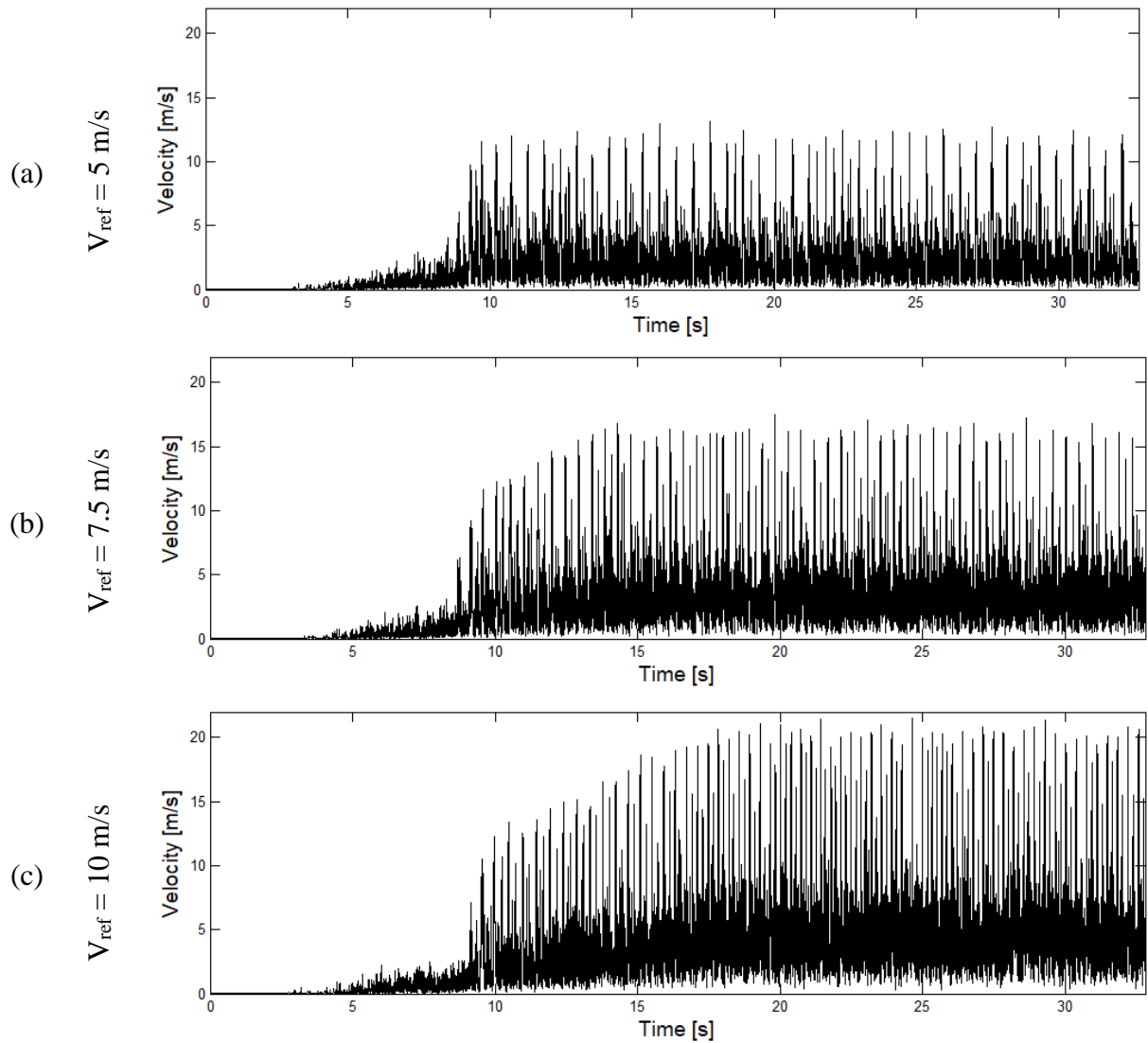


Figure 4.41 – Velocity signals for reference velocity 5m/s (a), 7.5 m/s (b), and 10 m/s (c), respectively; free to oscillate cylinders, two obstacle setup.

Reconstructed signals using DWT are presented in Figure 4.42 (a), (b) and (c) for the velocities 5 m/s, 7.5 m/s and 10 m/s, respectively. Velocity fluctuations are visible for all reference velocities, and the velocity levels for reference velocity 5 m/s are higher (Figure 4.42a) than the levels presented in Figure 4.37 (a). Figure 4.42 (b) and (c) present similar velocity levels compared with Figure 4.37 (b) and (c), with lesser amplitudes in velocity fluctuations.

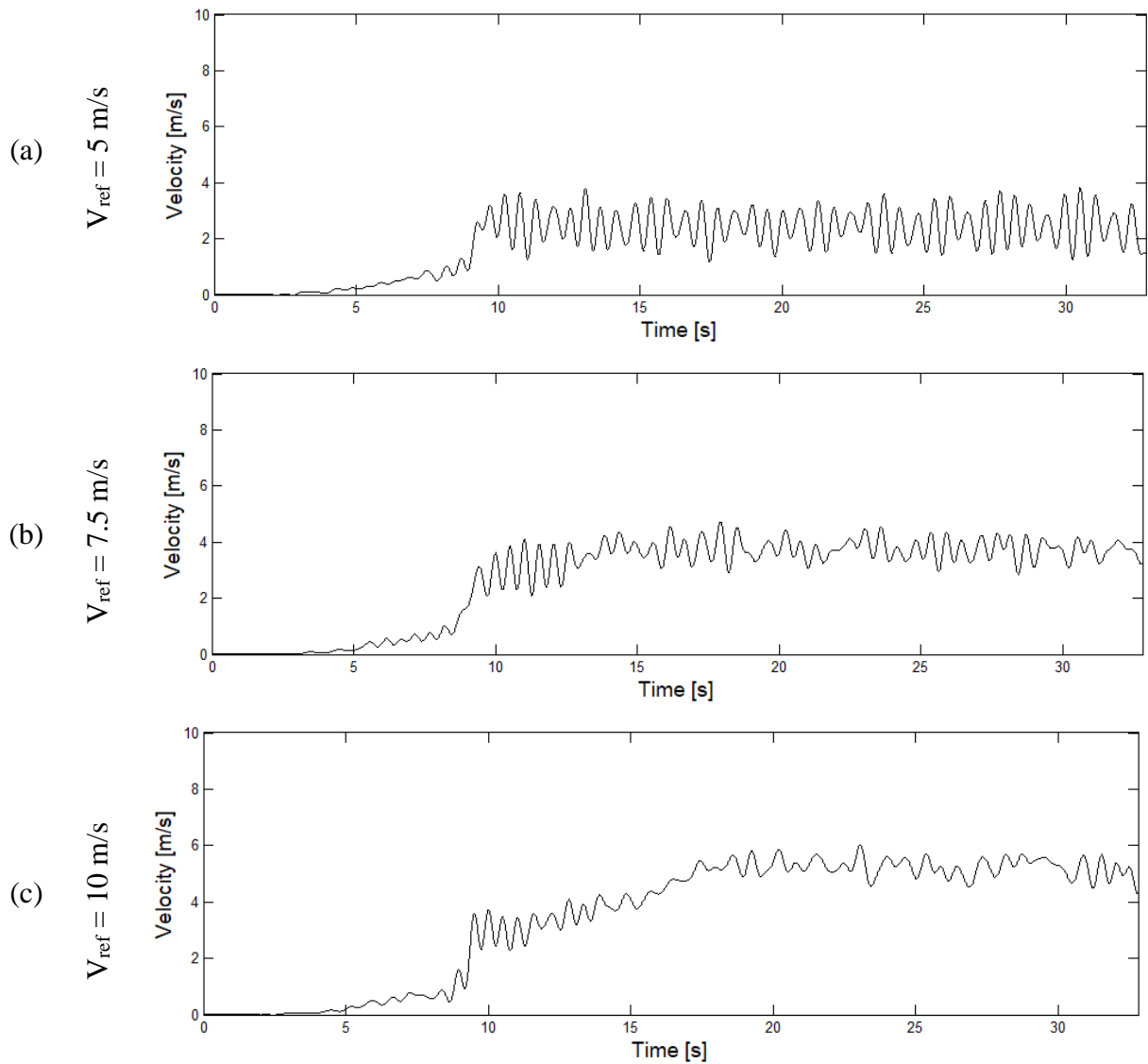


Figure 4.42 – Reconstruction of the signals using DWT for reference velocity 5m/s (a), 7.5 m/s (b), and 10 m/s (c), respectively; free to oscillate cylinders, two obstacle setup.

Figure 4.43 (a), (b), and (c) presents the continuous wavelet transform results for the velocity signals of Figure 4.41, in the range between 1–250 Hz and bandwidth of 1 Hz. Energy concentration in low levels of energy is visible in Figure 4.43 (a), which did not occur in Figure 4.38 (a). Figure 4.43 (b) and (c) present energy concentration in frequency levels ranging between 30 – 45 Hz, which occurred in the case of Figure 4.38 (b) and (c) for lower values of frequency (20 – 30 Hz).

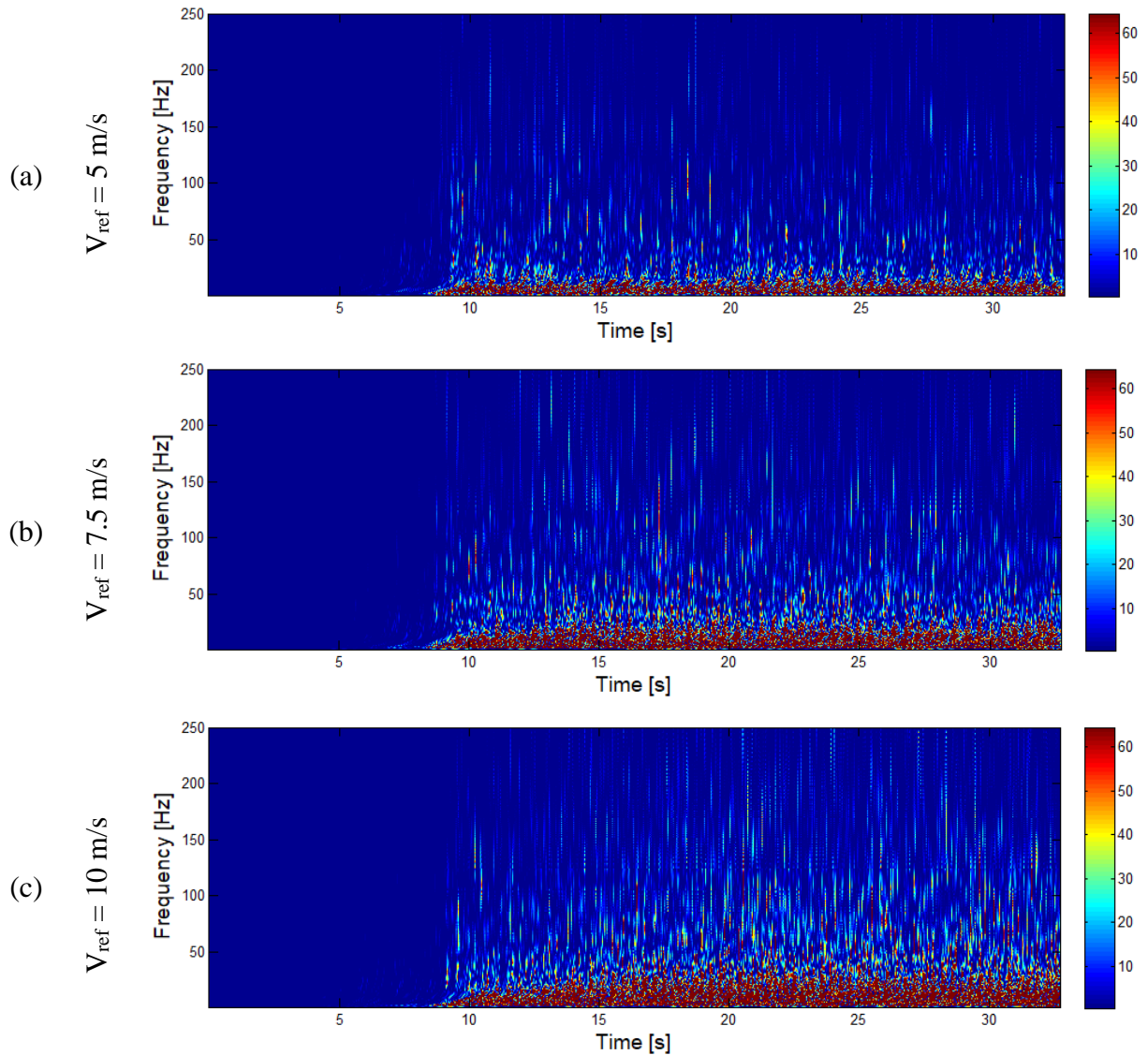


Figure 4.43 – CWT from the velocity signals for reference velocity 5m/s (a), 7.5 m/s (b), and 10 m/s (c), respectively; free to oscillate cylinders, two obstacle setup.

Figure 4.45 shows some photographs generated from the recordings of the high-speed camera employed in this study, for reference velocity 10 m/s. Figure 4.45 (a) shows the moment in which the acquisition of the data was turned on and (b) is the moment in which the configuration achieved the peak of angular position. These results support the results presented in Figure 4.44.

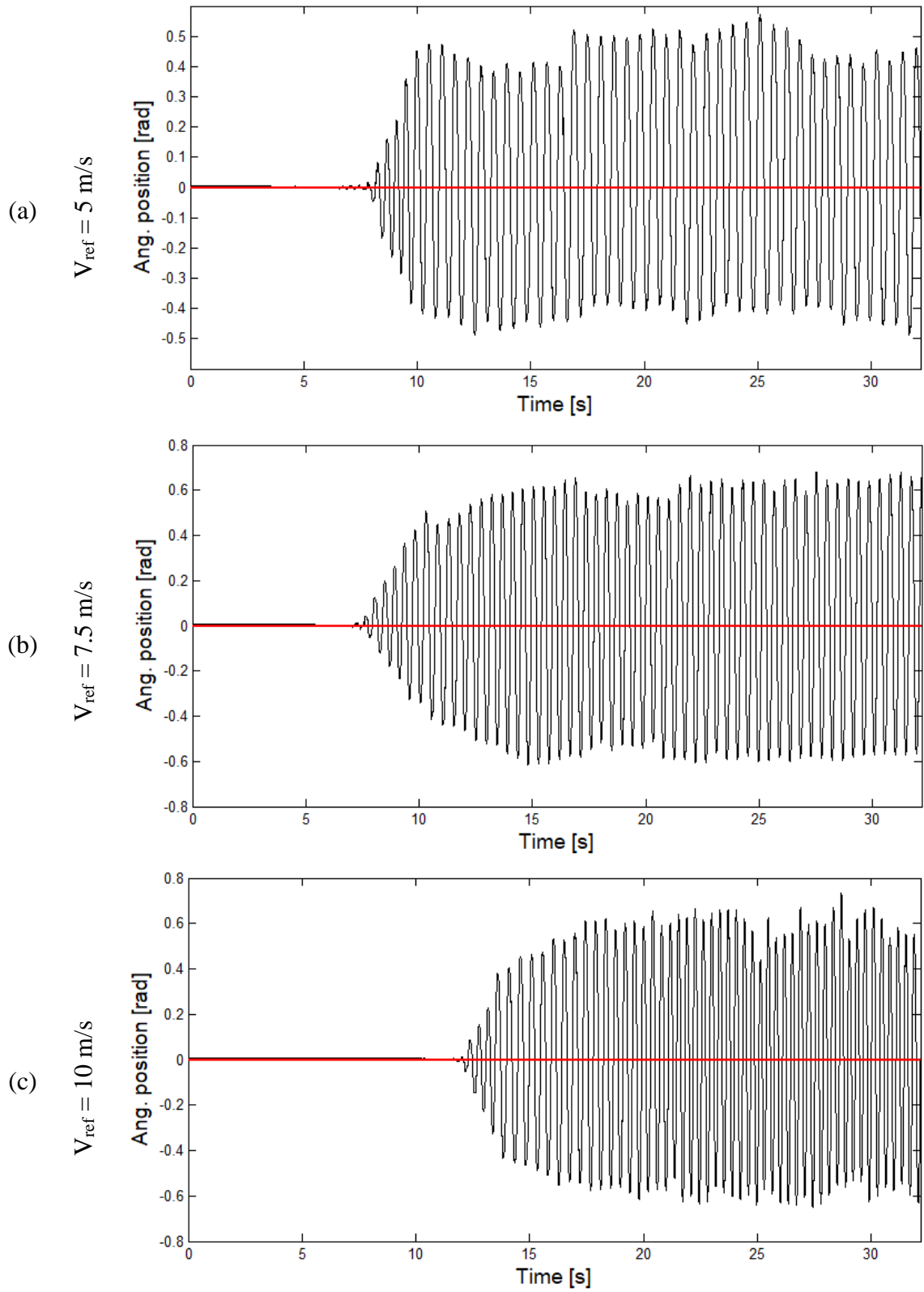


Figure 4.44 – Angular behavior for the free to oscillate cylinders with two obstacles for 5 m/s (a), 7.5 m/s (b), and 10 m/s (c).

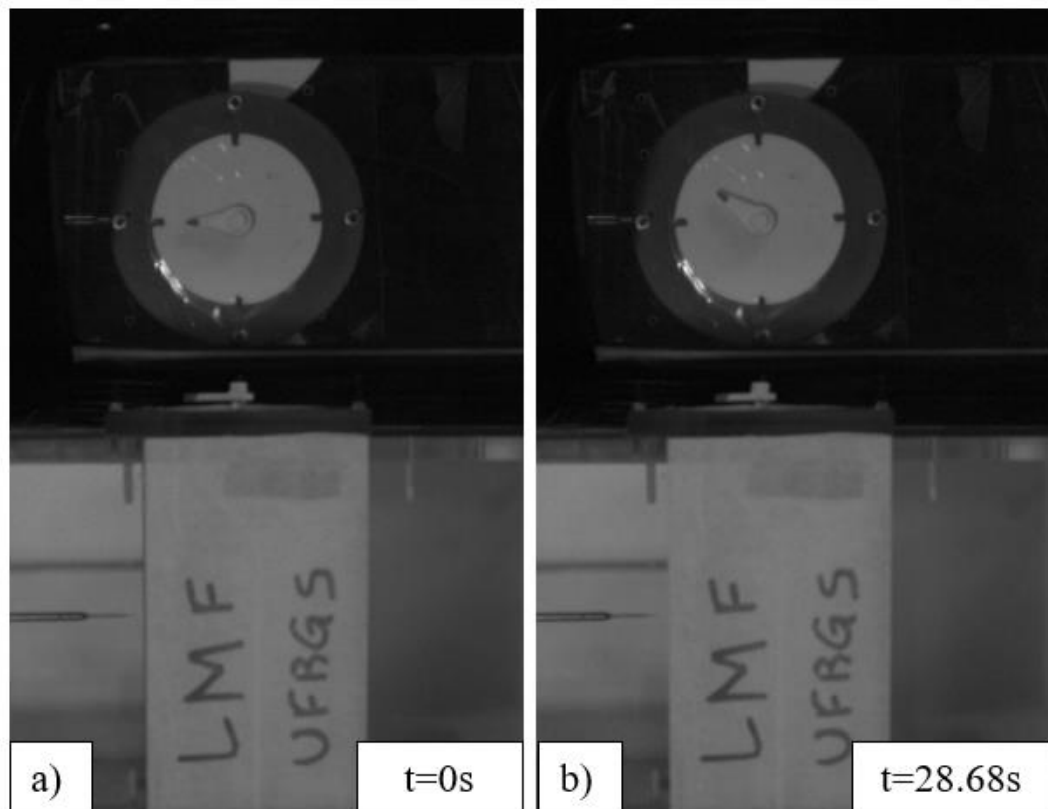


Figure 4.45 – Photographs from the high-speed camera for the oscillation cylinders with 2 obstacles, for the reference flow velocity of 10 m/s; the moment in which the acquisition is turned on (a) and the angular peak of this configuration (b).

4.4.4 Perturbated

The perturbated experiment consisted in perturbing the experiment using a device which is a cylinder with a diameter equal to 32 mm fixed on top of a metal rod. This device was inserted from downstream up to the side of the cylinders, causing a momentary acceleration in the flow near the cylinders, increasing the angular amplitude.

Figure 4.46 (a), (b) and (c) presents the results for velocity signal for reference velocities 5 m/s, 7.5 m/s and 10 m/s, respectively. The increase in the velocity signal of Figure 4.46 represents the exact moment in which the device perturbs and accelerates the flow, increasing the velocity level for a few seconds and then returning to a similar level, being clear its visualization in the reconstructed signal of velocities (DWT) in Figure 4.47. The velocity levels before the perturbation are similar to the natural experiment (results in section 4.4.1). During the perturbation, higher levels of velocity are achieved, which was

expected, once the flow is accelerated momentarily. After the perturbation, the velocity levels stabilize, ranging between 1 – 2 m/s, and are slightly higher than the experiment without aerodynamical devices (section 4.4.1).

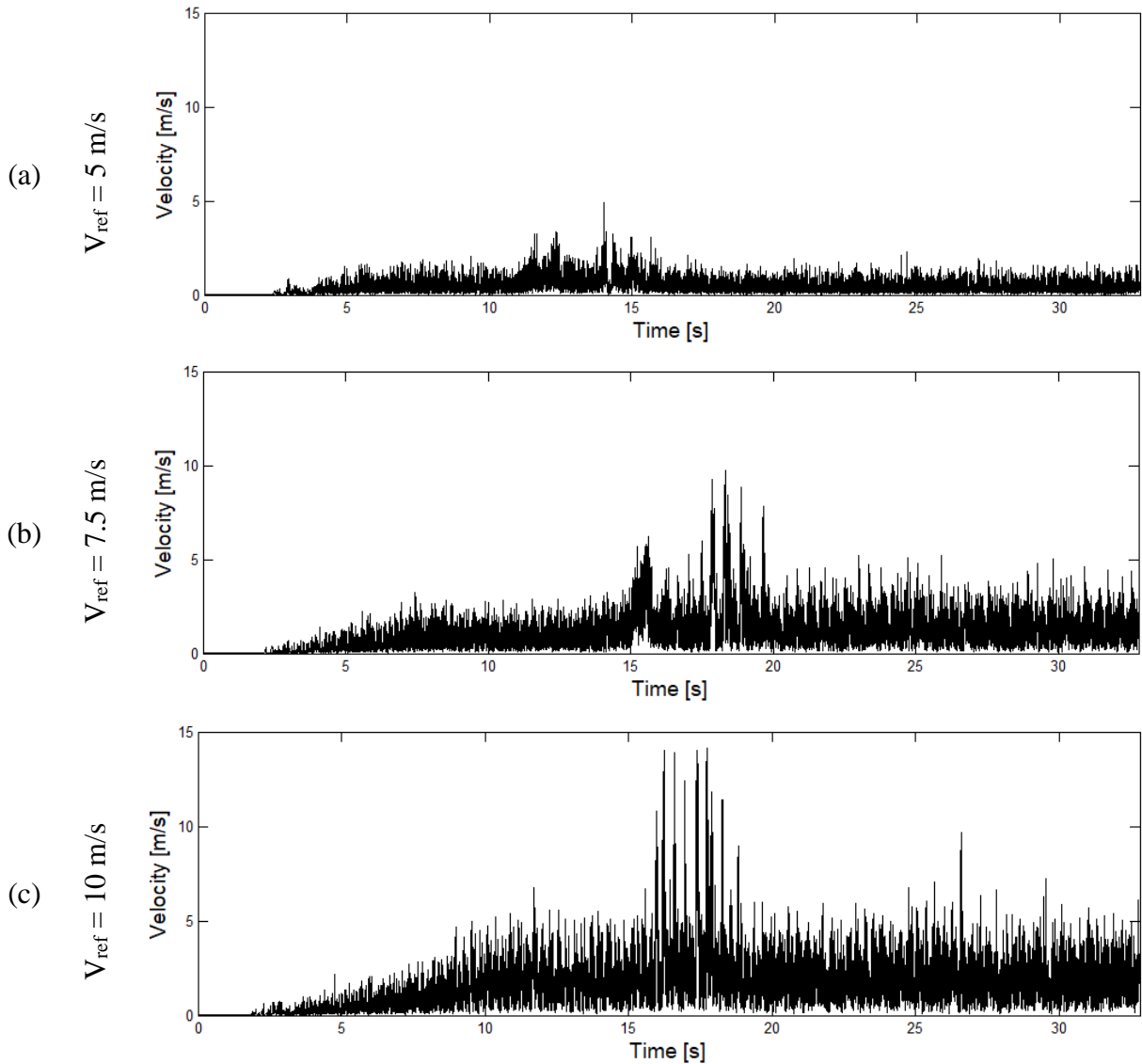


Figure 4.46 – Velocity signals for reference velocity 5m/s (a), 7.5 m/s (b), and 10 m/s (c), respectively; free to oscillate cylinders, perturbed setup.

Figure 4.48 (a), (b), and (c) presents the continuous wavelet transform results for the velocity signals of Figure 4.46, in the range between 1–250 Hz and bandwidth of 1 Hz. Figure 4.48 (a) presents no energy concentration, with similar behavior to the natural experiment (Figure 4.33a). Figure 4.48 (b) and (c) present energy concentration in low levels of frequency

(~20 Hz) in the instant that the device perturbs the flow. This increase in the energy is due to the higher levels of fluctuations and higher levels of velocity in this instant, and then the energy returns to lower levels.

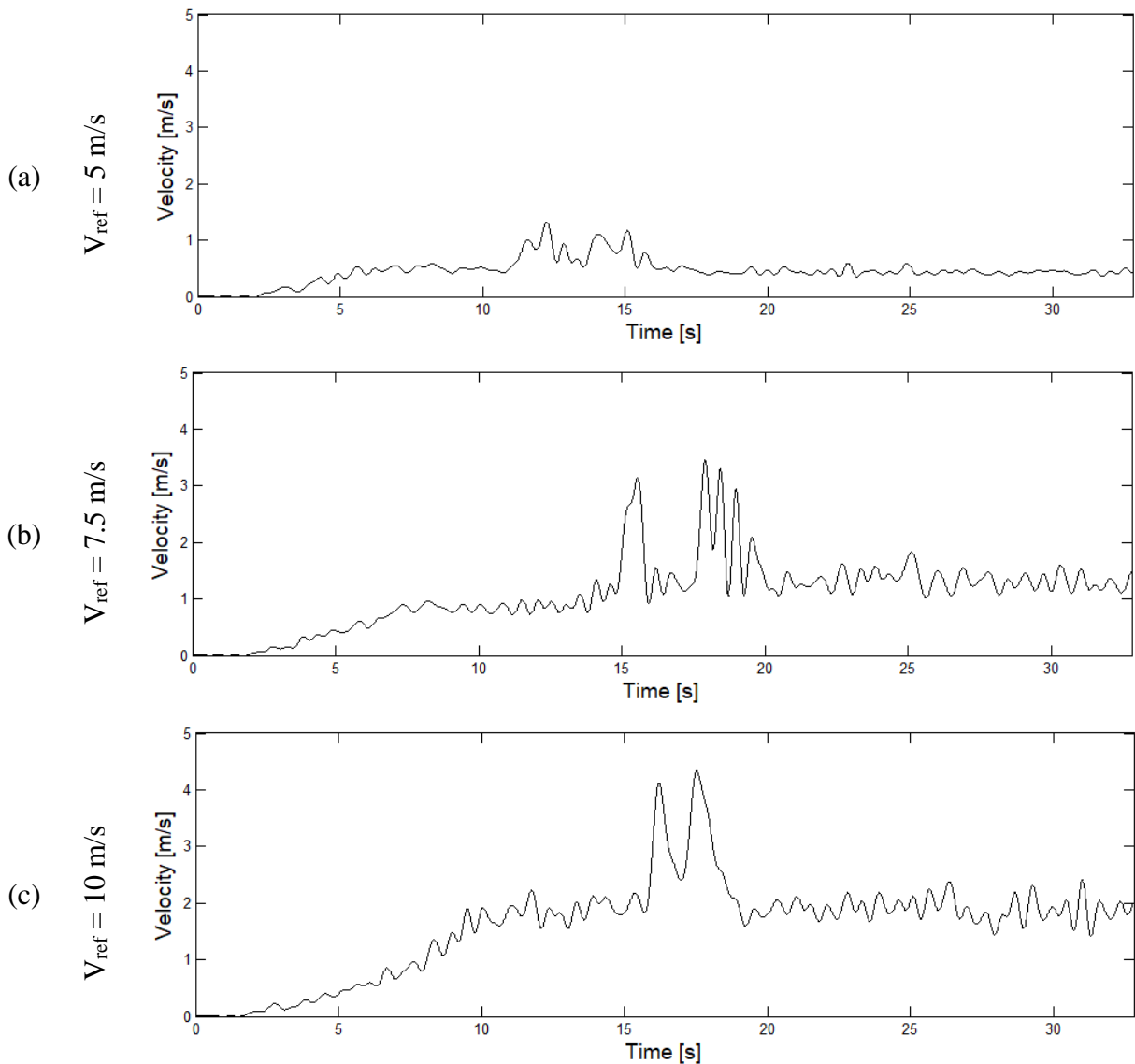


Figure 4.47 – Reconstruction of the signals using DWT for reference velocity 5m/s (a), 7.5 m/s (b), and 10 m/s (c), respectively; free to oscillate cylinders, two obstacle setup.

The angular oscillations for this case are presented in Figure 4.49 and are compared with the results presented for the natural case (Figure 4.34). For each result in Figure 4.49, the system was perturbed at about 15 – 22 s, and this perturbation is clearly observed in all the reference velocities. For the reference velocity equal to 5 m/s (Figure 4.49a), the perturbation was not enough to bring to the system another operation mode, remaining practically stopped

even after the perturbation, being similar to the natural case (Figure 4.34a). For reference velocity equal to 7.5 m/s, after the perturbation, the system achieved an oscillation level higher than the natural case, showing that the perturbation was able to generate another level of balance for the system, remaining permanently in this condition after this perturbation, achieving ± 0.6 rad as angular amplitude. Results for the reference velocity equal to 10 m/s showed a similar behavior founded for the velocity 7.5 m/s, where the system achieved another level of balance after the perturbation, remaining permanently with this behavior, with an angular amplitude equal to ± 0.4 rad. These two last cases showed that this system has two levels of balance. The first explorations about this topic are discussed in APPENDIX E.

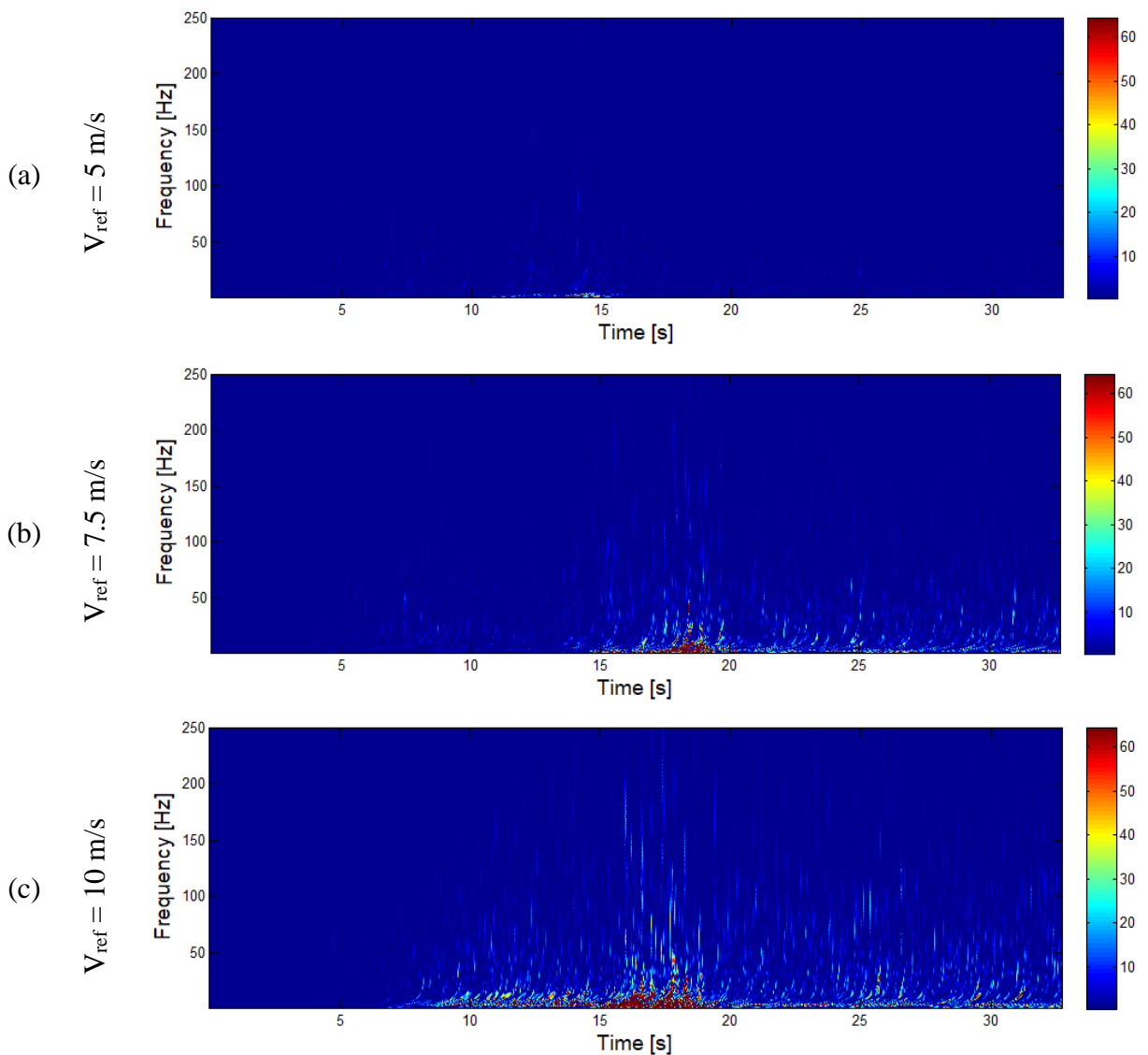


Figure 4.48 – CWT from the velocity signals for reference velocity 5m/s (a), 7.5 m/s (b), and 10 m/s (c), respectively; free to oscillate cylinders, two obstacle setup.

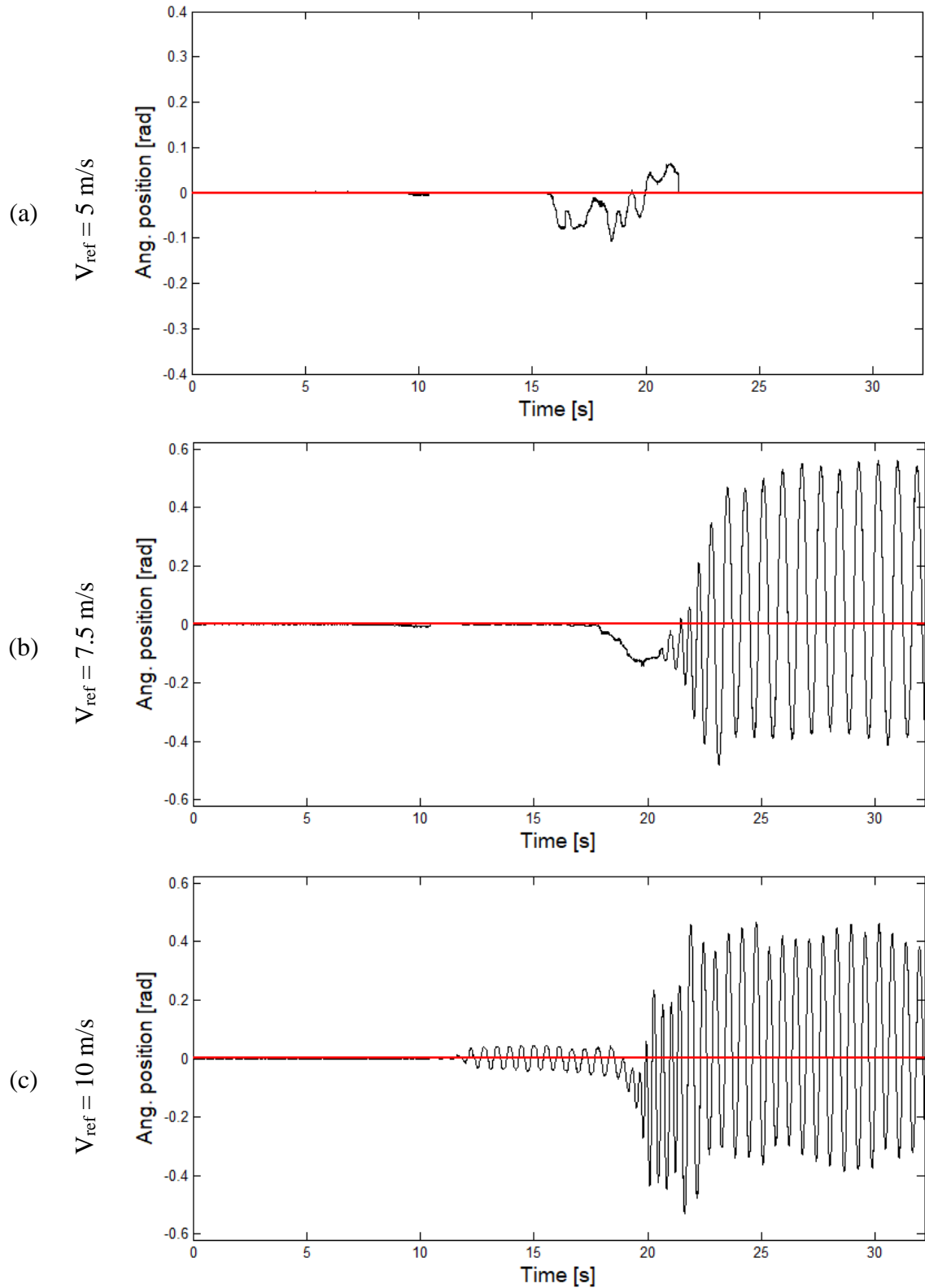


Figure 4.49 – Angular behavior for the perturbed free to oscillate cylinders for 5 m/s (a), 7.5 m/s (b) and 10 m/s (c).

Figure 4.54 shows some photographs from the recordings obtained by means of the high-speed camera, for reference velocity of 10 m/s. Figure 4.54 (a) is the moment in which the data acquisition by the anemometry system was turned on, (b) is when the perturbation is been removed and (c) is the moment in which the configuration achieved the peak of angular position. Figure 4.54 (d-f) presents the introduction of the perturbation in the flow.

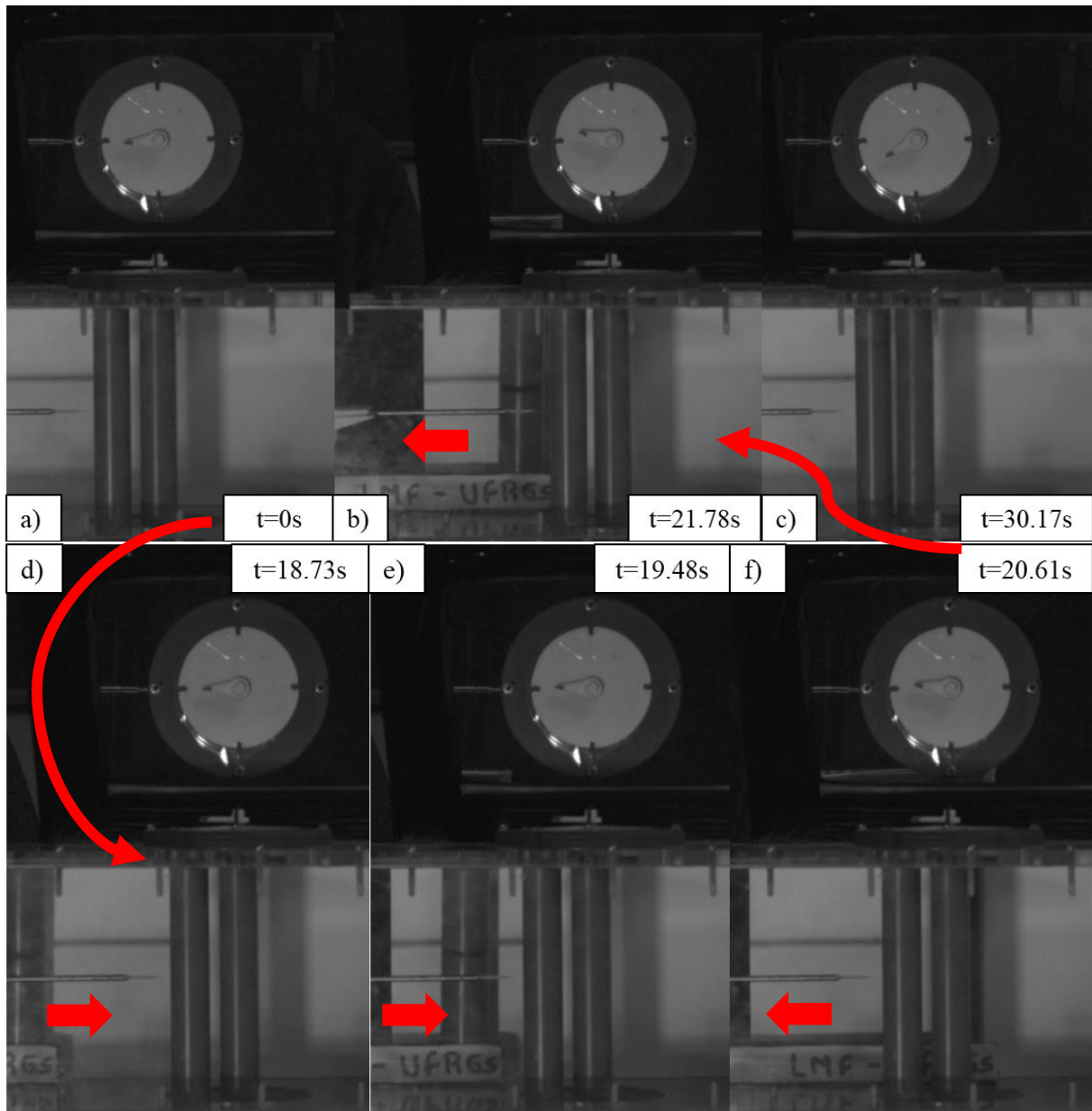


Figure 4.50 – Photographs from the high-speed camera for the perturbed oscillation cylinders; the moment in which the acquisition is turned on (a), perturbation being removed (b), angular peak (c), and details about the insertion of the perturbation in the flow (d-f).

The electrical system employed in the experiment shown in section 4.3.1 (free to rotate cylinders) was tried in these four configurations as well. The generator works better with the rotational movement, which is not the case for these configurations. Using this electrical system, the configurations were not able to produce power. To better explore this idea, a suggestion for future works is to use an appropriate electrical system that allows evaluating the ability to generate power of these configurations.

4.5 Results for the Savonius wind turbine

The results for reference velocity of 5.4 m/s are presented in Figure 4.51 (a) and (b), for Probe 1 and Probe 2, respectively. These velocity levels are better visualized in Figure 4.52, where is presented the reconstruction of the signal by means of DWT. From the results of both probes in Figure 4.52, the velocity starts from rest and starts to increase at about 10 s, achieving a peak of 2.5 m/s at about 12 s, where the turbine turned 90° and started to rotate, achieving a rotational velocity of about 1800 rpm. After 17 s, the velocity level remained almost constant during the experiment, about 0.8 – 1.3 m/s.

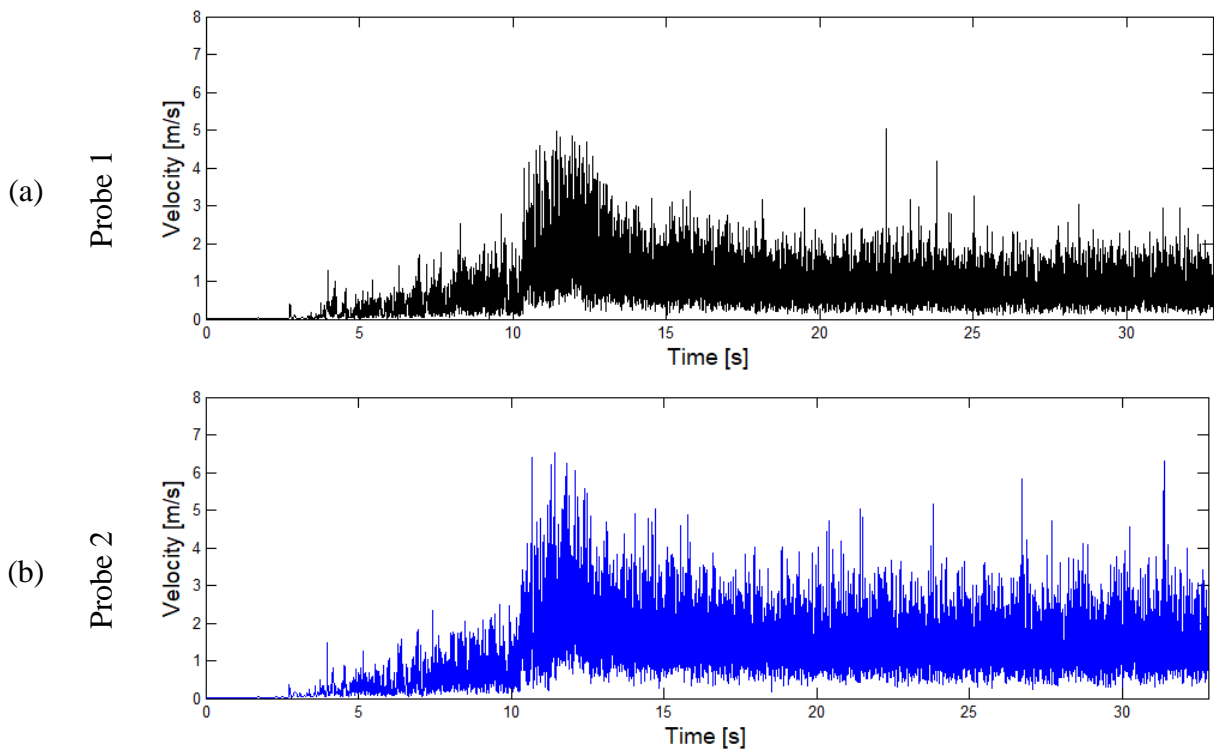


Figure 4.51 – Velocity signals for the wind turbine for Probe 1 (a) and Probe 2 (b), for the reference flow velocity of 5.4 m/s.

Figure 4.53 presents the continuous wavelet transform results from the velocity signals of Figure 4.51, in the range between 1–250 Hz, bandwidth of 1 Hz, showing the energy of the velocity series. Both results have the same main characteristics. Once the values of velocity signals in Figure 4.51 are low and without high fluctuations, the energy of the flow behind the turbine is very low in this case. It was expected lower values for the energy in the flow behind the turbine for this experiment compared with the results of the free to rotate cylinders (sec. 4.3), due to the fact that the Savonius wind turbine converts the kinetic energy into shaft power with more efficiency than the free to rotate cylinders. Thus, the velocity behind the turbine (sec. 4.3) is lesser than the free to rotate cylinders, justifying the low levels of energy found in Figure 4.53.

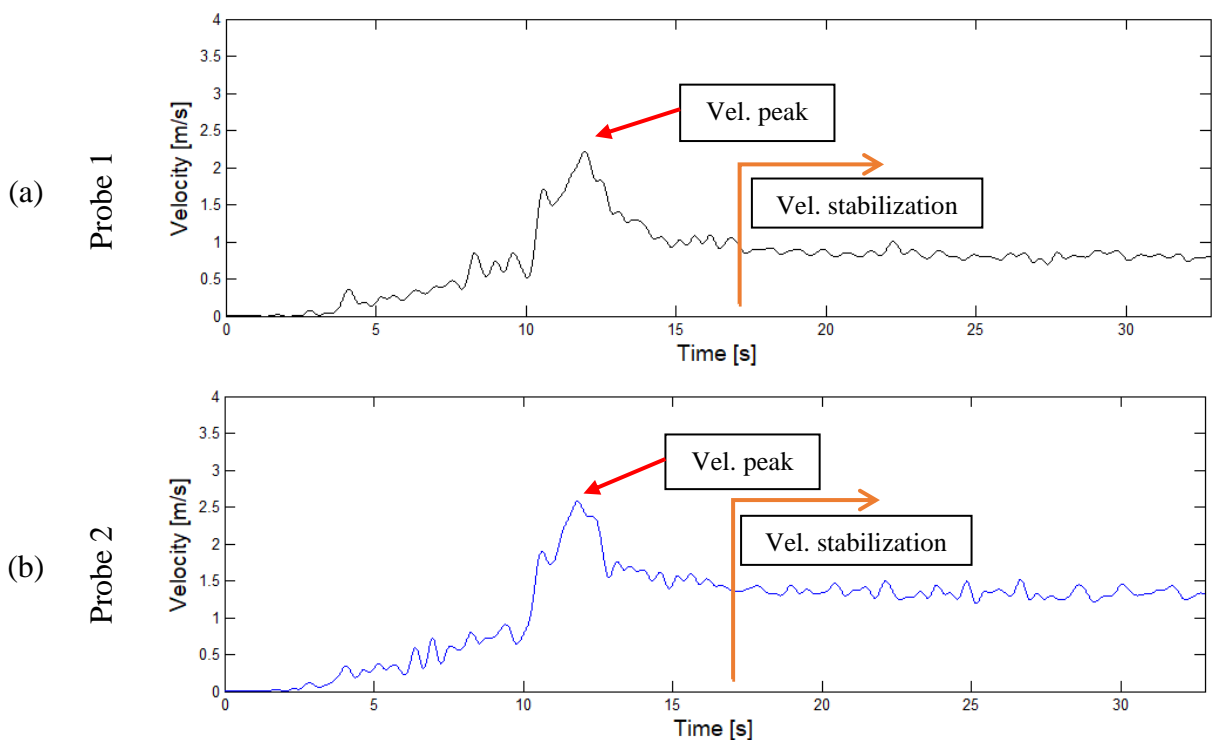


Figure 4.52 – Reconstruction of the signals using DWT for Probe 1 (a) and Probe 2 (b), for the reference flow velocity of 5.4 m/s.

Figure 4.54 shows some photographs from the recordings obtained by means of the high-speed camera for reference velocity 5.4 m/s. Figure 4.54 (a) is the moment that the data acquisition by the anemometry system starts, (b) is a stable state ($\sim 90^\circ$) that the wind turbine achieved before the rotational regime, and (c) shows a moment in which the rotational regime is already achieved.

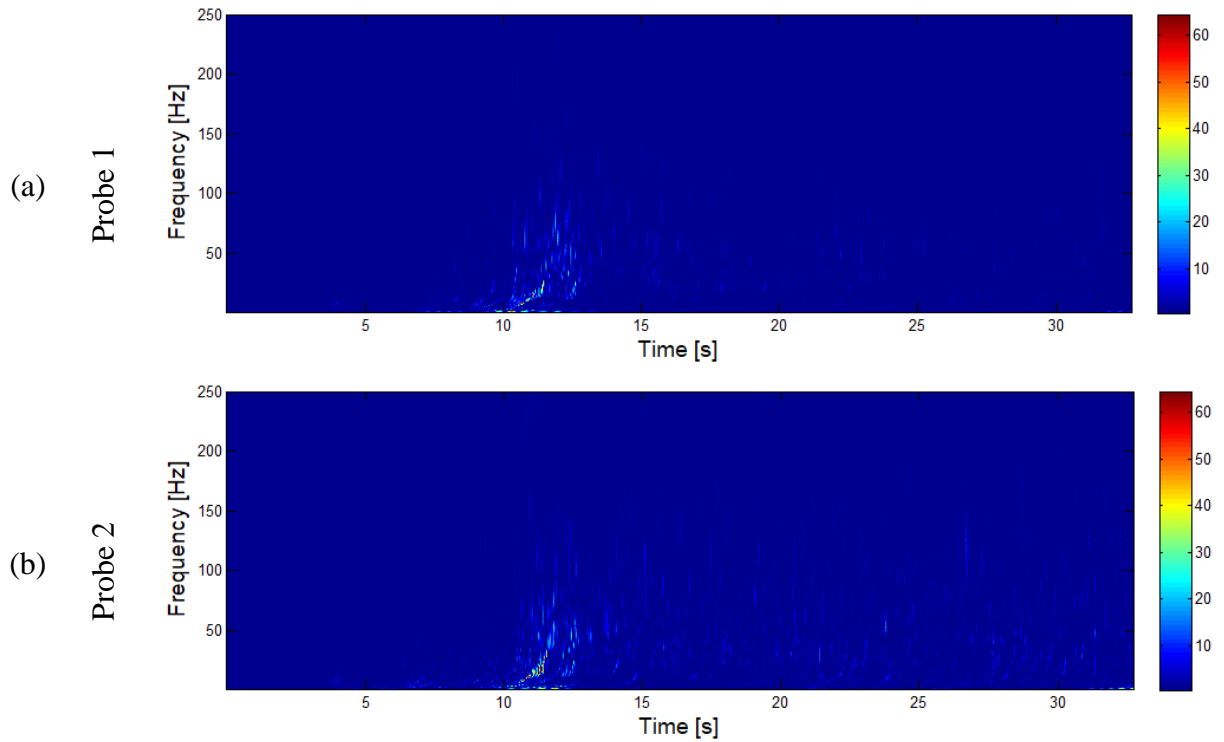


Figure 4.53 – CWT for the velocity signals for Probe 1 (a) and Probe 2 (b), for the reference flow velocity of 5.4 m/s.

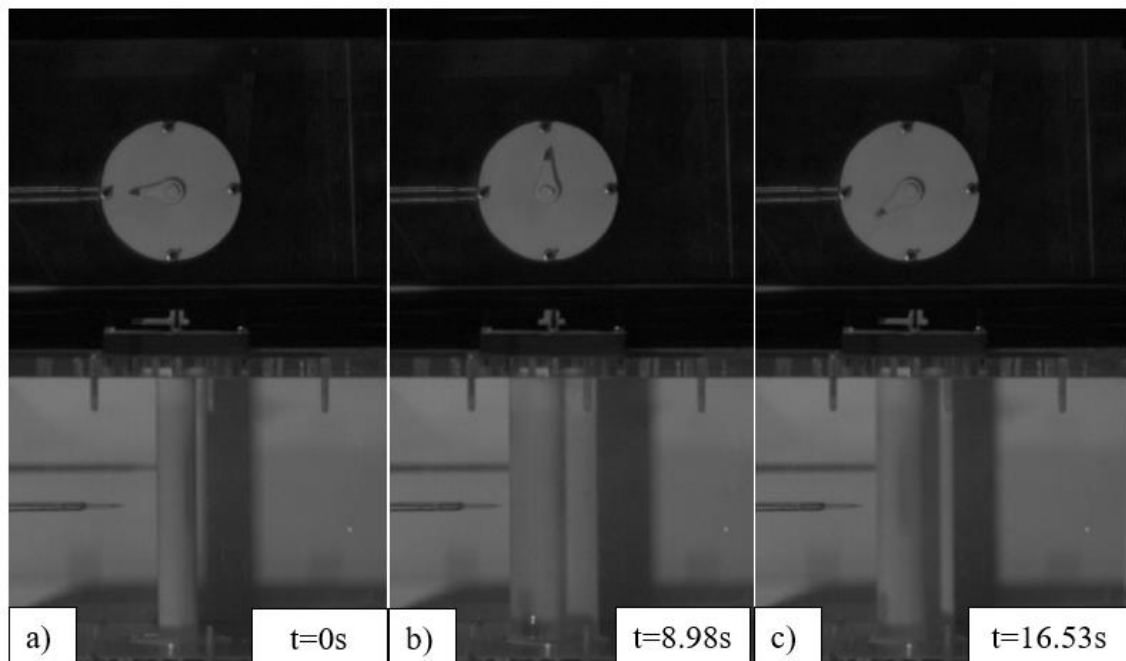


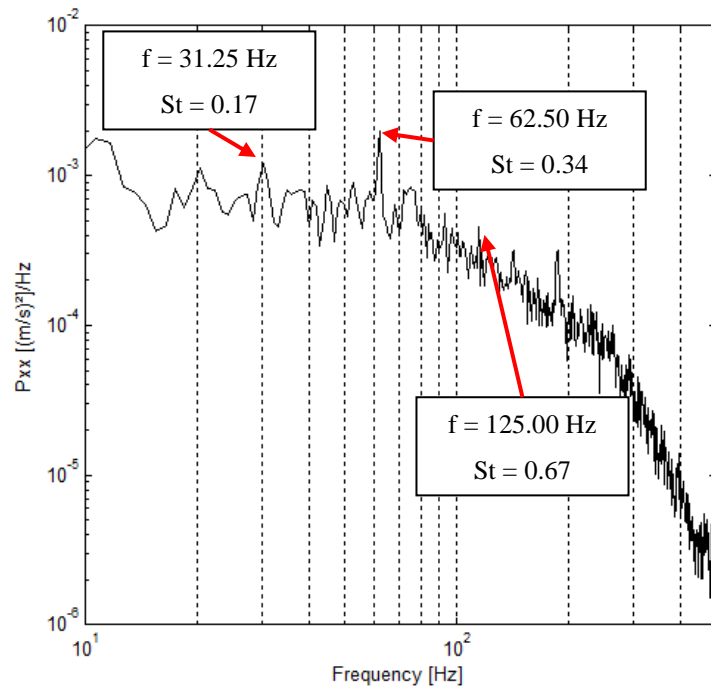
Figure 4.54 – Photographs from the high-speed camera for the wind turbine; rest position (a), stable state ($\sim 90^\circ$) achieved by Savonius turbine (b), and rotational regime (c).

Figure 4.55 presents the power spectrum from the velocity signals presented in Figure 4.51 and the results from both signals present peaks in 31.25 Hz and harmonics in 62.5 Hz, 93.75 Hz, and 125 Hz. The Strouhal numbers, considering the width of a turbine blade (29 mm) and the gap flow (7.29 m/s), are 0.12, 0.25, 0.37, and 0.50, respectively. Computed Strouhal numbers for reference flow velocity (5.4 m/s) are 0.17, 0.34, 0.50 and 0.67. According to Akwa, 2014, the Strouhal number of 0.34 represents the Strouhal number for the Savonius wind turbine positioned 90° with the main flow. This specific position for the Savonius wind turbine was found in this study, presented in Figure 4.54 (b).

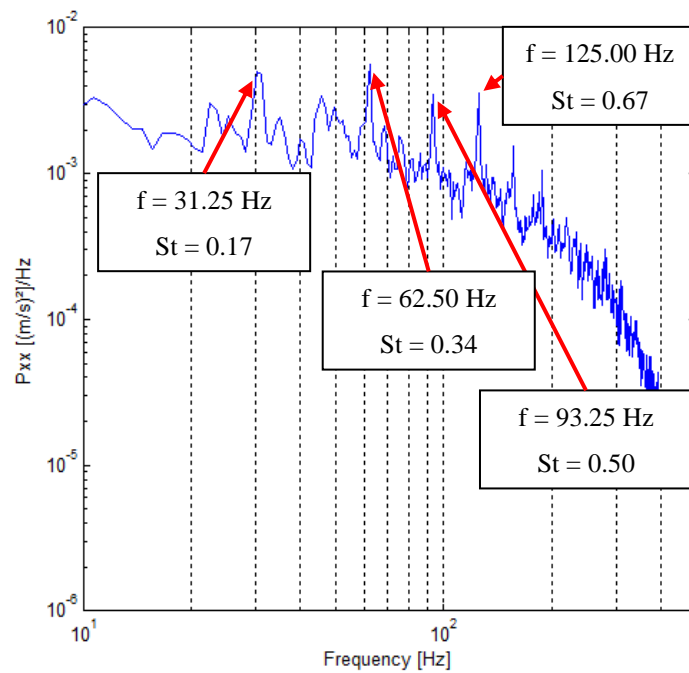
The results for reference velocity 10 m/s are presented in Figure 4.56 (a) and (b), for Probe 1 and Probe 2, respectively. The reconstructed signal from the velocity series, by means of DWT, is presented in Figure 4.57 (a) and (b), for Probe 1 and Probe 2, respectively, where the details of the velocity signal are better visualized. From the results of both probes, the velocity starts from rest and begins to increase at about 12 sec, achieving a peak of 3 m/s, where the turbine turned 90° and started to rotate, similar behavior to presented in Figure 4.54. After 17 s, the velocity level remained constant throughout the experiment, about 2 – 2.5 m/s. The rotational velocity achieved by the Savonius turbine for this experiment was about 4780 rpm. The behavior observed for this Reynolds number is very similar to the behavior found for reference flow velocity of 5.4 m/s.

Figure 4.59 (a) and (b) presents the continuous wavelet transform results for the velocity signal of Figure 4.56, in the range between 1–120Hz, bandwidth of 1 Hz, and shows the energy linked to the velocity series with the same main characteristics in both results. Despite the larger values for the velocity, comparing Figure 4.56 to Figure 4.51, the values of energy associated with the flow behind the turbine are very low, as presented for reference flow velocity of 5.4 m/s in Figure 4.53.

Figure 4.58 presents the power spectrum from the velocity signals presented in Figure 4.56 and the results from both signals present peaks in 39.06 Hz and harmonics in 78.12 Hz, 125.00 Hz, and 156.3 Hz. The Strouhal numbers, considering the width of a turbine blade and the gap flow velocity (13.50 m/s), are 0.08, 0.17, 0.27, and 0.34, respectively. Computed Strouhal numbers for reference flow velocity (10 m/s) are 0.11, 0.23, 0.36 and 0.45. The Strouhal number of 0.23 is related to the rest position of the Savonius turbine and $St = 0.36$ represents the 90° position found for this reference velocity [Akwa, 2014].



(a) - Probe 1



(b) - Probe 2

Figure 4.55 – Power spectrum from velocity signals of wind turbine for Probe 1 (a) and Probe 2 (b), for the reference flow velocity of 5.4 m/s.

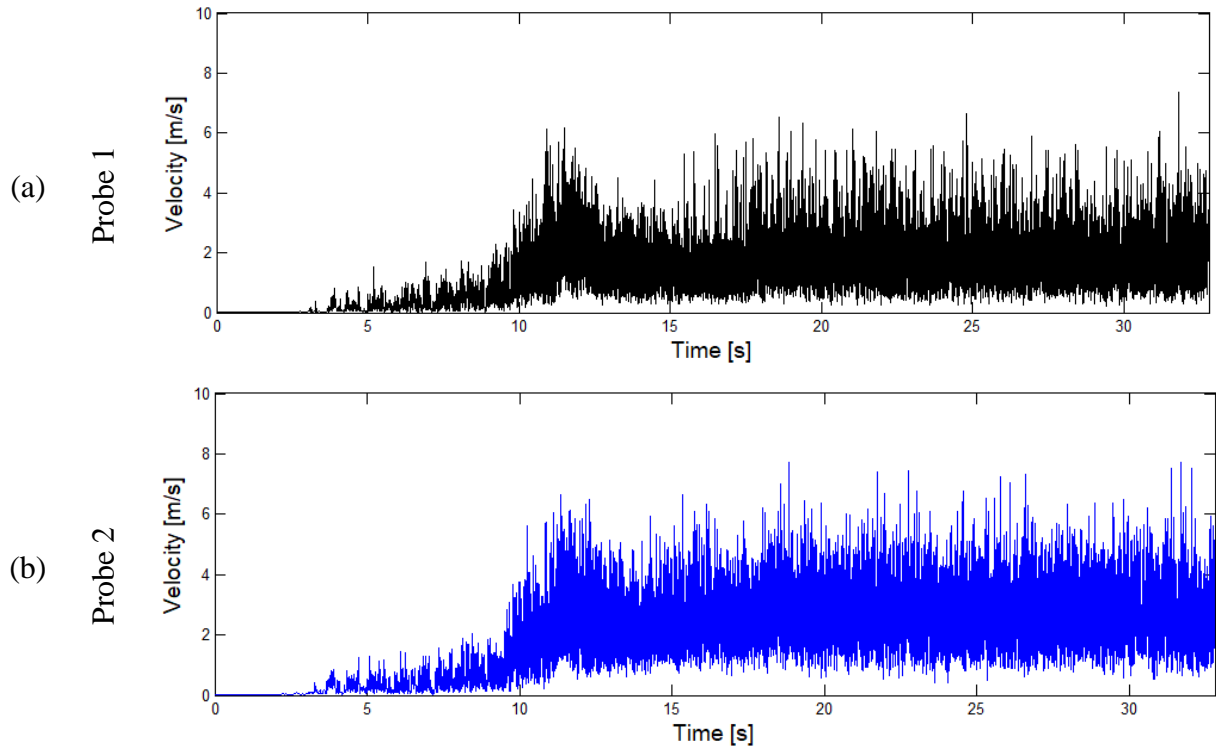


Figure 4.56 – Velocity signals for the wind turbine for Probe 1 (a) and Probe 2 (b), for the reference flow velocity of 10 m/s.

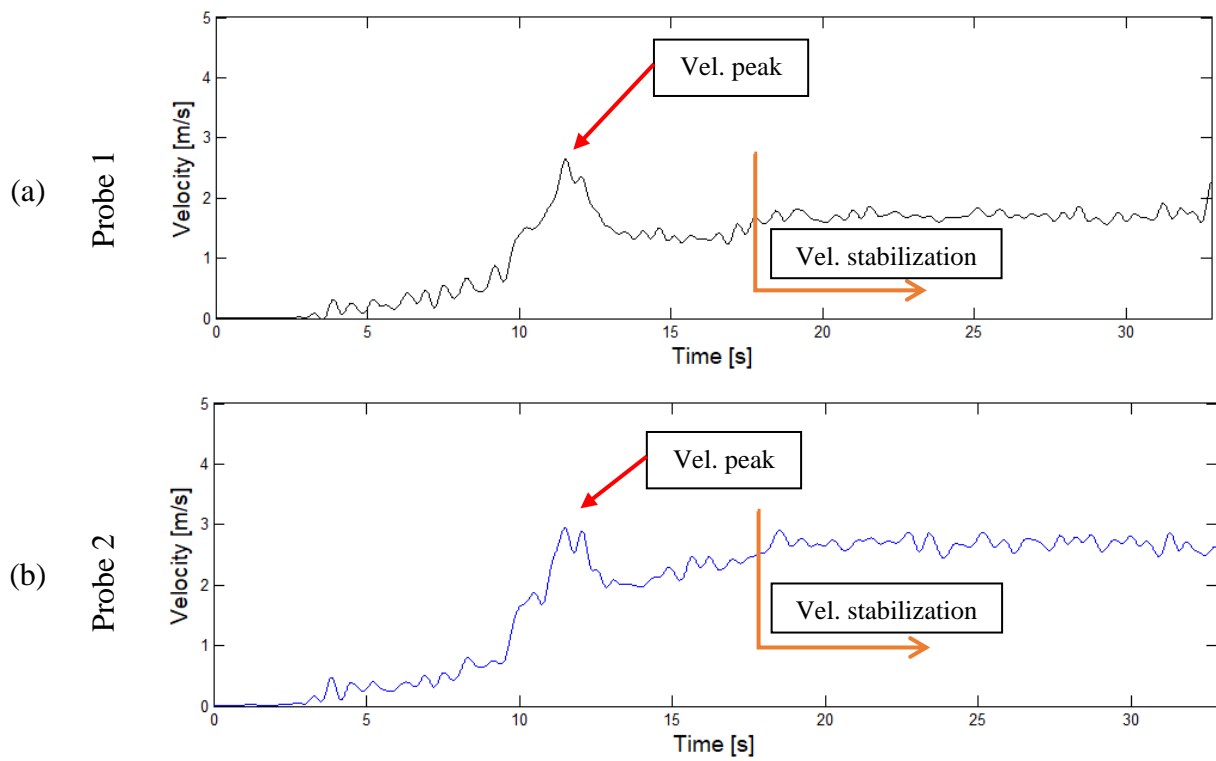
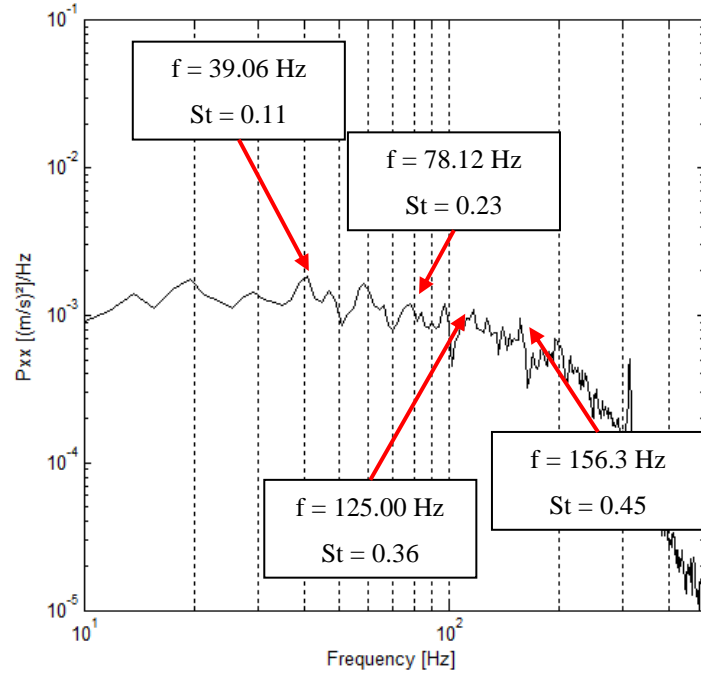
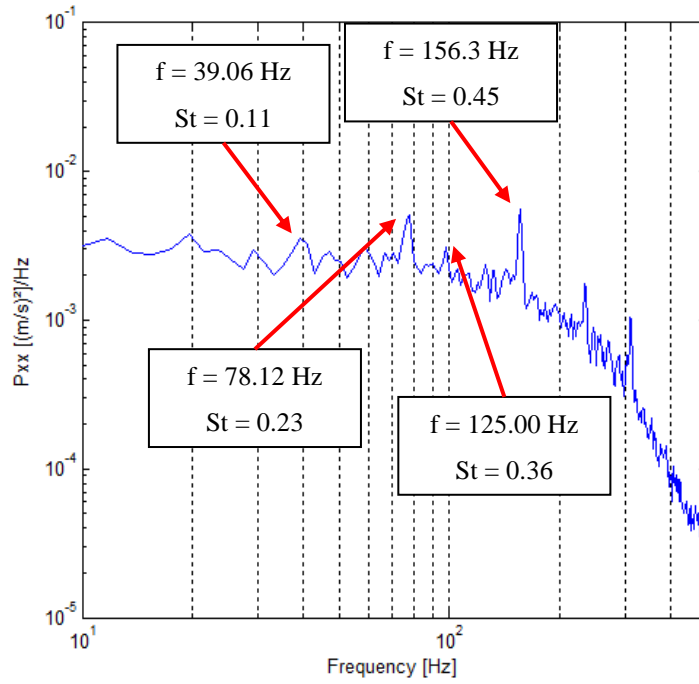


Figure 4.57 – Reconstruction of the signals using DWT for Probe 1 (a) and Probe 2 (b), for the reference flow velocity of 10 m/s.



(a) - Probe 1



(b) - Probe 2

Figure 4.58 – Power spectrum from velocity signals of wind turbine for Probe 1 (a) and Probe 2 (b), reference flow velocity of 10 m/s.

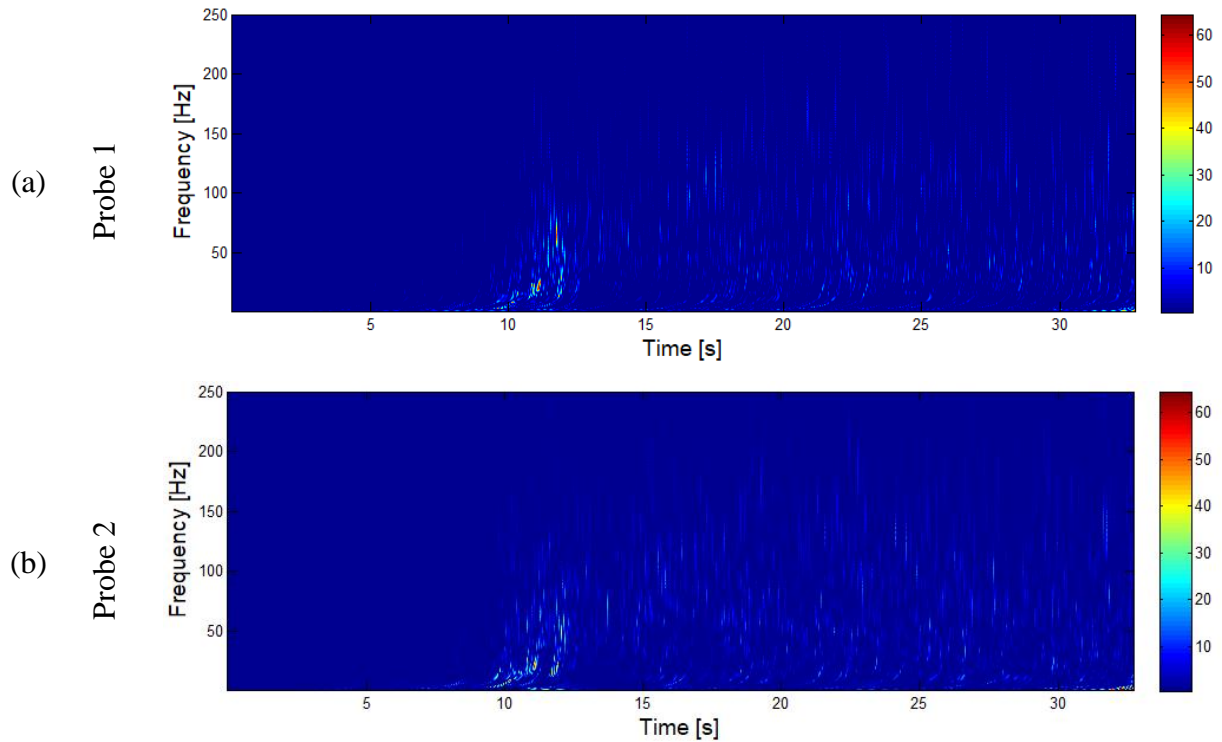


Figure 4.59 – CWT for the velocity signals for Probe 1 (a) and Probe 2 (b), reference flow velocity of 10 m/s.

4.5.1 Results for power generation for the wind turbine

The electrical power generation experiment for the Savonius wind turbine occurred as described in section 3.2.5. For the wind turbine, two experiments with the generator coupled in the assembly were performed, for the free stream velocities 10 m/s and 12.6 m/s. For free stream velocity 10 m/s, the “throat device” was placed to increase the rotational velocity. The results for 10 m/s are presented in Table 4.10 and Figure 4.60.

To generate the results of Table 4.10 and Figure 4.60, the wind turbine started mechanically coupled with the generator, but the generator was turned on only when the rotational velocity reached the stabilization, by connecting the jumpers from the stepper motor to the LEDs. To achieve stabilization, the wind turbine required assistance for starting. Then, the generator was turned on and the rotational velocity of the assembly, electrical tension, and current were evaluated in Table 4.10. In Table 4.10 it is possible to perceive that the rotational

velocity is almost constant. Figure 4.60 shows that the electrical system starts to reduce the generated power after adding 5 LEDs in the system.

Table 4.10 – Power generation results for reference flow velocity of 10 m/s.

| N° de LEDs [un.] | rpm | U [V] | i [mA] | P [mW] |
|------------------|------|-------|--------|--------|
| 0 | 4480 | – | – | – |
| 1 | 4350 | 1.44 | 68.7 | 98.93 |
| 2 | 4400 | 1.51 | 71.2 | 107.65 |
| 3 | 4460 | 1.57 | 73.7 | 115.71 |
| 4 | 4460 | 1.61 | 74.4 | 119.78 |
| 5 | 4460 | 1.60 | 74.35 | 118.96 |

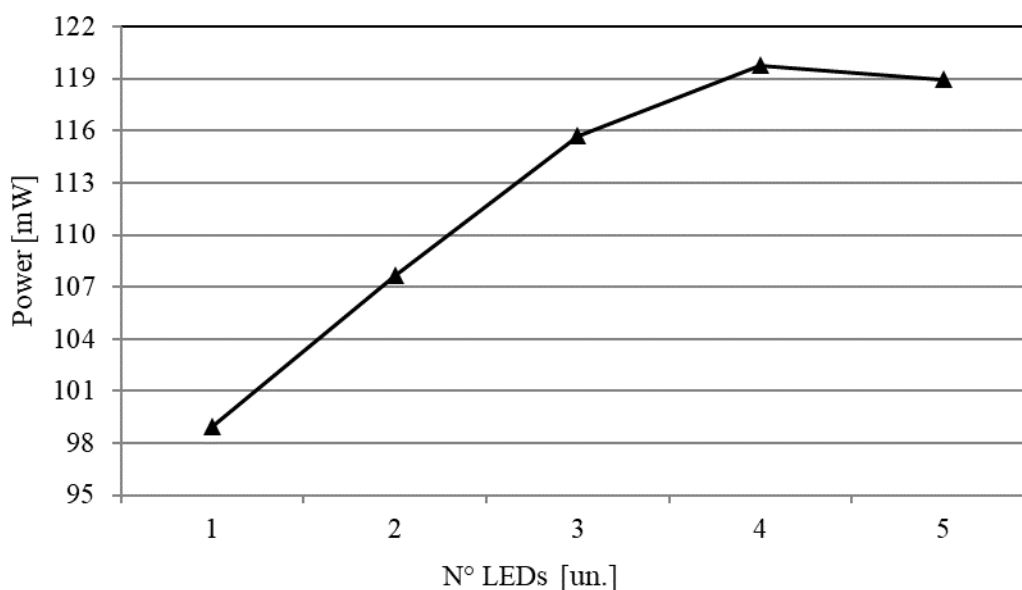


Figure 4.60 – Power generation obtained for reference flow velocity of 10 m/s.

For free stream velocity 12.6 m/s, no aerodynamical device was used to help to improve the rotational velocity. The results for 12.6 m/s are presented in Table 4.11 and Figure 4.61, following the same methodology applied for the free stream velocity of 10 m/s. The objective of this free stream velocity is to compare the power generation results between

the setup with two rotating cylinders (section 4.3.1) and the wind turbine without the aerodynamical device (the “throat device”).

Table 4.11 – Power generation results for reference flow velocity of 12.6 m/s

| rpm | N° de LEDs [un.] | U [V] | i [mA] | P [mW] |
|------|------------------|-------|--------|--------|
| 3760 | 0 | – | – | – |
| 3760 | 1 | 1.52 | 64.6 | 98.19 |
| 3760 | 2 | 1.51 | 69.66 | 105.19 |
| 3760 | 3 | 1.55 | 69.01 | 106.97 |
| 3760 | 4 | 1.59 | 71.22 | 113.24 |
| 3760 | 5 | 1.55 | 72 | 111.60 |
| 3760 | 6 | 1.65 | 66.68 | 110.02 |
| 3745 | 7 | 1.68 | 67.45 | 113.32 |
| 3730 | 8 | 1.68 | 67 | 112.56 |
| 3725 | 9 | 1.66 | 67.58 | 112.18 |
| 3800 | 10 | 1.67 | 69.2 | 115.56 |

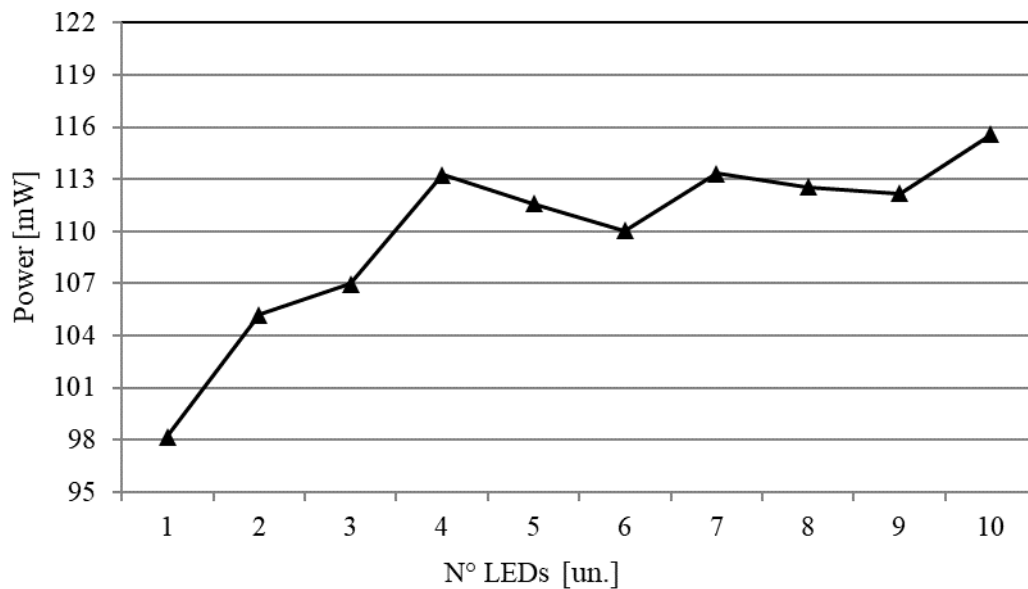


Figure 4.61 – Power generation for reference flow velocity of 12.6 m/s.

In Table 4.10 is possible to perceive that the rotational velocity is almost constant. Figure 4.60 shows that the maximum generated power is obtained with 10 LEDs in the system, being about 115.56 mW.

Comparing the results with the wind turbine at free-flow stream equal to 10 m/s, the quantity of power produced is similar, being about 4.2% lesser, even with the higher velocity in the free flow stream. The rotational velocity is lesser as well, showing that the aerodynamic device influences the obtained results, which was expected.

The results of the free to rotate cylinders show that, for the same velocity in the free flow stream, even with the aerodynamical device in the experiment with the cylinders, the wind turbine is able to produce almost 70% more power. The rotational velocity is also bigger, being about 77% faster. However, the noise produced by the free to rotate cylinders is lesser, and the manufacturing cost is lesser as well, implying that, depending on the application, the free to rotate cylinders are a reasonable option to generate power, even producing less power.

5 CONCLUSIONS

This work presented experimental results to analyze the bistable phenomenon and its ability to generate power for small applications, such as energy harvesting. Four main experiments were performed in the aerodynamic channel with hot-wire anemometer technique, considering arrangements with circular cylinders placed with a p/d ratio 1.26. The wavelet and Fourier analysis were performed in the obtained results with MATLAB software. An experiment in hydrodynamic flow channel was performed as well, considering the same dimensions for the channel and the cylinders used in the aerodynamic experiments.

The fixed cylinders were the starting point of this study, where were performed experiments regarding the presence of the bistability phenomenon. Both aerodynamic and hydrodynamic channels were used in this case, once the visualization in the hydrodynamic flow channel assists in the comprehension of the phenomenon and behavior observed in the results of the aerodynamic flow channel. Through these two combined techniques, the presence of the bistability was observed in both experiments for the side-by-side position and for 2.5° with the flow. In the last one, the bistability phenomenon was observed only in the hydrodynamic flow channel, suggesting that the inertia and the scales involved in this phenomenon may affect the results. Aerodynamic experiments presented two levels of velocity for side-by-side configuration, being clear its presence in the wavelet analysis performed, and the results for the power spectrum showed the presence of known Strouhal numbers in literature. Results for other angles presented two levels of velocity, one for each probe for angles lesser than 15° , and just one level of velocity for the others. The results for the same experiment in the hydrodynamic flow channel showed the presence of bistability for side-by-side configuration and for 2.5° , and for the other angles just the formation of the narrow and wide wakes. The width of the narrow wake found in the hydrodynamic flow channel for the side-by-side cylinders is in the order of the cylinder diameter ($O\sim 1.2d$), and for the wide wake is in the order of 1.7 times the cylinder diameter ($O\sim 1.7d$). Hydrodynamic and aerodynamic experiments were performed in the subcritical flow regime.

Results for free to rotate cylinders, performed in the aerodynamic flow channel with a high-speed camera showed that the system rotates after a certain period, and remains in this rotational regime during the rest of the experiment. However, several oscillations are visible in the assembly before the rotational regime. These oscillations are linked to the unbalance in

the drag forces, once the wakes formed behind the cylinders generate different values for the drag coefficients [Alam et al., 2003], forcing the cylinders to oscillate during this process. The results of wavelet and Fourier analysis showed oscillations in the velocity downstream the cylinders, what was perceived in the power spectrum, with energy concentration in the lower values of frequency during almost the whole experiment. The oscillation does not have a preferential direction of rotation and is a result of the chaotic characteristics [De Paula and Möller, 2018], but can be influenced by some factors such as transversal misalignment of the tubes in the rest condition before flow starts, geometrical imperfections and the blockage ratio oscillation. Power generation for this assembly happened for reference velocity equal to 12.6 m/s; other velocities imposed in the study of the wake behavior were not sufficient to rotate the generator used in this study. Two configurations were tested: in the first one an aerodynamic device was used to increase the acceleration and the blockage ratio and in the second one was placed one fixed cylinder, considering $p/d = 1.26$, to increase the acceleration close to the cylinders free to rotate. The results showed low values of power generation, with a maximum of 67.59 mW and 10.07 mW for the chosen generator, respectively, but both are able to generate power in small scales, like energy harvesting [Priya and Inman, 2009]. The experiments of the fixed cylinders were performed to understand what happens in the various angles which are obtained in the rotational cylinders, i.e., it was a preliminary study to better understand the oscillating phenomenon. The unbalance in drag forces observed by Varela et al., 2018 is the main mechanism to start the oscillation and then the rotation. After overcoming the unbalance due to the bistable phenomenon, the assembly oscillates because of the different wakes generated by the other angles, once after 15° a wide wake is formed in one cylinder and a narrow wake is formed in the other, as showed the static results, and each wake has a different drag coefficient. This dynamic behavior of the wakes leads to the oscillation and then the rotation of the system.

Wind turbine experiments were performed to compare with the rotational cylinders results, considering that the Savonius wind turbine is a good engineering device to produce energy, and has a simple design, which can be easily modeled and printed in a 3D printer [Akwa, 2014]. Velocity results regarding the velocity signals and the wavelet analysis showed lower levels of velocity behind the turbine for the same reference velocities employed in the case of the rotational cylinders. The power spectrum showed low energy concentrations, suggesting that the kinetic energy of the flow is converted to mechanical energy by the

turbine, increasing the efficiency to generate energy for the same conditions employed in the rotational cylinders. The turbine is able to produce energy for reference velocity equal 10 m/s, which was not observed for the free to rotate cylinders. For this velocity, an aerodynamic device was mounted into the channel, to accelerate and increase the blockage ratio. The results showed power generation of 119.78 mW for this configuration. Another reference velocity equal to 12.6 m/s was tested, the same for the free to rotate cylinders, but in this case, no aerodynamic device was employed, only the wind turbine by itself. The results showed power generation equal to 115.56 mW for the chosen generator, being very similar to the energy produced in the case with lower velocity and assistance of the aerodynamic device. Compared with the free to rotate cylinders, the wind turbine is able to produce 70% more energy, even without the aerodynamic device. However, the noise produced by the free to rotate cylinders is lesser, and the manufacturing cost is lesser as well, showing that both cases are applicable, depending on the purpose. The aerodynamic device is important in the results, once comparing the results with the wind turbine with lower velocity and aerodynamic device, the results presented are very similar, implying that the same energy can be produced using lower flow velocities.

Concluding the exploration of the bistability phenomenon, the results for free to oscillate cylinders showed some peculiarities. Four configurations were tested, as follows: natural, 1 obstacle, 2 obstacles, and perturbed. In the first one, the results showed few oscillations in the results of velocity, but low levels for them. For one and two obstacles, which are the configurations using aerodynamic devices during the whole experiment, larger angular amplitudes and higher levels of fluctuations in the velocity results were observed. More energy is associated with these experiments, shown in the CWT of the velocity results for these configurations. The perturbed configuration was compared to the natural configuration, where the system was perturbed with a device appropriated to do that. The increase in the velocity and angular positions were observed in the moment in which the perturbation was inserted into the aerodynamic channel. For the reference velocities equal to 7.5 m/s and 10 m/s, after the perturbation, the system achieved another level of amplitude, showing that the system has at least two levels of balance. Power generation for these four configurations was attempted with the electrical system used in the free to rotate cylinders and wind turbine, but once the generator works better with the rotational movement, the configurations were not able to generate energy for this electrical system, needing another

electrical system, perhaps with an piezoelectric system to convert the oscillatory behavior in electrical energy.

The main and specific objectives, proposed in the introduction of this work, were achieved along with the results presented in the text. The main contributions are the fact of the bistable phenomenon is able to produce power in small scales for the tested generator. The results for static and bistable phenomenon complements the results proposed by the others authors cited throughout the text. The power generation for the free to oscillate cylinders experiment was not possible using the electrical system employed in the other experiments. A specific electrical system needs to be mounted for this case.

5.1 Suggestions for future works

This work started with the exploration of the bistability phenomenon using the main tools used previously by other authors cited along with the text. This methodology is currently used and presents good results. Therefore, new studies for these topics can be performed using the methodology presented here.

The angular position for the cylinders presents several options for setting the angles and Reynolds numbers, but new studies in this sense must explore the influence of the misalignments for the bistable phenomenon, i.e., in which angle the bistability phenomenon is not perceived anymore. It can be hard to define, once the accuracy of the experiment must be very high. The reduction of the blockage ratio for the proposed study is also recommended.

The visualization in the hydrodynamic flow channel proved to be an accurate technique for the analysis of the wakes. The hoses used in this experiment were tested in order to analyze if they influence the results, and the recordings showed that they do not. However, it is suggested that they be installed out of the flow.

The experiments for power generation proved to be very useful for the cases with rotational configurations. However, the use of a Foucault break would allow the determination of the power curve of the system, stabilizing the parameters for building a prototype. For the case with the oscillatory cylinders, another electrical system needs to be studied to analyze the power to energy generation.

Visualizations with a high-speed camera together with the Tracker software analysis is a new technique employed in this work and worked well for the purposes studied. Another

software, commercial or an algorithm specifically developed for this purpose, may reduce the imprecision of the software. The low storage points are another problem that could be fixed.

BIBLIOGRAPHY

Afgan, I., Kahil, Y., Benhamadouche, S. and Sagaut, P. **Large eddy simulation of the flow around single and two side-by-side cylinders at subcritical Reynolds numbers.** *Physics of Fluids*, vol. 23, n. 7, 2011.

Akwa, J. V. **Estudo numérico e experimental do escoamento sobre um rotor eólico savonius em canal aerodinâmico com alta razão de bloqueio.** PhD thesis, Universidade Federal do Rio Grande do Sul, 2014.

Alam, M. M. and Meyer, J. P. **Two interacting cylinders in cross flow.** *Physical Review*, vol. 84, n. 5, p. 16, 2011.

Alam, M.M., Moriya, M. and Sakamoto, H. **Aerodynamic characteristics of two side-by-side circular cylinders and application of wavelet analysis on the switching phenomenon.** *Journal of Fluids and Structures*, vol. 18, n. 3–4, p. 325–346, 2003.

Alam, M. M. and Sakamoto, H. **Investigation of Strouhal frequencies of two staggered bluff bodies and detection of multistable flow by wavelets.** *Journal of Fluids and Structures*, vol. 20, n. 3, p. 425–449, 2005.

Anton, S. R. and Sodano, H. A. **A review of power harvesting using piezoelectric materials (2003-2006).** *Smart Materials and Structures*, vol. 16, n. 3, 2007.

Beeby, S. P., Tudor, M. J. and White, N. M. **Energy harvesting vibration sources for microsystems applications.** *Measurement Science and Technology*, vol. 17, n. 12, 2006.

Bendat, J. S. and Piersol, A. G. **Random Data – Analysis and Measurement Procedures.** 2. ed. . New York: John Wiley & Sons, 1990.

Blevins, R. D. **Flow-induced vibration.** Van Nostrand Reinhold, 1990.

Brown, G. L. and Roshko, A. **On density effects and large structure in turbulent mixing layers**. *Journal of Fluid Mechanics*, vol. 64, n. 4, p. 775–816, 1974.

Chauhan, B. V. S., Pratap, S.V., Imran, S. and Ajitanshu, V. **Numerical Modelling on Flow Pattern Determination for Circular Staggered Cylinders in Crossflow**. *Invertis Journal of Science & Technology*, vol. 12, p. 15, 2019.

Chen, S. S. **Flow-induced vibration of circular cylindrical structures**. National Technical Information Service, Springfield, 1985.

Chen, S. S. **A general theory for dynamic instability of tube arrays in crossflow**. *Journal of Fluids and Structures*, vol. 1, p. 35–53, 1987.

De Paula, A. V. **Estudo sobre o fenômeno da biestabilidade de escoamentos turbulentos em bancos de tubos de arranjo triangular**. Master's degree thesis, Universidade Federal do Rio Grande do Sul, 2008.

De Paula, A.V. **Determinação de parâmetros que caracterizam o fenômeno da biestabilidade em escoamentos turbulentos**. PhD thesis, Universidade Federal do Rio Grande do Sul, 2013.

De Paula, A.V and Möller, S. V. **On the chaotic nature of bistable flows**. *Experimental Thermal and Fluid Science*, vol. 94, p. 172–191, 2018.

De Paula, A. V., Endres, L. A. M. and Möller, S. V. **Bistable features of the turbulent flow in tube banks of triangular arrangement**. *Nuclear Engineering and Design*, vol. 249, p. 379–387, 2012.

De Paula, A. V. and Möller, S. V. **Finite mixture model applied in the analysis of a turbulent bistable flow on two parallel circular cylinders**. *Nuclear Engineering and Design*, vol. 264, p. 203–213, 2013.

De Paula, A. V., Endres, L. A. M.; Möller and Möller, S.V. **Experimental study of**

the bistability in the wake behind three cylinders in triangular arrangement. Journal of the Brazilian Society of Mechanical Sciences and Engineering, vol. 35, n. 2, p. 163–176, 2013.

Destefani, B. V. **Visualização da biestabilidade em dois cilindros circulares dispostos lado a lado em um canal hidráulico posicionados na horizontal e na vertical.** Graduation course thesis, Universidade Federal do Rio Grande do Sul, 2016.

Elhimer, M., Harran, G., Hoarau, Y., Cazin, S. and Marchal, M. **Coherent and turbulent processes in the bistable regime around a tandem of cylinders including reattached flow dynamics by means of high-speed PIV.** Journal of Fluids and Structures, vol. 60, p.62-79, 2016.

Endres, L. A. M., Möller, S. V. **On the fluctuating wall pressure field in tube banks.** Nuclear Engineering and Design, vol. 203, n. 1, p. 13–26, 2001.

Freire, A. P. S., Menut, P. P. M. and Su, J. **Turbulência.** . Rio de Janeiro - RJ, Brasil: ABCM, 2002.

Gu, Z., Sun, T., He, D.X. and Zhang, L.L. **Two circular cylinders in high-turbulence flow at supercritical Reynolds number.** Journal of Wind Engineering and Industrial Aerodynamics, vol. 49, p. 379–388, 1993.

Gu, Z. and Sun, T. **On interference between two circular cylinders in staggered arrangement at high subcritical Reynolds numbers.** Journal of Wind Engineering and Industrial Aerodynamics, vol. 80, n. 3, p. 287–309, 1999.

Habowski, P. B., de Paula, A. V. and Möller, S. V. **Analysis of the wake of two parallel circular cylinders at several angular positions to the flow.** Proceedings of COBEM 2019 – 25th International Congress of Mechanical Engineering, Uberlandia, MG – Brazil, 2019.

Hsu, L. C., Chen, C. L. and Ye, J. Z. **A study of flow patterns for staggered cylinders at low Reynolds number by spectral element method.** Journal of Mechanical Science and Technology, vol. 31, n. 6, p. 2765–2780, 2017.

Hu, J. C. and Zhou, Y. **Flow structure behind two staggered circular cylinders. Part 1. Downstream evolution and classification.** Journal of Fluid Mechanics, vol. 607, p. 51–80, 2008a.

Hu, J. C. and Zhou, Y. **Flow structure behind two staggered circular cylinders. Part 2. Heat and momentum transport.** Journal of Fluid Mechanics, vol. 607, p. 81–107, 2008b.

Hussain, A. K. M. F. **Coherent structures - Reality and myth.** Physics of Fluids, vol. 26, n. 10, p. 2816–2850, 1983.

Hussain, A. K. M. F. **Coherent structures and turbulence.** Journal of Fluid Mechanics, vol. 173, p. 303–356, 1986.

Indrusiak, M. L. S., Kozakevicius, A. J. and Möller, S. V. **Wavelet Analysis Considerations for Experimental Nonstationary Flow Phenomena.** Revista de Engenharia Térmica, vol. 15, n. 1, p. 67, 2016.

Indrusiak, M. L. S. and Möller, S. V. **Wavelet analysis of unsteady flows: Application on the determination of the Strouhal number of the transient wake behind a single cylinder.** Experimental Thermal and Fluid Science, vol. 35, n. 2, p. 319–327, 2011.

Indrusiak, Maria Luiza Sperb. **Caracterização de escoamentos turbulentos transientes usando a transformada de ondaletas.** 2004.

Moffat, R. J. **Describing the uncertainties in experimental results.** Experimental Thermal and Fluid Science, vol. 1, n. 1, p. 3-17, 1988.

Möller, S. V. and Silvestrini, J. H. **Turbulência: Fundamentos**. In: ABCM - Turbulência, 4. ed., Rio de Janeiro - RJ, Brasil: ABCM, 2004. p. 1–32.

Neumeister, R. F., Petry, A. P. and Möller, S. V. **Characteristics of the wake formation and force distribution of the bistable flow on two cylinders side-by-side**. Journal of the Brazilian Society of Mechanical Sciences and Engineering, vol. 40, n. 12, p. 1–19, 2018.

Olinto, C. R., Indrusiak, M. L. S., Enderes, L. A. M. and Möller, S. V. **Experimental study of the characteristics of the flow in the first rows of tube banks**. Nuclear Engineering and Design, vol. 239, n. 10, p. 2022–2034, 2009.

Païdoussis, M. P. **Flow-induced vibrations in nuclear reactors and heat exchangers: practical experiences and state of knowledge**. Proceedings of practical experiences with flow-induced vibrations, 1979.

Païdoussis, M. P. **A review of flow-induced vibrations in reactors and reactor components**. Nuclear Engineering and Design, vol. 74, p. 31–60, 1982.

Percival, D. B., Walden, A. T. **Wavelet Methods for Time Series Analysis**. Cambridge University Press, 2000.

Priya, S. and Inman, D. J. **Energy Harvesting Technologies**. Springer Science + Business Media, LLC, New York, 2009.

Priya, S. **Advances in energy harvesting using low profile piezoelectric transducers**. Journal of Electroceramics, vol. 19, n. 1, p. 165–182, 2007.

Scarselli, G., Nicassio, F., Pinto, F., Ciampa, F. Iervolino, O. and Meo, M. **A novel bistable energy harvesting concept**. Smart Materials and Structures, vol. 25, n. 5, p. 13, 2016.

Sumner, D. **Two circular cylinders in cross-flow: A review**. Journal of Fluids and Structures, vol. 26, n. 6, p. 849–899, 2010.

Sumner, D., Price, S. J. and Paidoussis, M. P. **Tandem Cylinders in Impulsively Started Flow**. Journal of Fluids and Structures, vol. 13, n. 7–8, p. 955–965, 1999.

Sumner, D., Price, S. J. and Paidoussis, M. P. **Flow-pattern identification for two staggered circular cylinders in cross-flow**. Journal of Fluid Mechanics, vol. 411, p. 263–303, 2000.

Sumner, D., Price, S. J. and Paidoussis, M. P. **Investigation of impulsively-started flow around side-by-side circular cylinders: Application of particle image velocimetry**. American Society of Mechanical Engineers, Aerospace Division (Publication) AD, vol. 53–1, p. 93–102, 1997.

Sun, T. F., Gu, Z. F., He, D. X. and Zhang, L. L. **Fluctuating pressure on two circular cylinders at high Reynolds numbers**. Journal of Wind Engineering and Industrial Aerodynamics, vol. 41, n. 1–3, p. 577–588, 1992.

Tubular Exchanger Manufacturers Association Inc. **TEMA Standards (Tubular Exchanger Manufacturers Association)**, 7th ed., New York. 1988.

Tennekes, H. and Lumley, J. L. **A First Course in Turbulence**. The MIT Press, 1972.

Varela, D. J. C. **Análise experimental do escoamento transversal turbulento sobre dois cilindros paralelos fixos, com liberdade oscilatória e rotacional**. Master's degree thesis, Universidade Federal do Rio Grande do Sul, 2017.

Varela, D., Neumeister, R. F., Dias, G., De Paula, A.V. and Möller, S.V. **Experimental analysis of turbulent transversal flow on two fixed parallel cylinders with oscillatory and rotational freedom**. Proceedings of COBEM 2017 – 24th International Congress of Mechanical Engineering, Curitiba, PR – Brazil, 2017.

Wong, C. W., Zhou, Y., Alam, M. M. and Zhou, T. M. **Dependence of flow classification on the Reynolds number for a two-cylinder wake**. Journal of Fluids and Structures, vol. 49, p. 485–497, 2014.

Woyciekoski, M. L., Endres, L. A. M., de Paula, A. V. and Möller, S. V. **Influence of the free end flow on the bistability phenomenon after two side by side finite height cylinders with aspect ratios of 3 and 4 and high blockage**. Ocean Engineering, vol. 195, p. 14, 2020.

Wu, G., Du, X. and Wang, Y. **LES of flow around two staggered circular cylinders at a high subcritical Reynolds number of 1.4×10^5** . Journal of Wind Engineering and Industrial Aerodynamics, vol. 196, p. 14, 2020.

Yang, Y., Shen, Q., Jin, J., Wang, Y., Qian, W. and Yuan, D. **Rotational piezoelectric wind energy harvesting using impact-induced resonance**. Applied Physics Letters, vol. 105, n. 5, p. 4, 2014.

Ye, Z-H., Sun, X. and Zhang, J.-Z. **Flow-induced vibrations of two staggered circular cylinders at low Reynolds number**. Journal of Vibration Testing and System Dynamics, vol. 3, n. 1, p. 39–54, 2019.

Zdravkovich, M. M. **The effects of interference between circular cylinders in cross flow†**. Journal of Fluids and Structures, vol. 1, n. 2, p. 239–261, 1987.

Zhou, Y. and Alam, M. M. **Wake of two interacting circular cylinders: A review**. International Journal of Heat and Fluid Flow, vol. 62, p. 510-537, 2016.

APPENDIX A Error Analysis of Tracker Software

To evaluate the error for the Tracker software, a sample of 6800 points was considered, where the cylinders were stopped. In this situation, the software oscillates very slightly in the acquisition of the points, as can be seen in Figure A.1. The values found for the error analysis are shown in Table A.1.

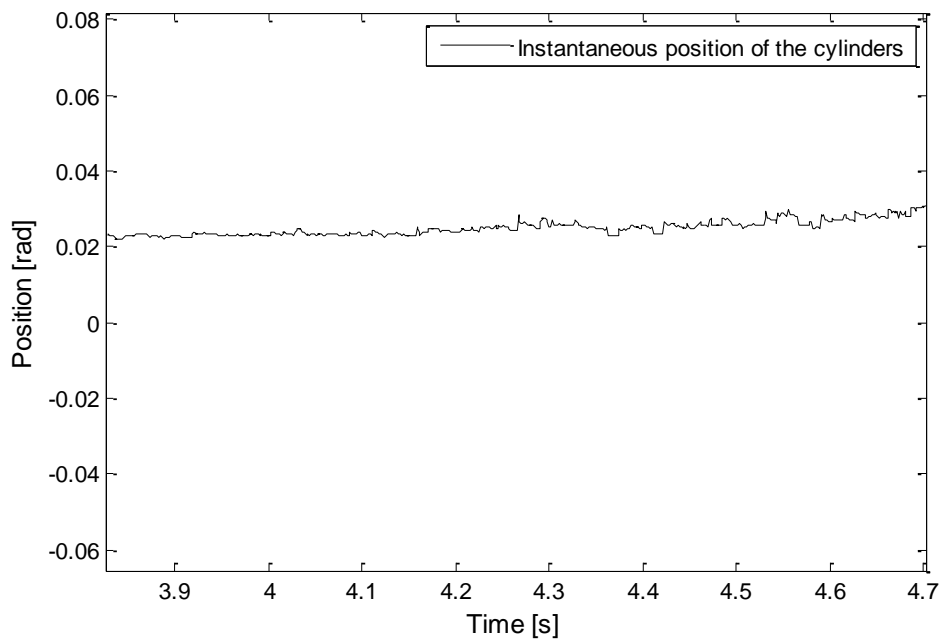


Figure A.1 – Details of the error associated with the acquisition of cylinder position data.

Table A.1 – Details of the error associated with the acquisition of cylinder position data.

| Statistical greatness | Value |
|-------------------------------|------------------------|
| Mean [rad.] | 0.0239 |
| Std. deviation [rad.] | 0.0038 |
| Variance [rad. ²] | 1.462×10^{-5} |

APPENDIX B Measurement Uncertainty

The measurement uncertainty is mandatory in experimental studies. The error is given by the difference between the actual and obtained value. According to Moffat, 1988, the measurement uncertainty is given by Equation B.1.

$$\delta R_i = \left\{ \sum_{i=1}^n \left(\frac{\partial R_i}{\partial x_i} \delta x_i \right)^2 \right\}^{1/2} \quad (\text{B.1})$$

In Equation B.1, R_i is the analyzed result and x_i is the uncertainty associated to the variable measured.

The uncertainty in the measurement of velocity series through the anemometry system is in the range of 2-7%, depending on the calibration curve used and the region of the curve on which the measurement is located.

The uncertainty in the values read for the frequencies of vortex shedding using the Fourier analysis depends on the bandwidth used (Be) and the average statistical error (ε) of each acquisition performed. Typical values for these are $3 \text{ Hz} < Be < 4 \text{ Hz}$ and $8\% < \varepsilon < 12\%$.

In the hydrodynamic channel, the uncertainty of the water level is approximated to $\pm 0.3 \text{ mm}$. The error of positioning the cylinders in both experiments is evaluated as $\pm 0.5 \text{ mm}$, where a pachymeter with a resolution of $\pm 0.05 \text{ mm}$ was used. Table B.1 presents a summarized scale resolution for the instruments used in this work.

Table B.1 – Main scale resolutions of used instruments.

| Instrument | Scale resolution |
|---------------------|---------------------------|
| Thermometer | $\pm 0.5^\circ \text{ C}$ |
| Barometer | $\pm 0.5 \text{ mm Hg}$ |
| Paquimeter | $\pm 0.05 \text{ mm}$ |
| Digital multimeter | $\pm 0.1 \%$ |
| Pressure transducer | 1% |
| Tachometer | 0.05% |

APPENDIX C Details About the Angular Base

The angular base, used to position the cylinders in the hydrodynamic flow channel, is presented in Figure C.1. This part was laser cut in at the *Innovation and digital manufacturing laboratory of the Engineering School (LIFEELAB)* of UFRGS.

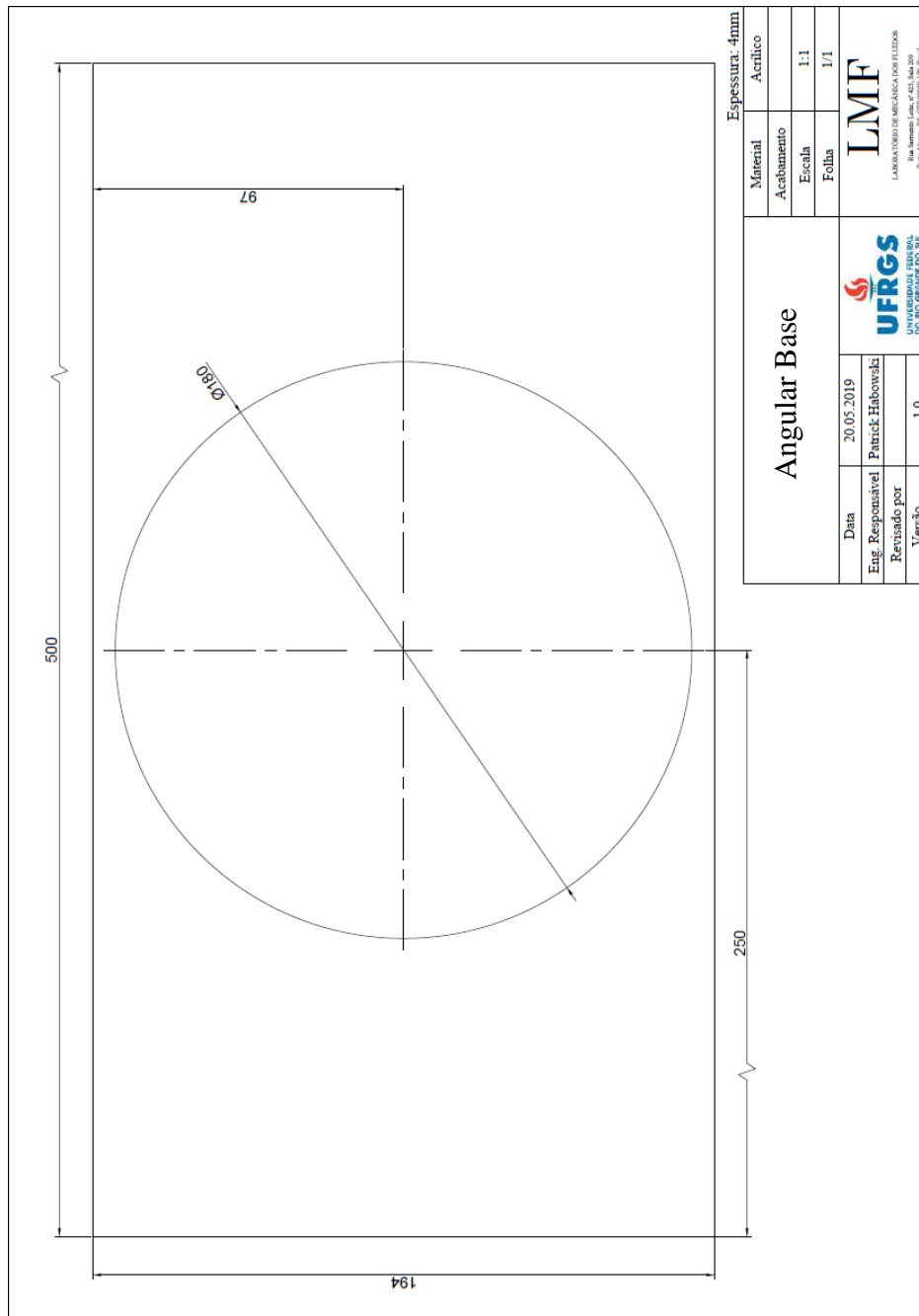


Figure C.1 – Angular base used to position the cylinders.

APPENDIX D Details About the Angular Positioner

The angular positioner, used to position the cylinders in the hydrodynamic flow channel, is presented in Figure D.1. This part was laser cut in at the *Innovation and digital manufacturing laboratory of the Engineering School (LIFEELAB) of UFRGS*.

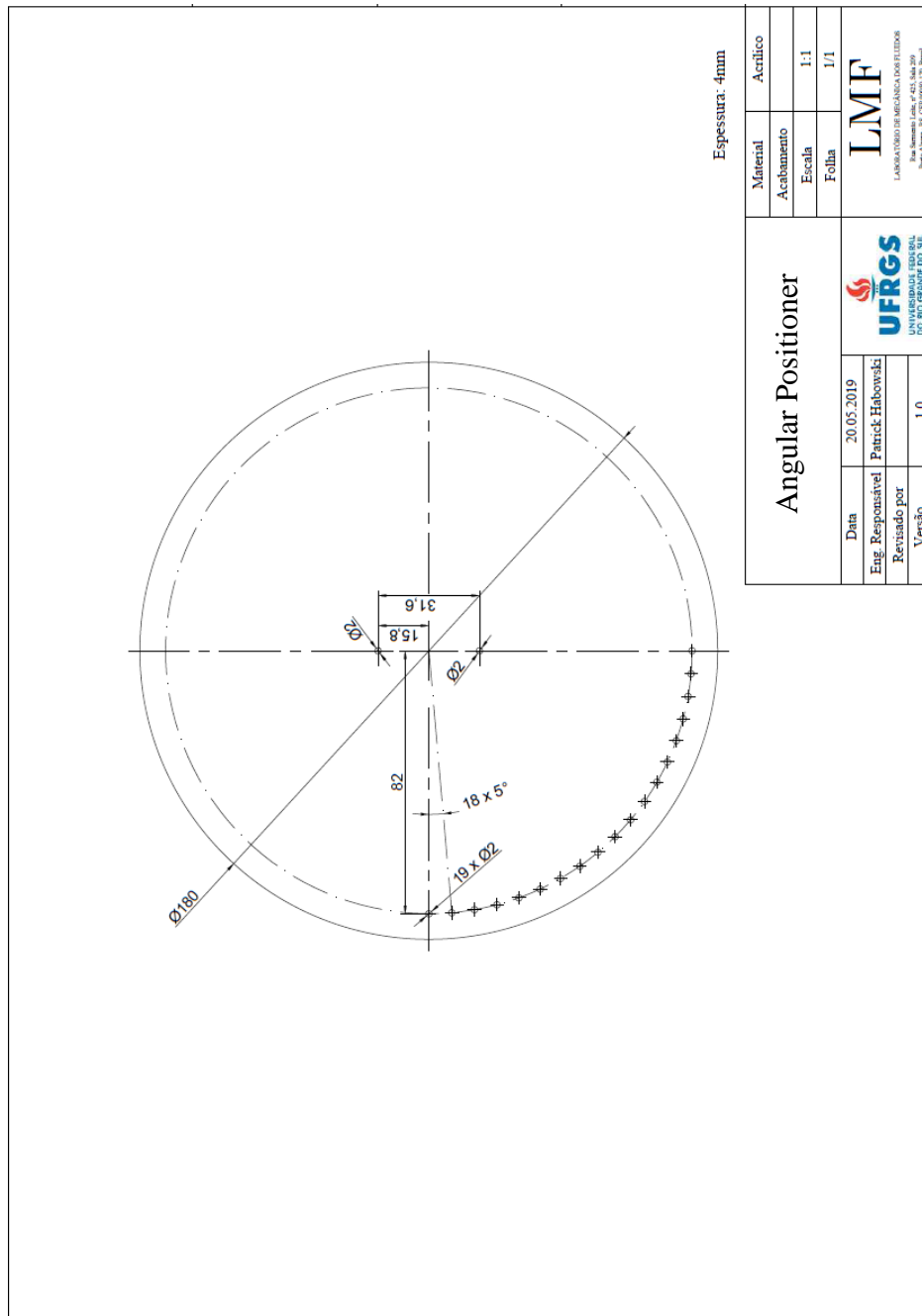


Figure D.1 – Angular positioner used to position the cylinders.

APPENDIX E Studies Involving Balance of Classical Dynamic Systems

This appendix presents the first studies involving the balance of classical dynamic systems that were found in the results of angular behavior of the free to oscillate cylinders for the reference velocity of 10 m/s (Figure 4.49c). Through the analysis of Figure 4.49 (c), were perceived that the system achieved two balance levels, where the second level of balance was generated perturbing the system with a metal rod and a cylinder with 32 mm of diameter (more detailed in sec. 4.4.4).

These levels of balance were plotted in Figure E.1, using a generalized van der Pol type oscillator. In Figure E.1 the red line represents the generalized van der Pol type oscillator, using reasonable coefficients, and the blue line is the results of the angular position results in Figure 4.49 (c). This is a preliminary result involving the idea of balance of dynamic systems, but the results of Figure 4.49 (c) (blue line in Figure E.1) presented reasonable similarity to the generalized van der Pol type oscillator (red line in Figure E.1). More studies in this sense will be performed in future works.

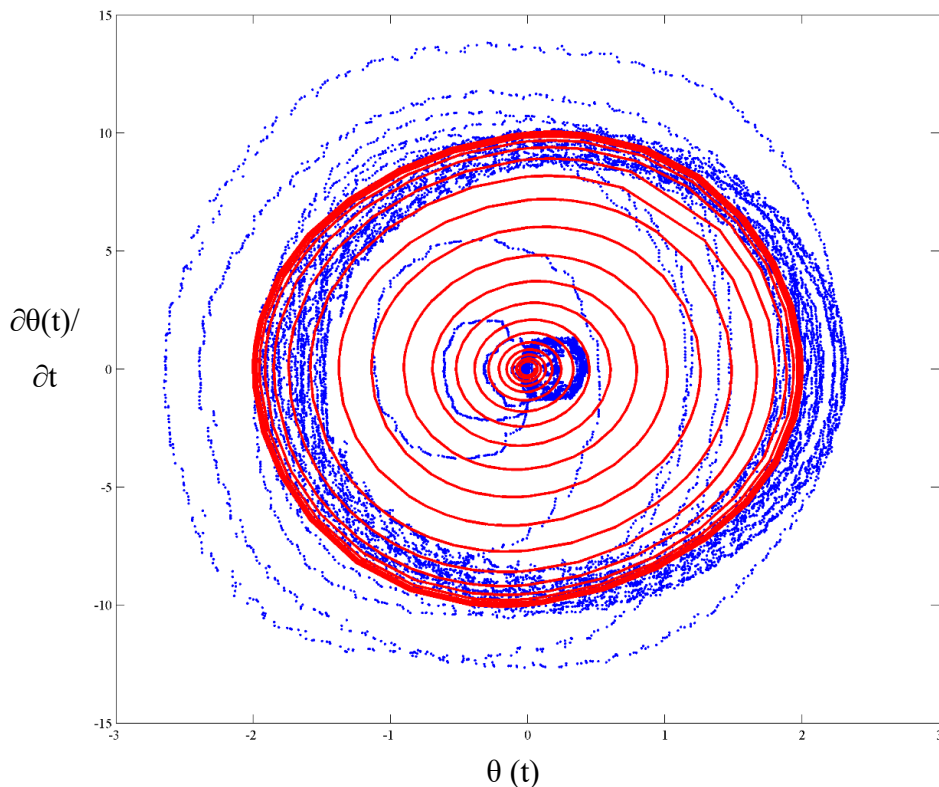


Figure E.1 – Results for the generalized van der Pol oscillator and angular behavior for free to oscillate cylinders, reference flow velocity of 10 m/s.